The Dissertation Committee for Hoshik Lee
certifies that this is the approved version of the following dissertation:

Quantum Chaos and Electron Transport Properties in a Quantum Waveguide

Committee:

Linda E. Reichl, Supervisor

Qian Niu

Tomio Y. Petrosky

Zhen Yao

Robert E. Wyatt

Quantum Chaos and Electron Transport Properties in a Quantum Waveguide

by

Hoshik Lee, B.S.; M.S.

DISSERTATION
Presented to the Faculty of the Graduate School of
The University of Texas at Austin
in Partial Fulfillment
of the Requirements
for the Degree of

DOCTOR OF PHILOSOPHY

THE UNIVERSITY OF TEXAS AT AUSTIN
May 2008

Dedicated to my wife Miyeon.

Acknowledgments

I was extremely fortunate to have had the opportunity to work in the Center for Complex Quantum Systems for the past six years. I would like express my thanks and gratitude to my thesis advisor, Prof. Reichl. She gives wonderful ideas and supports to me. She focus to connects diverse fields of physics through a deep understanding of the fundamentals, leading to a creative, challenging, and interactive work environment. I should say thanks to Prof. C. Jung in UNAM. He advised me for a part of this thesis. I would also thank to Dr. Kyungsun Na and Dr. Han Hsu (now in The University of Minnesota) for their invaluable discussions and feedback.

I appreciate my parents who always support me and encourage me to study. I could not finished my Ph.D. work without their supports. Finally, I want to express a special thanks to my wife, Miyeon, and daughter, Seoyoung.

Quantum Chaos and Electron Transport Properties in a Quantum Waveguide

Publication No. __________________

Hoshik Lee, Ph.D.
The University of Texas at Austin, 2008

Supervisor: Linda E. Reichl

We numerically investigate electron transport properties in an electron waveguide which can be constructed in 2DEG of the heterostructure of GaAs and AlGaAs. We apply R-matrix theory to solve a Schrödinger equation and construct a S-matrix, and we then calculate conductance of an electron waveguide.

We study single impurity scattering in a waveguide. A δ-function model as a single impurity is very attractive, but it has been known that δ-function potential does not give a convergent result in two or higher space dimensions. However, we find that it can be used as a single impurity in a waveguide with the truncation of the number of modes. We also compute conductance for a finite size impurity by using R-matrix theory. We propose an appropriate criteria for determining the cut-off mode for a δ-function impurity that reproduces the conductance of a waveguide when a finite impurity presents.

We find quantum scattering echoes in a ripple waveguide. A ripple waveguide (or cavity) is widely used for quantum chaos studies because it is easy to control a particle's dynamics. Moreover we can obtain an exact expression of Hamiltonian matrix with for the waveguide using a simple coordinate transformation. Having an exact Hamiltonian matrix reduces computation time significantly. It saves a lot of computational needs. We identify three families of resonance which correspond to three different classical phase space structures. Quasi bound states of one of those resonances reside on a heteroclinic tangle formed by unstable manifolds and stable manifolds in the phase space of a corresponding classical system. Resonances due to these states appear in the conductance in a nearly periodic manner as a function of energy. Period from energy frequency gives a good agreement with a prediction of the classical theory. We also demonstrate wavepacket dynamics in a ripple waveguide. We find quantum echoes in the transmitted probability of a wavepacket. The period of echoes also agrees with the classical predictions.

We also compute the electron transmission probability through a multi-ripple electron waveguide. We find an effect analogous to the Dicke effect in the multi-ripple electron waveguide. We show that one of the S-matrix poles, that of the super-radiant resonance state, withdraws further from the real axis as each ripple is added. The lifetime of the super-radiant state, for N quantum dots, decreases as $\frac{1}{N}$. This behavior of the lifetime of the super-radiant state is a signature of the Dicke effect.

Table of Contents

Acknowledgments **v**

Abstract **vi**

List of Tables **x**

List of Figures **xi**

Chapter 1. Introduction **1**

Chapter 2. R-matrix theory **10**

- 2.1 Formal Scattering Theory 10
- 2.2 R-matrix theory for an one dimensional system: I 12
- 2.3 R-matrix theory for an one dimensional system: II 19
- 2.4 R-matrix theory for a quasi one dimensional system 23

Chapter 3. Electron Conductance in a waveguide with a single impurity **32**

- 3.1 The Delta-function Impurity in 2-D Open Space 33
- 3.2 The Conductance for Waveguide with Finite Range Impurity . 35
- 3.3 The Conductance for Waveguide with Delta-function Impurity 38

Chapter 4. Ripple Cavity and Chaos **46**

- 4.1 Classical Dynamics of a ripple cavity 46
  - 4.1.1 Poincare Surface of Section 46
  - 4.1.2 Homoclinic and Heteroclinic Tangle 50
- 4.2 Hamiltonian Matrix of a ripple cavity 55
- 4.3 Husimi Function 60

Chapter 5. Scattering Echoes in a ripple waveguide **64**

5.1 Chaotic scattering in a waveguide with a ripple cavity 67

5.2 Conductance fluctuations and resonances 73

5.3 Quantum Echoes 81

5.4 The wavepacket dynamics 84

Chapter 6. Dicke Effect in a multi ripple waveguide **88**

6.1 The bi-ripple waveguide 91

6.2 Transmission Resonances and Husimi Plots 98

6.2.1 First Resonance Structure 98

6.2.2 Second Resonance Structure 101

6.2.3 Other Resonance Structures 106

6.3 Dicke Effect in a bi-ripple cavity 107

6.4 Tri- and Quad- Ripple Waveguide 111

Chapter 7. Conclusions **115**

Appendices **119**

Appendix A. Evaluation of a retarded free Green's function in Equation (2.27) **120**

Appendix B. Evaluation of Eq. (2.39) **124**

Appendix C. Hamiltonian matrix elements of a open ripple cavity (a zero-slope boundary condition for side walls) **126**

Bibliography **129**

Vita **138**

List of Tables

3.1 The constant μ for the disk shape potential, diameter $2a$ in a quantum waveguide, width L for different potential strength g and radius. 44

3.2 The constant μ for the square shape potential, width $2a$ in a quantum waveguide, width L for different potential strength g and width 45

5.1 The energy frequency $f_E = 1/\Delta E_0$ and T_c/τ_{SOS} for $n_p = 3, 4, 5, 6$. The horseshoe development parameter β is 3^{-3} 82

5.2 The energy frequency $f_E = 1/\Delta E_0$ and T_c/τ_{SOS} for different development of horseshoe 83

List of Figures

1.1 (a) a circular billiard which have regular trajectories, (b) a stadium type billiard which shows chaotic trajectories 2

1.2 Schematic view of the heterojunction of GaAs and AlGaAs and energy band diagram 4

1.3 (a) Electron waveguide in a 2DEG of GaAs/AlGaAs by shallow wet chemical etching technic (from Ref. [5]), (b) Quantized conductance through a quantum point contact (from Ref. [6], Copyright (1988) by the American Physical Society) 5

1.4 Magneto-resistance of two different shape quantum dots such as stadium (a) and regular circle (b) billiards (after from Ref. [4], Copyright (1992) by the American Physical Society) 7

1.5 (a) Classical dwell time probability for the cases of mixed (thick line) and fully chaotic (thin line) (b) Conductance for a mixed system (upper line) and a fully chaotic system (lower line) (from Ref. [10], Copyright (2000) by the American Physical Society) 8

2.1 Schematic view of one dimensional scattering with an asymptotic region. A particle enter from the left and reflects back due to the hard wall at $x = 0$. 13

2.2 Schematic view of one dimensional scattering with an asymptotic region. A particle enter from the left and reflects back due to the hard wall at $x = 0$. 19

2.3 A two-dimensional cavity attached to two semi-infinite leads (waveguides). 25

3.1 The geometry of the two dimensional electron waveguide with a single disk shaped impurity. L is the width of the waveguide. a is the radius of the impurity and y_0 is the transversal position of the impurity. $\hat{P}_\ell$ and $\hat{P}_r$ denote the asymptotic regions and $\hat{Q}$ denotes the reaction region. 36

3.2 Conductance of a waveguide with a finite range impurity for different numbers of modes, N. The impurity is disk shape, the potential strength $g = -7\,\mathrm{feVcm}^2$, and the radius $a = L/150$. When using $N = 120$, the conductance has converged to its final result. 37

3.3 Comparison of the conductance of a waveguide with finite range impurity and a waveguide with no impurity. The solid line is for the waveguide with a disk shaped impurity with $g = -7\,\mathrm{feVcm}^2$, $N = 120$, and $a = L/150$. The dotted line is for the waveguide with no impurity. There is a considerable conductance drop due to the electron localization around the impurity, and dips correspond to the quasi bound state. 40

3.4 Conductance for electron waveguide with a δ-function impurity. N denotes truncate number of modes. It shows conductance do not converge as N increases. 41

3.5 (a) Conductance for a waveguide with a single impurity. The solid line is for a disk shape impurity with $g = -7\,\mathrm{feVcm}^2$ and $a = L/400$. All other lines are for a δ-function impurity with a finite number of modes N_t and $g = -7\mathrm{feVcm}^2$. (b) The deviation in the first resonance dip. 43

4.1 A ripple cavity with a side wall height, L and the ripple amplitude, a. A particle bounce off the wall. 47

4.2 Poincare surface of sections in Birkhoff coordinate for a ripple cavity with L=0.7 and $W = 2\pi$ and the ripple amplitude (a) $a = 0$, (b) $a = 0.1$, (c) $a = 0.3$, (d) $a = 0.8$ 49

4.3 Sketch of stable($W^s(\mathbf{P})$) and unstable($W^u(\mathbf{P})$) manifolds for a saddle point P. Intersections of these manifolds form homoclinic points ($\mathbf{h}_n$). (from Ref. [30]) 51

4.4 Stable(solid) and unstable(dashed) manifolds of two fixed points near the side walls in a ripple cavity for a $L = 0.7$ and $a = 0.3$. 54

4.5 Poincare surface of section for a open ripple cavity with the same parameters as ones used for Fig. 4.4. Stable (blue) and unstable (red) manifolds are superimposed. Green line indicate gaps. 56

4.6 Husimi function of (a) 99th, (b)101st, (c) 102nd eigen states of a ripple cavity with the same parameters for Fig. 4.2 (c). . . . 62

4.7 Electron probabilities of eigen states corresponding to Fig. 4.6. 63

5.1 (a) The waveguide with ripple cavity for $a = 13.846\text{Å}$, $d = 47.269\text{Å}$ and $W = 300.0\text{Å}$. Leads are attached to the ripple cavity at $x = 0$ and $x = W$. α is the reflection angle at the bottom. (b) The classical Poincare surface of section using Birkhoff coordinates at the bottom boundary ($y = 0$). 68

5.2 The stable and unstable manifolds of the ripple cavity with parameters in given in Fig.5.1. The first tendril of unstable manifold is intersected by the third tendril of stable manifold in two points which implies that the horseshoe development is $\beta = 3^{-3}$. Inset shows two points intersections. 70

5.3 A set of initial condition closed to the unstable manifolds evolutes in time. A segment is repelled from the saddle following the unstable manifolds. Approaching the other saddle points, some of them escape from the cavity, but others are attracted by the saddle points following the stable manifolds. 72

5.4 Conductance G of the waveguide with ripple cavity for the energy range where there are three propagating modes in the leads. No evanescent modes in the leads are included. The scattered triangles represent the eigenenergies of the corresponding closed billiard. The symbols "+" locate the resonances associated with the large KAM island. The symbols "o" locate the resonances associated with the period-6 island chain. 76

5.5 Fano shape resonances at (a) $E = 5.612$eV (a scattering state on the large KAM island). (b) $E = 6.204$eV (a scattering state on the island chain surrounding the large KAM island), (c) $E = 6.288$eV (a scattering state on the chaotic layer) Dashed lines show fitted results. The fitted parameters, E_R, Γ, and q are given. 77

5.6 Husimi plots of resonant scattering states for the resonances in Fig. 5.5. (a) The state at $E = 5.612$eV lies on the large KAM island. (b) The state at $E = 6.204$eV lies on the island chain surrounding the large KAM island. (c) The state at $E = 6.288$eV lies on the chaotic scattering layer and has high probability regions closed to the outer fixed points. Husimi plots (a) and (b) are superimposed on the classical Poincare surface of section, and (c) on the stable and unstable manifolds. 79

5.7 The FFT of Fig. 5.4. To perform the FFT, we remove the monotonic background. The plot yields a fundamental frequency $f_E = 1/\Delta E_0 = 3.81(eV)^{-1}$. 80

5.8 Husimi Plots for resonant scattering states on the chaotic layer for (a) $E = 6.557$eV, (b) 6.824eV, and $E = 7.086$eV. These states all cover the chaotic scattering layer. 81

5.9 The probability amplitude function $b_3(E)$ (dashed line) of the eigenfunction expansion for an initial wavepacket with $g = 66.487$Å, $x_0 = -1000$Å, and $k_0 = 0.1889$Å^{-1} superposed on the conductance fluctuations for the corresponding energy regime. 85

5.10 The transmitted wavepacket $|\Psi(x', y', t)|^2$ in the asymptotic region of the right lead ($x' = 1000\mathring{A}, y' = L/2$) as a function of time. The inset is a linear-log plot of the probability which appears to decay exponentially. 87

6.1 (a) The schematic view of the bi-ripple waveguide, where $a = 13.846\mathring{A}$ and $d = 47.269$. θ is the reflection angle at the bottom wall. (b) The classical Poincare surface of section using Birkhoff coordinate at the bottom boundary. The parameter a and d are chosen to have mixed phase space. 92

6.2 Electron transmission through the double ripple cavity for the energy range where only a propagating modes is allowed in the leads. No evanescent modes are included. The triangles represent the eigen energies (E_j in Eq. 6.2) for the corresponding bi-ripple cavity(Neumann boundary condition at the interfaces, but Dirichlet boundary condition at upper and bottom walls). 99

6.3 Lowest energy conductance resonance in the first channel. (a) Solid line (dashed line) represents the electron transmission for the bi-ripple (mono-ripple) waveguide. (b) Contour plot of log T in a complex energy plane. (c) Spatial distribution of ψ_{17}. Red (blue) is positive (negative). (d) Spatial distribution of ψ_{18}. 100

6.4 (a) and (a') show the electron transmission and contour plot of T in the complex energy plane, respectively when we take into account only ψ_{16} and ψ_{17}. (b) and (b') use only ψ_{18} and ψ_{19} (c) and (c') use ψ_{16}, ψ_{17}, ψ_{18} and ψ_{19}. (d) and (d') use ψ_{15}, ψ_{16}, ψ_{17}, ψ_{18} and ψ_{19}. 102

6.5 (a) Electron transmission at the second resonance energy for the bi-ripple waveguide shows the resonance splitting. The dashed line is the electron transmission for the mono-ripple waveguide. (b) Contour plot of T in a complex energy plane. It shows two poles and a transmission zero. (c) a magnified version of (b) near the transmission zero. It confirms that a pole is located near the real axis. 104

6.6 (a) and (b) the Coefficient γ_j at the incident energy $E = 1.583053E_1$ which corresponds to the perfect transmission and $E = 1.583053E_1$ which corresponds the transmission zero, respectively. (c) and (d) represent the real part of the scattering wavefunction at $E = 1.583053E_1$ and $E = 1.583053E_1$, respectively. (e) $\sim$ (f) show the R-matrix basis state wavefunction for states ψ_{21}, ψ_{22}, and ψ_{23}. 105

6.7 The electron transmission in the neighborhood of the energies: (a) $E = 2.3779E_1$, (b) $E = 2.8851E_1$, and (c) $E = 2.9062E_1$. The Husimi plots of scattering eigenstates at the energies (d) $E = 2.3779E_1$, (e) $E = 2.8851E_1$, and (f) $E = 2.9235E_1$. . . . 108

6.8 (a) The electron transmission in the neighborhood of the 2nd resonance structure for the N-ripple waveguide for N=2 (black solid), N=3(blue dash), and N=4(red dot-dash) (b) S-matrix in a complex energy plane for tri-ripple waveguide. (c) S-matrix in a complex energy plane for quad-ripple waveguide. 113

6.9 The width $|\Gamma|$ of the superradiant quasibound state at the second resonance structure energy for N-ripple waveguide with $N = 1 \sim 5$. Dashed line show the linearly fitted line for help to see the linearity. 114

A.1 Path of integral in complex k-plane 121

Chapter 1

Introduction

Quantum chaos study has been intensively paid attention in the last few decades. Chaos means the unpredictability of the trajectory of a classical particle in a macroscopic system. However, one cannot expect to find a unpredictability of a trajectory in a quantum mechanical system because we have no phase space for individual trajectory due to the uncertainty principle. However, quantum chaos was defined as the manifestation of classical chaos in a quantum system [1, 2]. Classical trajectory of a billiard have been studied for more than a century. As shown in Fig. 1.1, two different shape billiard show different classical motion of particles. Fig. 1.1 (b) shows a stadium billiard in which the trajectory is chaotic while Fig. 1.1 (a) shows a circular billiard and regular trajectories. These two different types of billiard also show different quantum characteristics such as the spectral statistics of level spacing of eigen energies [1]. A classically regular system such as a circular billiard shows a Poisson-like spectral spacing distribution while a chaotic billiard has a Wigner-like distribution. Moreover, in particular, an quantum eigen wavefunction of a stadium billiard resembles with a unstable periodic orbits of a corresponding classical particle [3]. These structure are called *scars*.

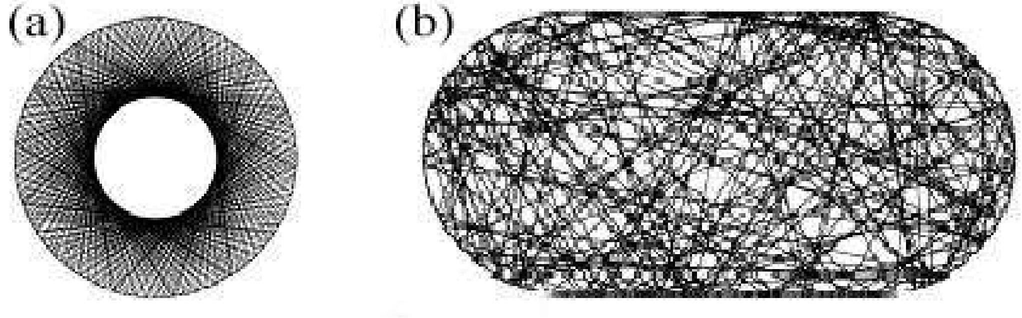

Figure 1.1: (a) a circular billiard which have regular trajectories, (b) a stadium type billiard which shows chaotic trajectories

Due to the advance of nano technology, nano structure can be fabricated in semiconductor. Electron transport study in a nano structure have been focused in a few decades. It is possible that one fabricate the semiconductor in which the coherent length of an electron is longer than the typical dimension of the structure at very low temperature. Therefore, quantum mechanical behaviors of electrons can emerge in such a small electronic device. Wave nature of electron can be seen in such nano structure as, for example, quantum dots, nano wires, quantum waveguides, a quantum point contact *etc.* In particular, two dimensional electron gas in the heterostructure of GaAs and AlGaAs has a huge electron mobility ($\mu \sim 10^6 cm^2 Vs$) and long mean free path ($\ell \sim 10\mu m$) at very low temperature. Electron scattering in a nano structure of 2DEG is therefore ballistic because electron-phonon interaction and electron-electron interaction are negligible at low temperature. It enable us to study quantum chaos in a microscopic device. For example, stadium type quantum dot (chaotic) and circular quantum dot (regular) show quite different quantum characteristics. Electron conduction through a chaotic quantum dot show high aperiodic oscillation which is dominated by stable trajectories of the classical counter part [4].

In this chapter, we briefly review two dimensional electron gas (2DEG) and a few nano structures which can be fabricated on 2DEG. We also review some experiments and numerical results which show quantum phenomena in classically chaotic systems and mixed phase space systems.

A thin electron gas layer is formed in a heterostructure of GaAs and AlGaAs. A sharp potential barrier is formed at the interface between GaAs and AlGaAs due to the different band gap. AlGaAs has wider band gap than GaAs even though they have similar lattice structure and lattice constant. Electrons are transferred from the layer of dopped-AlGaAs to GaAs because Fermi energy in dopped-AlGaAs is higher than in GaAs. The charge transfer gives rise to an electrostatic filed that cause the energy bands to bend at the interface as shown in Fig. 1.2. Electrons from n-dopped AlGaAs are accumulated in a triangular potential well in GaAs. Due to the potential well, the electron motion is confined along the lateral direction. This system is refereed as a two-dimensional electron gas (2DEG). Typical carrier concentration is about $2 \times 10^{11}/cm^2$. Since AlGaAs and GaAs form a nearly perfect interface and electrons are well separated from their ions in AlGaAs, electron scattering from ions is almost negligible. As a result, an election in a 2DEG has a very high mobility.

Two dimensional nano structure can be obtained by metal gates fabri-

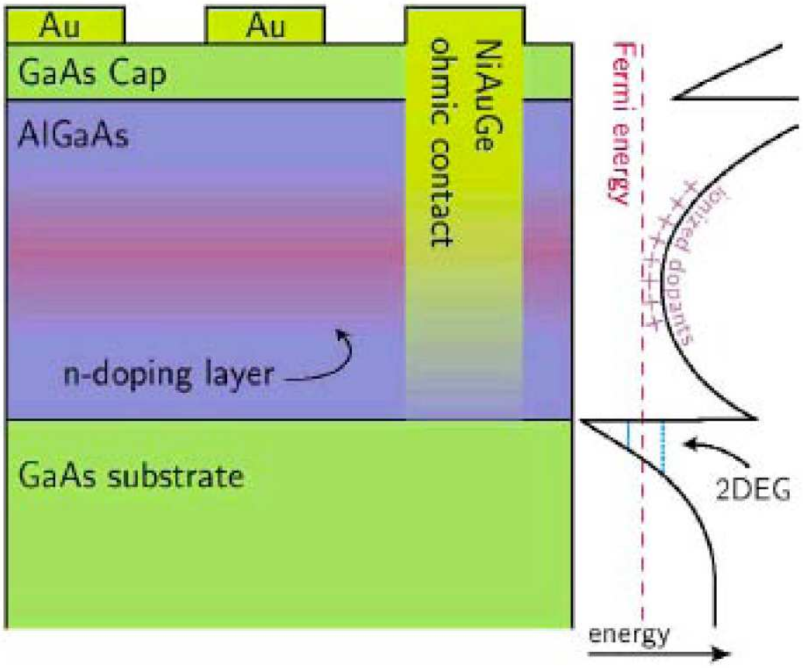

Figure 1.2: Schematic view of the heterojunction of GaAs and AlGaAs and energy band diagram

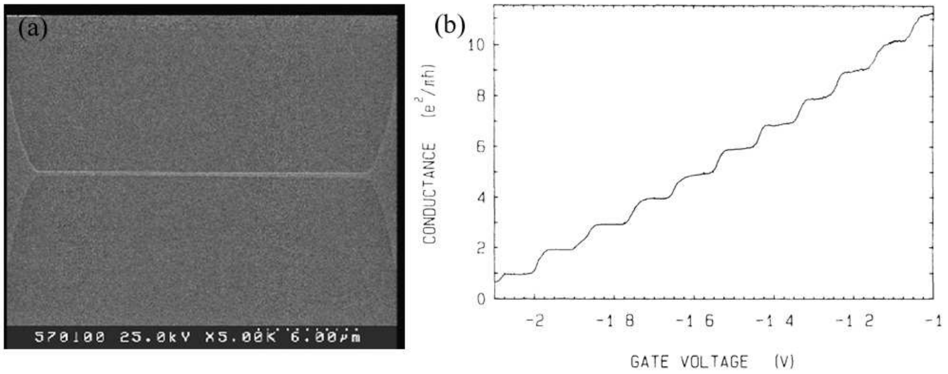

Figure 1.3: (a) Electron waveguide in a 2DEG of GaAs/AlGaAs by shallow wet chemical etching technic (from Ref. [5]), (b) Quantized conductance through a quantum point contact (from Ref. [6], Copyright (1988) by the American Physical Society)

cated on the surface of the heterostructure. Applying negative gate voltage on the metal gate gives rise to the formation of electrostatic potential by depleting of electrons underneath gates. Electrons in 2DEG are confined by the potential whose size and shape can be easily controlled by gate voltages. Fig.1.3 (a) shows an electron waveguide formed on 2DEG of GaAs/AlGaAs [5]. Conductance of an electron waveguide is quantized as shown in Fig. 1.4 (b) because electron wavefunction is discretized along the transversal direction due to the confinement potential. Each transversal mode carries a conductance quanta $2e^2/h$.

It has proven that R-matrix theory is so useful for study of an electron scattering in a waveguide. Conductance does not obey the Ohm's law any more in a nano scale device. Instead of Ohm's law, conductance is proportional to the transmission probability from the Landauer's formula. Using

R-matrix theory, we can calculate the transmission probability and scattering wavefunctions. In Chapter 2, we briefly review the formal theory of quantum scattering. We also reformulate R-matrix theory for low dimensional systems.

Single impurity scattering in a waveguide have been studied in a few decades. Interference between electron backscattering from the waveguide and a single impurity forms a quasi bound state in a waveguide. It significantly reduce conductance of the waveguide. Delta-function potential is preferred for a model of a single impurity because it simplify the computation. However, it has been known that a δ-function potential does not gives us a convergent result in two or higher space dimensions. Therefore, many other approaches have been studied for example, an impurity D-function model [7] *etc.* However, if the δ-function potential is regularized in a open system, it can give us a physically meaningful result [8, 9]. In Chapter 3, we investigate an effect of a single impurity on conductance of a waveguide and propose a criteria of cutoff-mode for a δ-function model to reproduce a finite size impurity model. We use R-matrix theory to calculate a S-matrix for a waveguide which contain a finite-size impurity.

In 1992, Marcus's ground-breaking experiment [4] has opened quantum chaos study in a micron-scale semiconductor structure such as a regular circle billiard and a stadium billiard shown in Fig. 1.4. One can nowadays fabricate such billiards as a sub-micron quantum dots. Fig. 1.4 shows aperiodic conductance fluctuations as a function of an applied magnetic field. They found that power spectra of theses fluctuation indicate different quantum characteristics

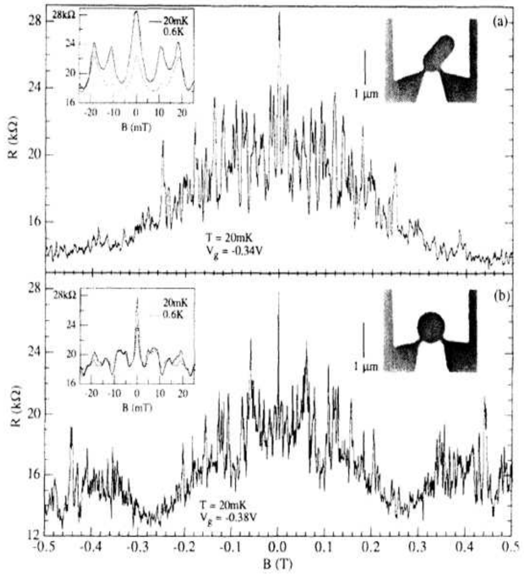

Figure 1.4: Magneto-resistance of two different shape quantum dots such as stadium (a) and regular circle (b) billiards (after from Ref. [4], Copyright (1992) by the American Physical Society)

for a chaotic and regular dots. They also observed that power spectrum at low frequency is dominated by a few periodic orbits of a corresponding classical particle.

In addition to fully chaotic system (*e.g.* stadium billiard), a mixed phase space system has been studied recently. A system whose phase space have regular areas and chaotic sea is called *mixed phase system.* Fully chaotic systems and mixed phase systems shows different behavior in both classical and quantum mechanical systems. For example, Dwell time probability for a classical particle of a open ripple cavity with parameters for a mixed phase system shows a power law decay rather than exponential decay shown in a fully

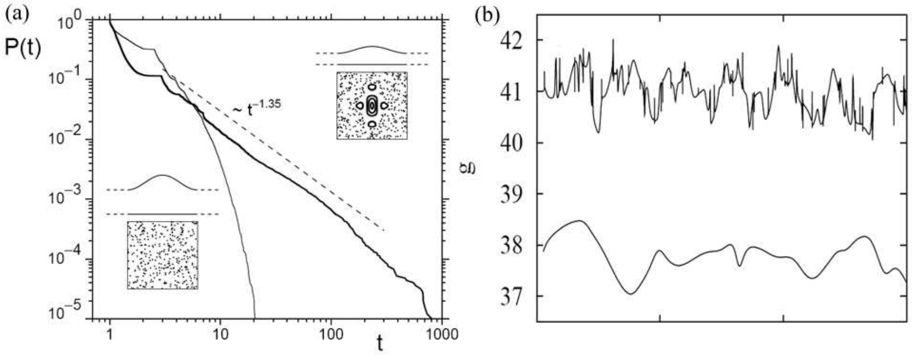

Figure 1.5: (a) Classical dwell time probability for the cases of mixed (thick line) and fully chaotic (thin line) (b) Conductance for a mixed system (upper line) and a fully chaotic system (lower line) (from Ref. [10], Copyright (2000) by the American Physical Society)

chaotic system as shown in Fig. 1.5 (a). Power law decay for a mixed system indicates fractal behavior of classical trajectories which do not appear in a fully chaotic system. Conductance for the ripple cavity also shows different quantum behavior for a mixed system and a fully chaotic system. The lower line in Fig. 1.5 (b) shows the smooth variation of conductance for a fully chaotic ripple cavity. However, many sharp peaks appear on top of smooth variation for the case of mixed phase space system. Bäcker *et al.* identified these sharp peaks as a eigen states which correspond to a regular region and hierarchical region around KAM tori of the phase space for the classical counterpart.

In this work, we investigate quantum behavior of an electron in a ripple waveguide. Especially, we study the quantum mechanical effects in the case that a ripple waveguide has a *mixed phase space*. In Chapter 4, we overview the classical dynamics of a ripple cavity. We also compute Hamiltonian matrix elements and Husimi distribution for a ripple cavity. In Chapter 5, we find quantum scattering echoes in a ripple waveguide in both energy domain and time domain. We identify resonances in conductance by plotting Husimi functions at resonance energies. We find that a family of resonances is corresponding to the *tangle* structure in the classical phase space and dominates quantum scattering echoes. We calculate the period of the echoes and compare it with the prediction from classical theory. We also investigate wavepacket dynamics in a ripple waveguide.

In 1950s, Dicke predicted that decay channels of electrons in two-atom system split into two channel in spontaneous emission. One channel is very fast and corresponds to a broad resonance. It is called *super-radiant* resonance. The other channel is so slow that it has very sharp resonance, namely, *sub-radiant* resonance. These two different decays from symmetry related collective states of two atoms which interact via common photon fields. Analogous effects was found in a mesoscopic systems 40 years after Dicke's prediction. In Chapter 6, we study the resonance splitting in a multi-ripple waveguide. We find the resonance splitting is a analogous effect of Dicke effect found in quantum optics. These splitting is due to the interaction of quasi bound states of each ripple cavity. We also found that the lifetime of super radiant resonance decrease as the number of ripple, N.

The conclusions are given in Chapter 7.

Chapter 2

R-matrix theory

R-matrix theory was developed by Wigner and Eisenbud for analyzing the nuclear scattering data in 1950s [11, 12]. Recently, it has been proved that it is so useful and efficient to compute S-matrix for electron scattering in a electron waveguide[13, 14, 15, 16]. In this chapter, we briefly review formal quantum scattering theory. We also review a R-matrix formalism for one dimensional electron scattering and later expand this formalism to a quasi one dimensional system.

2.1 Formal Scattering Theory

Schrödinger equation of an electron scattering in a potential V is given by

$$(E-H)|\Psi\rangle = 0, \tag{2.1}$$

where $H = H_0 + V$. General solution of Eq. (2.1) for a scattering system is a Lippman-Schwinger equation such as,

$$\begin{aligned} |\Psi^{(+)}\rangle &= |\phi_0\rangle + \frac{1}{E-H+i\epsilon}V|\phi_0\rangle \\ &= |\phi_0\rangle + G^{(+)}V|\phi_0\rangle, \end{aligned} \tag{2.2}$$

where G is a total Green's function, and $|\phi_0\rangle$ is a homogeneous solution. In this case, $\langle x|\phi_0\rangle$ is a incident plane wave.

A multi channel scattering matrix, $\mathbf{S_{ba}}$ can be defined [17, 18] such as,

$$\begin{aligned}
\mathbf{S_{ba}} &\equiv \langle\Psi_b^{(-)}|\Psi_a^{(+)}\rangle \qquad (2.3)\\
&= \langle\Psi_b^{(+)}|\Psi_a^{(+)}\rangle + \langle\Psi_b^{(-)} - \Psi_b^{(+)}|\Psi_a^{(+)}\rangle\\
&= \delta_{ba} + \langle\Psi_b^{(-)} - \Psi_b^{(+)}|\Psi_a^{(+)}\rangle\\
&= \delta_{ba} + \lim_{\epsilon\to 0}\left\langle \phi_0 \,\middle|\, V\left(\frac{1}{E_b - H + i\epsilon} - \frac{1}{E_a - H - i\epsilon}\right)\middle|\, \Psi_a^{(+)}\right\rangle\\
&= \delta_{ba} + \lim_{\epsilon\to 0}\langle\phi_b|\, V|\Psi_a^{(+)}\rangle\left(\frac{1}{E_b - E_a + i\epsilon} - \frac{1}{E_b - E_a - i\epsilon}\right)\\
&= \delta_{ba} - 2\pi i\delta(E_b - E_a)\langle\phi_b|\, V|\Psi_a^{(+)}\rangle.
\end{aligned}$$

In the last step, the following identity is used

$$\lim_{\epsilon\to 0}\frac{1}{E \pm i\epsilon} = \mathbf{P}\frac{1}{E} \mp i\pi\delta(E). \qquad (2.4)$$

We can define a *T-matrix*.

$$\begin{aligned}
T^{(+)} &\equiv V + V\lim_{\epsilon\to 0}\frac{1}{E - H + i\epsilon}V = V + VG^{(+)}V \qquad (2.5)\\
&= V(1 + G^{(+)}V) = V + VG_0^{(+)}V + VG_0^{(+)}VG_0^{(+)}V + \cdots ,
\end{aligned}$$

where $G_0^{(+)}$ is a free Green's function defined as

$$\hat{G_0}^{(+)} = \lim_{\epsilon\to 0}\frac{1}{E - H_0 + i\epsilon}. \qquad (2.6)$$

We use the dyson series for the total green function such as

$$G^{(+)} = G_0^{(+)} + G_0^{(+)}VG_0^{(+)} + G_0^{(+)}VG_0^{(+)}VG_0^{(+)} + \cdots . \qquad (2.7)$$

If we plug it into Eq.(2.2), the asymptotic region wavefunction is given by,

$$\begin{aligned} |\Psi^{(+)}\rangle &= |\phi_0\rangle + (G_0^{(+)} + G_0^{(+)} V G_0^{(+)} + \cdots)V|\phi_0\rangle \\ &= |\phi_0\rangle + G_0^{(+)}(V + V G_0^{(+)} V + \cdots)|\phi_0\rangle \\ &= |\phi_0\rangle + G_0^{(+)} T^{(+)}|\phi_0\rangle. \end{aligned} \tag{2.8}$$

We hence have a S-matrix in terms of T-matrix such as

$$\mathbf{S_{ba}} = \delta_{ba} - 2\pi i \delta(E_b - E_a)\langle\phi_b|\, T|\phi_a\rangle. \tag{2.9}$$

2.2 R-matrix theory for an one dimensional system: I

We consider 1-dimensional electron scattering in this section. As shown in Fig. 2.1, we assume that an electron incidents from $x = \infty$ and there is a arbitrary potential $V(x)$ in a range of $0 \le x \le a$. There is also a hard wall at $x = 0$ so that an electron reflects back to the asymptotic region In order to use the R-matrix theory, we divide the configuration space into largely two sub-spaces such as a reaction region and an asymptotic region as seen in Fig. 2.1. The essence of R-matrix theory is that we can expand a scattering wavefunction in the reaction region with a set of basis functions which satisfy a certain boundary condition at the interface. We introduce the projection operators to divide such areas,

$$\hat{Q} = \int_0^a dx|x\rangle\langle x| \tag{2.10}$$

$$\hat{P} = \int_a^\infty dx|x\rangle\langle x|\,. \tag{2.11}$$

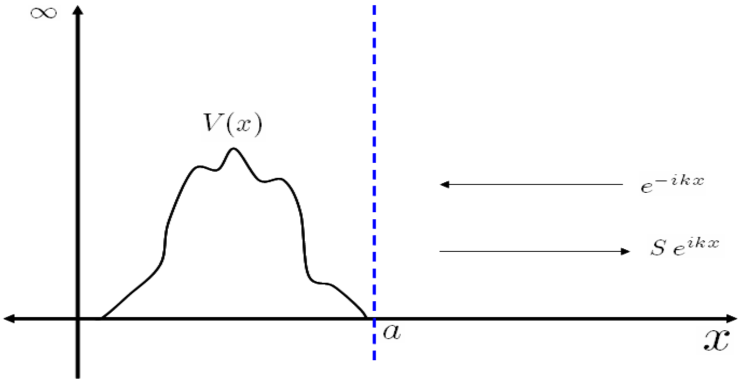

Figure 2.1: Schematic view of one dimensional scattering with an asymptotic region. A particle enter from the left and reflects back due to the hard wall at $x = 0$.

These projection operators satisfy the conditions $\hat{P} + \hat{Q} = \hat{1}$, $\hat{P}^2 = \hat{P}$, $\hat{Q}^2 = \hat{Q}$, and $\hat{P}\hat{Q} = \hat{Q}\hat{P} = 0$. The potential exists only in *Q-space* (reaction region). Using these properties, we have two Schrödinger equations.

$$\begin{aligned}(E - H_{PP})\hat{P}|\Psi\rangle &= H_{PQ}\hat{Q}|\Psi\rangle &(2.12)\\ (E - H_{QQ})\hat{Q}|\Psi\rangle &= H_{QP}\hat{P}|\Psi\rangle, &(2.13)\end{aligned}$$

where H_{PQ} and H_{QP} depends on boundary conditions in each area. We will discuss it later in this section. The total Hamiltonian of the system can be written by

$$H = H_{PP} + H_{QQ} + H_{PQ} + H_{QP}. \tag{2.14}$$

We can easily get a general solution of Eq. (2.12) including a homogeneous solution $|\phi_0(E)\rangle$.

$$\hat{P}|\Psi\rangle = |\phi_0(E)\rangle + \frac{1}{E - H_{PP}} H_{PQ}\hat{Q}|\Psi\rangle \tag{2.15}$$

After plug it into Eq. (2.13), we have a wavefunction in Q-space in terms of a homogeneous solution.

$$\hat{Q}|\Psi\rangle = \frac{1}{E - H_{QQ} - H_{QP}\frac{1}{E-H_{PP}}H_{PQ}} H_{QP}|\phi_0(E)\rangle \tag{2.16}$$

Finally, we have a scattering wavefunction in a asymptotic region (P-space).

$$\begin{aligned} \hat{P}|\Psi\rangle &= |\phi_0(E)\rangle \\ &+ \frac{1}{E - H_{PP}} \underbrace{H_{PQ}\frac{1}{E - H_{QQ} - H_{QP}\frac{1}{E-H_{PP}}H_{PQ}} H_{QP}}_{T} |\phi_0(E)\rangle \\ &= |\phi_0(E)\rangle + \hat{G^0_P} T|\phi_0(E)\rangle \end{aligned} \tag{2.17}$$

Hence, by definition, S-matrix is written by

$$\mathbf{S} = 1 - 2\pi i \left\langle \phi_0(E) \middle| H_{PQ}\frac{1}{E - H_{QQ} - H_{QP}\frac{1}{E-H_{PP}}H_{PQ}} H_{QP} \middle| \phi_0(E) \right\rangle . \tag{2.18}$$

To ensure the continuity of wavefunction at the interface and hermiticity of the total Hamiltonian, Bloch proposed the coupling operator for zero-slope boundary condition [19] (Neumann boundary condition), H_{QP} as

$$H_{QP} = \frac{\hbar^2}{2m}\delta(x-a)\frac{\overrightarrow{\partial}}{\partial x}. \tag{2.19}$$

H_{PQ} depends on the boundary condition for asymptotic wavefunction. If we choose the wavefunction zero boundary condition (Dirichlet boundary condition) at asymptotic side of the interface [20, 21], it is given by,

$$H_{PQ} = \frac{\hbar^2}{2m}\delta(x-a)\frac{\overleftarrow{\partial}}{\partial x}, \tag{2.20}$$

where the arrows denote the direction of derivative.

Because the zero-slope boundary condition at the interface and wavefunction zero boundary condition at $x = 0$ in Fig. 2.1, we can expand the scattering wavefunction in the reaction region with a set of basis states which satisfy both boundary conditions,

$$\hat{Q}|\Psi\rangle \; = \; \sum_{j=1}^{\infty} \gamma_j |j\rangle, \tag{2.21}$$

where $|j\rangle$ satisfy a Schrödinger equation in the reaction region.

$$(E_j - H_{QQ})|j\rangle \; = \; 0 \tag{2.22}$$

Since we have chosen the hard wall boundary condition for asymptotic region side at the interface, the asymptotic region wavefunction can be expressed by

$$\langle x|\phi_0(E)\rangle \; = \; A_k \mathrm{sin}(k(x-a)) \equiv \phi_E(x), \tag{2.23}$$

where $k \; = \; \sqrt{2mE/\hbar^2}$, and A_k is a normalization constant. We restrict only positive k to require the orthonormality.

$$\int_a^{\infty} \phi_E(x)\phi_{E'}^*(x)dx \; = \; \delta(E-E') \tag{2.24}$$

From the above othonomalization condition, the normalization constant A_k is obtained as,

$$A_k \; = \; \sqrt{\frac{2}{\pi}}\sqrt{\frac{m}{\hbar^2 k}}. \tag{2.25}$$

In order to calculate the T-matrix (the second term in Eq. (2.18)), we start off to calculate the asymptotic region free Green's function.

$$G_P^0(E) \equiv \frac{1}{E^{(+)} - H_{PP}} \; = \; \int_0^{\infty} \frac{|\phi_0(E')\rangle\langle\phi_0(E')|}{E^{(+)} - E'} dE' \tag{2.26}$$

We have to express a Green's function in position bases because H_{QP} and H_{PQ} are given in position representations. We also consider only a retarded Green's function for appropriate boundary condition.

$$\begin{aligned}\left\langle x' \middle| \frac{1}{E^{(+)} - H_{PP}} \middle| x \right\rangle &= \lim_{\epsilon \to 0} \int_0^\infty \frac{\phi_0(E')(x')\phi_0^*(E')(x)}{E - E' + i\epsilon}\, dE' \\ &= \frac{4m}{\hbar^2 \pi} \lim_{\epsilon \to 0} \int_0^\infty \frac{\sin(k'(x'-a))\sin(k'(x-a))}{(k^2 - k'^2) + i\epsilon}\, dk' \\ &= i\frac{m}{\hbar^2 k}\left(e^{ik(x'+x)}e^{-2ika} - e^{ik(x'-x)}\right), \qquad (2.27)\end{aligned}$$

where we assume $x' > x$. See Appendix A for the evaluation of the integration.

We define a regularized propagator in the reaction region space such as

$$\widetilde{G}_Q \equiv \frac{1}{E - H_{QQ} - H_{QP}\frac{1}{E - H_{PP}}H_{PQ}}. \qquad (2.28)$$

T-matrix can be rewritten by

$$\begin{aligned}\langle \phi_0(E)\,| T |\, \phi_0(E)\rangle &= \left\langle \phi_0(E) \middle| H_{PQ}\widetilde{G}_Q H_{QP} \middle| \phi_0(E) \right\rangle \qquad (2.29) \\ &= \sum_{j,j'=1}^{\infty} \langle \phi_0(E)|H_{PQ}|j'\rangle\langle j'|\widetilde{G}_Q|j\rangle\langle j|H_{QP}|\phi_0(E)\rangle,\end{aligned}$$

where

$$\langle j'|\widetilde{G}_Q|j\rangle = \frac{1}{E - E_j\delta_{j'j} - \langle j'|H_{QP}\ G_P^0\ H_{PQ}|j\rangle}. \qquad (2.30)$$

In order to calculate the last term of the denominator in Eq. (2.30), we consider the derivatives of the free Green's function at the interfaces.

$$\begin{aligned}&\overrightarrow{\frac{\partial}{\partial x'}}\langle x'|G_P^0|x\rangle\overleftarrow{\frac{\partial}{\partial x}}\Bigg|_{x=a,x'=a} \\ &= i\frac{m}{\hbar^2 k}\overrightarrow{\frac{\partial}{\partial x'}}\left(e^{ik(x'+x)}e^{-2ika} - e^{ik(x'-x)}\right)\overleftarrow{\frac{\partial}{\partial x}}\Bigg|_{x=a,x'=a} \\ &= -i\frac{2m}{\hbar^2}k \qquad (2.31)\end{aligned}$$

We define the reaction region wavefunction in a position basis.

$$\langle x|j\rangle \equiv \varphi_j(x) \tag{2.32}$$

The last term in the denominator of Eq. (2.30) is given by,

$$\begin{aligned}
\langle j'|H_{QP}\; G_P^0\; H_{PQ}|j\rangle &= \int_a^\infty \int_a^\infty \langle j'|H_{QP}|x'\rangle\langle x'|G_P^0|x\rangle\langle x|H_{PQ}|j\rangle dx dx' \\
&= \varphi_{j'}(a)\frac{\hbar^2}{2m}\left(-i\frac{2m}{\hbar^2}k\right)\frac{\hbar^2}{2m}\varphi_j(a) \\
&= -i\sqrt{\frac{\hbar^2 k}{2m}}\varphi_{j'}(a)\sqrt{\frac{\hbar^2 k}{2m}}\varphi_j(a). \qquad (2.33)
\end{aligned}$$

Coupling terms in Eq. (2.29) are

$$\begin{aligned}
\langle\phi_0(E)|H_{PQ}|j'\rangle &= \frac{\hbar^2}{2m}A_k\mathrm{sin}(k(x-a))\overleftarrow{\frac{\partial}{\partial x}}\delta(x-a)\varphi_{j'}(x) \qquad (2.34) \\
&= \frac{\hbar^2}{2m}\sqrt{\frac{2m}{\pi\hbar^2 k}}\varphi_{j'}(a),
\end{aligned}$$

$$\begin{aligned}
\langle j|H_{QP}|\phi_0(E)\rangle &= \varphi_j(x)\frac{\hbar^2}{2m}\overrightarrow{\frac{\partial}{\partial x}}\delta(x-a)A_k\mathrm{sin}(k(x-a)) \qquad (2.35) \\
&= \frac{\hbar^2}{2m}\sqrt{\frac{2m}{\pi\hbar^2 k}}\varphi_j(a).
\end{aligned}$$

We plug Eqs.(2.33),(2.34),and (2.35) into Eq. (2.29), then T-matrix, Eq. (2.29), becomes

$$\begin{aligned}
\langle\phi_0(E)\,|T|\,\phi_0(E)\rangle &= \langle\phi_0(E)|H_{PQ}\widetilde{G}_Q H_{QP}|\phi_0(E)\rangle \\
&= \frac{1}{\pi}\sum_{j',j=1}^{\infty}\sqrt{\frac{\hbar^2 k}{2m}}\varphi_{j'}(a)\left(E-H_{in}+i\omega\omega^T\right)^{-1}\sqrt{\frac{\hbar^2 k}{2m}}\varphi_j(a) \\
&= \frac{1}{\pi}\omega^T\frac{1}{E-H_{in}+i\omega\omega^T}\omega, \qquad (2.36)
\end{aligned}$$

where ω is a column vector whose the nth element is $\sqrt{\hbar^2 k/2m}\varphi_n(a)$, and H_{in} is a diagonal matrix which have E_j elements. Hence, $S - matrix$ is

$$\mathbf{S} \;=\; 1 - 2i\omega^T \frac{1}{E - H_{in} + i\omega\omega^T}\omega. \tag{2.37}$$

In ordinary scattering theory, $|\phi_0(E)\rangle$ may be a plane wave rather than a sinusoidal function (for R-matrix theory). Moreover, asymptotic region wavefunction is a combination of incoming plane wave and outgoing plane wave which looks like $\sim e^{-ikx} - Se^{ikx}$. Indeed, we will show that the asymptotic region wavefunction can be expressed the combination of plane waves.

$$\begin{aligned}\langle x|\hat{P}|\Psi\rangle \;&=\; \phi_E(x) + \langle x|G_P^0 T|\phi_0(E)\rangle \qquad (2.38)\\ &=\; \phi_E(x)\\ &+\; \int_a^\infty \int_0^\infty \langle x|G_P^0|x'\rangle\langle x'|\phi_0(E')\rangle\langle\phi_0(E')|T|\phi_0(E)\rangle dE' dx'\end{aligned}$$

After taking the limit $x \to \infty$ and some lengthy algebra (See Appendix B), a scattering wavefunction in the asymptotic region can be expressed by the combination of incoming and outgoing waves such as

$$\Psi_E(x) \;=\; i\sqrt{\frac{m}{2\pi\hbar^2 k}} e^{ika}\left\{e^{-ikx} - e^{-2ika}\left(1 - 2i\omega^T \frac{1}{E - H_{in} + i\omega\omega^T}\omega\right)e^{ikx}\right\}. \tag{2.39}$$

We will show that the S-matrix, Eq. 2.90, can be written in terms of R-matrix in Section 2.4.

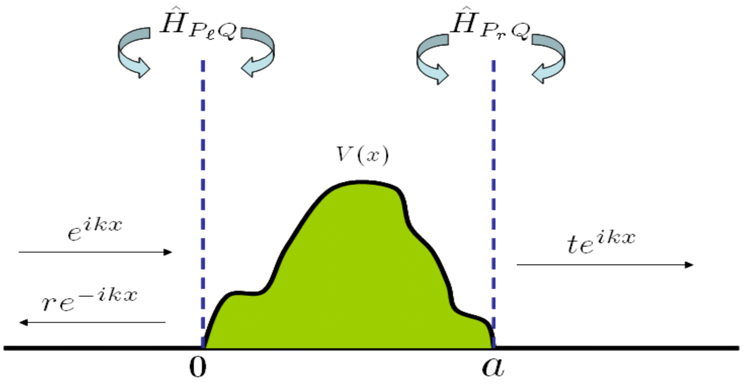

Figure 2.2: Schematic view of one dimensional scattering with an asymptotic region. A particle enter from the left and reflects back due to the hard wall at $x = 0$.

2.3 R-matrix theory for an one dimensional system: II

We considered only one asymptotic region case in the previous section. It was mathematically similar to the case of spherically 3-dimensional scattering. In this section, we will consider two asymptotic regions case which is more suitable for resonance tunneling example or a 1-D quantum wire example. In Fig. 2.2, there is a tunneling barrier and an incident electron from left. Electron can tunnel though the barrier (transmission) or electron can be reflected back at the barrier (reflection). Therefore, we have two asymptotic regions. In this section, we formulate R-matrix theory for one dimensional scattering with two asymptotic regions.

We define the projection operators,

$$\begin{aligned}\hat{P}_\ell &= \int_{-\infty}^{0} dx|x\rangle\langle x| \\ \hat{Q} &= \int_{0}^{a} dx|x\rangle\langle x| \\ \hat{P}_r &= \int_{a}^{\infty} dx|x\rangle\langle x|,\end{aligned} \tag{2.40}$$

which satisfy $\hat{P}_\ell + \hat{Q} + \hat{P}_r = \hat{1}$, $\hat{P}_r\hat{Q} = \hat{P}_\ell\hat{Q} = \hat{P}_r\hat{P}_\ell = 0$, $\hat{P}_r^2 = \hat{P}_r$, and $\hat{P}_\ell^2 = \hat{P}_\ell$.

Using the projection operators, Schrödinger equation can be rewritten by

$$\begin{aligned}(E - H_{P_\ell P_\ell})\hat{P}_\ell|\Psi\rangle &= H_{P_\ell Q}\hat{Q}|\Psi\rangle \\ (E - H_{QQ})\hat{Q}|\Psi\rangle &= H_{QP_\ell}\hat{P}_\ell|\Psi\rangle + H_{QP_r}\hat{P}_r|\Psi\rangle \\ (E - H_{P_r P_r})\hat{P}_r|\Psi\rangle &= H_{P_r Q}\hat{Q}|\Psi\rangle.\end{aligned} \tag{2.41}$$

Asymptotic regions' wavefunctions can be expressed with homogeneous solution $|\phi_1\rangle$ and $\phi_2\rangle$ in each region respectively.

$$\hat{P}_\ell|\Psi\rangle = |\phi_1\rangle + \frac{1}{E - H_{P_\ell P_\ell}} H_{P_\ell Q}\hat{Q}|\Psi\rangle \tag{2.42}$$

$$\hat{P}_r|\Psi\rangle = |\phi_2\rangle + \frac{1}{E - H_{P_r P_r}} H_{P_r Q}\hat{Q}|\Psi\rangle \tag{2.43}$$

We plug the above equations into Eq. (2.42), then the reaction region wavefunction is

$$\begin{aligned}\hat{Q}|\Psi\rangle &= H_{QP_\ell}\left(|\phi_1\rangle + \frac{1}{E - H_{P_\ell P_\ell}} H_{P_\ell Q}\hat{Q}|\Psi\rangle\right) \\ &+ H_{QP_r}\left(|\phi_2\rangle + \frac{1}{E - H_{P_r P_r}} H_{P_r Q}\hat{Q}|\Psi\rangle\right).\end{aligned} \tag{2.44}$$

After plug this in into Eq. (2.42) again, Schrödinger equation for the reaction region is rewritten by

$$\begin{aligned}&\left(E - H_{QQ} - H_{QP_\ell}\frac{1}{E - H_{P_\ell P_\ell}}H_{P_\ell Q} - H_{QP_r}\frac{1}{E - H_{P_r P_r}}H_{P_r Q}\right)\hat{Q}|\Psi\rangle \\ = \;& H_{QP_\ell}\hat{P}_\ell|\phi_1\rangle + H_{QP_r}\hat{P}_r|\phi_2\rangle.\end{aligned} \tag{2.45}$$

We define some propagators such as,

$$\begin{aligned}G^o_{P_\ell}(E) &\equiv \frac{1}{E - H_{P_\ell P_\ell}} \\ G^o_{P_r}(E) &\equiv \frac{1}{E - H_{P_r P_r}} \\ G^o_{Q}(E) &\equiv \frac{1}{E - H_{QQ}} \\ \tilde{G}_Q(E) &\equiv \frac{1}{E - H_{QQ} - H_{QP_\ell}G^o_{P_\ell}H_{P_\ell Q} - H_{QP_r}G^o_{P_r}H_{P_r Q}}\end{aligned} \tag{2.46}$$

Using Eqs.(2.45) and (2.46), asymptotic region wavefunctions, Eqs.(2.42) and (2.43), can be expressed such as,

$$\begin{aligned}\hat{P}_\ell|\Psi\rangle = |\phi_1\rangle &+ G^o_{P_\ell}H_{P_\ell Q}\tilde{G}_Q H_{QP_\ell}\hat{P}_\ell|\phi_1\rangle \\ &+ G^o_{P_\ell}H_{P_\ell Q}\tilde{G}_Q H_{QP_r}\hat{P}_r|\phi_2\rangle \\ = |\phi_1\rangle &+ G^o_{P_\ell}T_{\ell\ell}\hat{P}_\ell|\phi_1\rangle + G^o_{P_\ell}T_{\ell r}\hat{P}_r|\phi_2\rangle,\end{aligned} \tag{2.47}$$

$$\begin{aligned}\hat{P}_r|\Psi\rangle = |\phi_2\rangle &+ G^o_{P_r}H_{P_r Q}\tilde{G}_Q H_{QP_\ell}\hat{P}_r|\phi_2\rangle \\ &+ G^o_{P_r}H_{P_r Q}\tilde{G}_Q H_{QP_\ell}\hat{P}_\ell|\phi_1\rangle \\ = |\phi_2\rangle &+ G^o_{P_r}T_{rr}\hat{P}_r|\phi_2\rangle + G^o_{P_r}T_{r\ell}\hat{P}_\ell|\phi_1\rangle.\end{aligned} \tag{2.48}$$

After we take $\langle x|$ to both asymptotic regions and take the limit $x \to -\infty$, asymptotic wavefunction at $x < 0$ can be written by

$$\begin{aligned}
\langle x|\hat{P}_\ell|\Psi\rangle &= \sqrt{\frac{2m}{\pi\hbar^2 k}}\frac{e^{ika}}{2i}\left(e^{ikx} - e^{-ikx}e^{-2ika}\right) \qquad (2.49)\\
&+ \sqrt{\frac{2m}{\pi\hbar^2 k}}\frac{e^{ika}}{2i}\left(2\pi i\langle\phi_1|T_{\ell\ell}|\phi_1\rangle e^{-ikx}e^{-2ika} + 2\pi i\langle\phi_1|T_{\ell r}|\phi_2\rangle e^{ikx}e^{-2ika}\right)\\
&= \sqrt{\frac{2m}{\pi\hbar^2 k}}\frac{e^{ika}}{2i}\left(1 - 2\pi i\langle\phi_1|T_{\ell r}|\phi_2\rangle e^{-2ika}\right)e^{ikx}\\
&+ \sqrt{\frac{2m}{\pi\hbar^2 k}}\frac{e^{ika}}{2i}\left(1 - 2\pi i\langle\phi_1|T_{\ell\ell}|\phi_1\rangle e^{-2ika}\right)e^{-ikx},
\end{aligned}$$

where T-matrices are defined such as

$$\begin{aligned}
T_{\ell\ell} &= H_{P_\ell Q}\frac{1}{E - H_{QQ} - H_{QP_\ell}G^o_{P_\ell}H_{P_\ell Q} - H_{QP_r}G^o_{P_r}H_{P_r Q}}H_{QP_\ell} \qquad (2.50)\\
T_{\ell r} &= H_{P_\ell Q}\frac{1}{E - H_{QQ} - H_{QP_\ell}G^o_{P_\ell}H_{P_\ell Q} - H_{QP_r}G^o_{P_r}H_{P_r Q}}H_{QP_r},
\end{aligned}$$

In the calculation, we also consider only the retarded Green's function. Similarly, we can compute the wavefunction in the asymptotic region at $x \to \infty$, such as

$$\begin{aligned}
\langle x|\hat{P}_r|\Psi\rangle &= -\sqrt{\frac{2m}{\pi\hbar^2 k}}\frac{e^{ika}}{2i}\Big\{e^{-ikx} + 2\pi i\langle\phi_r|T_{rr}|\phi_2\rangle e^{ikx}e^{-2ika}\\
&- \left(1 - 2\pi i\langle\phi_r|T_{r\ell}|\phi_\ell\rangle\right)e^{ikx}e^{-2ika}\Big\}, \qquad (2.51)
\end{aligned}$$

where T-matrix operators are

$$\begin{aligned}
T_{r\ell} &= H_{P_r Q}\frac{1}{E - H_{QQ} - H_{QP_\ell}G^o_{P_\ell}H_{P_\ell Q} - H_{QP_r}G^o_{P_r}H_{P_r Q}}H_{QP_r}\\
T_{rr} &= H_{P_r Q}\frac{1}{E - H_{QQ} - H_{QP_\ell}G^o_{P_\ell}H_{P_\ell Q} - H_{QP_r}G^o_{P_r}H_{P_r Q}}H_{QP_r}. \qquad (2.52)
\end{aligned}$$

We know the asymptotic wavefunctions have forms such as

$$\psi_\ell = {}_{x\to-\infty} \left(e^{ikx} - t' e^{-ikx} - r e^{ikx}\right), \tag{2.53}$$

$$\psi_r = {}_{x\to\infty} \left(e^{-ikx} - r' e^{ikx} - t e^{ikx}\right), \tag{2.54}$$

where $r(r')$ and $t'(t)$ are reflection and transmission coefficient, respectively such as

$$t' = -2\pi i\langle\phi_\ell|T_{\ell r}|\phi_r\rangle e^{-2ika} \tag{2.55}$$

$$r = \left(1 - 2\pi i\langle\phi_\ell|T_{\ell\ell}|\phi_\ell\rangle\right) e^{-2ika} \tag{2.56}$$

$$t = -2\pi i\langle\phi_r|T_{r\ell}|\phi_\ell\rangle e^{-2ika} \tag{2.57}$$

$$r' = \left(1 - 2\pi i\langle\phi_r|T_{rr}|\phi_r\rangle\right) e^{-2ika}. \tag{2.58}$$

A S-matrix relates incoming wave and outgoing wave such as,

$$\begin{aligned} \mathrm{S}_{\alpha\beta} &= U^\dagger \left(\delta_{\alpha\beta} - 2\pi i\langle\phi_\alpha|T_{\alpha\beta}|\phi_\beta\rangle\right) U^\dagger \\ &= \begin{pmatrix} \overline{r} & \overline{t}' \\ \overline{t} & \overline{r}' \end{pmatrix}. \end{aligned} \tag{2.59}$$

where $\alpha, \beta = \ell, r$, and U is a diagonal matrix whose matrix elements are e^{ika}, which is the phase factor because of boundary condition for the asymptotic region wavefunction at the interface.

2.4 R-matrix theory for a quasi one dimensional system

In this section, we will formulate the scattering theory by using R-matrix theory for a quasi one-dimensional system which is actually two - dimensional system, but the motion of the particle along the one direction is restricted. For instance, as shown in Fig. 2.3, the wavefunction along the transversal direction is quantized due to the hard walls at the upper and bottom walls. We refer it as *quasi-one dimensional system.* If we consider an electron waveguide mentioned in Chapter 1, confining potential along the transversal direction result in discretization of wavefunction. In a waveguide, it is possible that the longitudinal wavevector would be imaginary if the transversal momentum is large enough. This mode is called an *evanescent mode* in contrast to a propagating mode because it does not propagate. In the previous section, we compute a S-matrix using a formal scattering theory and R-matrix. However, in this section, we will formulate a S-matrix for a waveguide in a slightly different way (wavefunction matching with R-matrix) because it is much easier to account evanescent modes in the computation. However, we will show that the S-matrix computed in this section is equivalent to the previous section's result if we neglect evanescent modes.

We consider an open cavity attached to two semi-infinite leads (waveguides) as seen in Fig. 2.3. According to R-matrix theory, we can expand a scattering wavefunction in a cavity area, so called reaction region, with basis functions $\hat{Q}|j\rangle$ which has a corresponding eigen energy λ_j such that

$$\hat{Q}|\Psi\rangle = \sum_{j=1}^{\infty} \gamma_j \hat{Q}|j\rangle. \tag{2.60}$$

Using the orthonormality of basis function $|j\rangle$ and Eq. (2.42), we can obtain the expansion coefficient γ_j as

$$\gamma_j = \frac{1}{E-\lambda_j}\Big(\langle j|H_{QP_\ell}\hat{P}_\ell|\Psi\rangle + \langle j|H_{QP_r}\hat{P}_r|\Psi\rangle\Big). \tag{2.61}$$

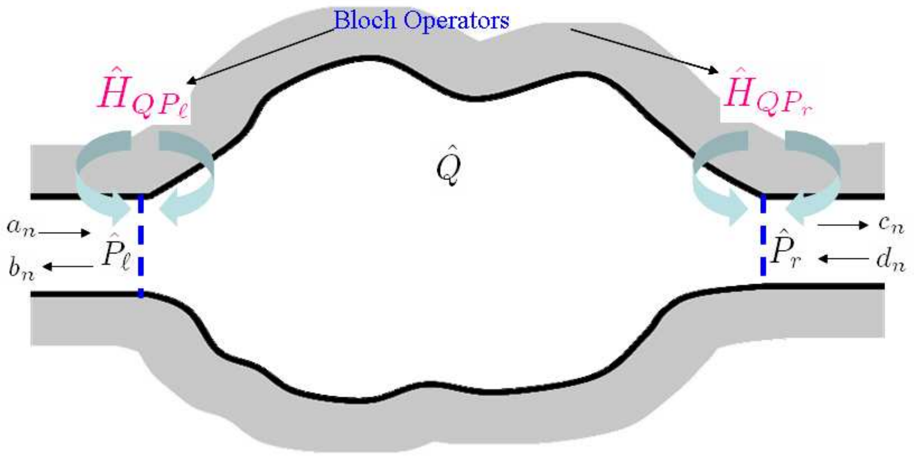

Figure 2.3: A two-dimensional cavity attached to two semi-infinite leads (waveguides).

We also expand the wavefunction in two asymptotic regions because we have discretized transversal modes such as

$$\langle x, y|\hat{P}_\alpha|\Psi\rangle = \sum_{n=1}^{\infty} \Gamma_n^\alpha \chi_n^\alpha(x)\varphi_n(y), \tag{2.62}$$

where $\alpha = \ell, r$, and $\varphi_n(y)$ is the wavefunction for the transversal direction and will form $\varphi_n(y) = \sqrt{2/L}\sin(n\pi y/L)$ if the waveguide has the width L and top and bottom boundaries are hard walls. We must distinguish between propagating modes and evanescent modes in asymptotic regions of the waveguide. The propagating modes are given by

$$\begin{aligned} \Gamma_n^l \chi_{k_n}^l(x) &= \frac{a_n^p}{\sqrt{k_n}} e^{ik_n x} - \frac{b_n^p}{\sqrt{k_n}} e^{-ik_n x} \quad \text{for} \quad x < x_\ell, \\ \Gamma_n^r \chi_{k_n}^r(x) &= \frac{c_n^p}{\sqrt{k_n}} e^{ik_n x} - \frac{d_n^p}{\sqrt{k_n}} e^{-ik_n x} \quad \text{for} \quad x > x_r, \end{aligned} \tag{2.63}$$

where the wave vector k_n is

$$k_n \;=\; \sqrt{\frac{2mE}{\hbar^2} - \left(\frac{n\pi}{L}\right)^2} \tag{2.64}$$

If there are m propagating modes then $n \;=\; 1, 2, ...m$. The evanescent modes $((n\pi/L)^2 > 2m^*E/\hbar^2)$ are given by

$$\begin{aligned} \Gamma^l_n \chi^l_{k_n}(x) &= -\frac{b^e_n}{\sqrt{k_n}} e^{\kappa_n x} \quad \text{for} \quad x < 0, \\ \Gamma^r_n \chi^r_{k_n}(x) &= -\frac{d^e_n}{\sqrt{k_n}} e^{-\kappa_n x} \quad \text{for} \quad x > 2a, \end{aligned} \tag{2.65}$$

where

$$\kappa_n \;=\; \sqrt{\left(\frac{n\pi}{L}\right)^2 - \frac{2m^*E}{\hbar^2}}. \tag{2.66}$$

For evanescent modes, the index $n \;=\; m+1,\, m+2\,.....\infty$

We require that the wavefunction should be continuous at both interfaces between the reaction region (cavity) and asymptotic regions (two leads) at $x = x_\ell, x_r$. Using Eqs.(2.19) and (2.20), it gives us

$$\Gamma^\alpha_n \chi^\alpha_{k_n}(x_\alpha) \;=\; \sum_{n'=1}^{\infty} R_{\alpha l}(n,n') \frac{d\chi^l_{k_{n'}}}{dx}\bigg|_{x_l} \Gamma^l_{n'} - \sum_{n'=1}^{\infty} R_{\alpha r}(n,n') \frac{d\chi^r_{k_{n'}}}{dx}\bigg|_{x_r} \Gamma^l_{n'}, \tag{2.67}$$

where

$$R_{\alpha\beta}(n,n') \;=\; \frac{\hbar^2}{2m^*} \sum_{j=1}^{\infty} \frac{\phi_{j,n}(x_\alpha)\phi_{j,n'}(x_\beta)}{E - \lambda_j} \tag{2.68}$$

is the (n,n')th matrix element of the reaction matrix. The quantity, $\phi_{j,n}(x_\alpha)$, is a measure of the overlap between the jth reaction region state and nth transverse mode in the asymptotic regions. It is defined

$$\phi_{j,n}(x_\alpha) \;=\; \int_0^\infty dy \phi_j(x_\alpha, y)\varphi_n(y) \tag{2.69}$$

We define

$$\overline{a}_p = \begin{pmatrix} a_1^p \\ \vdots \\ a_m^p \end{pmatrix}, \overline{b}_p = \begin{pmatrix} b_1^p \\ \vdots \\ b_m^p \end{pmatrix}, \overline{c}_p = \begin{pmatrix} c_1^p \\ \vdots \\ c_m^p \end{pmatrix}, \overline{d}_p = \begin{pmatrix} d_1^p \\ \vdots \\ d_m^p \end{pmatrix}, \tag{2.70}$$

$$\overline{b}_e = \begin{pmatrix} b_{m+1}^e \\ \vdots \\ b_N^e \end{pmatrix}, \overline{d}_e = \begin{pmatrix} d_{m+1}^e \\ \vdots \\ d_N^e \end{pmatrix}. \tag{2.71}$$

$$\begin{pmatrix} \overline{B}_p \\ \overline{C}_p \end{pmatrix} = \overline{U} \cdot \begin{pmatrix} \overline{b}^p \\ \overline{c}^p \end{pmatrix}, \begin{pmatrix} \overline{A}_p \\ \overline{D}_p \end{pmatrix} = \overline{U}^\dagger \cdot \begin{pmatrix} \overline{a}^p \\ \overline{d}^p \end{pmatrix}, \tag{2.72}$$

where the matrix $\overline{U}$ is a unitary diagonal matrix with matrix elements

$$\overline{U}_{n,n'} = \begin{cases} e^{-ik_n x_\ell}\delta_{nn'} & \text{if } 1 \leq n \leq m \\ e^{-ik_n x_r}\delta_{nn'} & \text{if } m \leq n \leq N \end{cases} \tag{2.73}$$

Using above matrices, we can rewrite Eq. (2.67) as,

$$\begin{pmatrix} \overline{A}_p - \overline{B}_p \\ -\overline{B}_e \\ \overline{C}_p - \overline{D}_p \\ -\overline{D}_e \end{pmatrix} = \overline{K} \cdot \mathbf{R} \cdot \overline{K} \cdot \begin{pmatrix} i(\overline{A}_p + \overline{B}_p) \\ -\overline{B}_e \\ i(\overline{C}_p + \overline{D}_p) \\ -\overline{D}_e \end{pmatrix} \tag{2.74}$$

where $\mathbf{R}$ is the reaction matrix defined as

$$\mathbf{R} = \begin{pmatrix} R_{\ell\ell}(p,p) & R_{\ell\ell}(p,e) & R_{\ell r}(p,p) & R_{\ell r}(e,e) \\ R_{\ell\ell}(e,p) & R_{\ell\ell}(e,e) & R_{\ell r}(e,p) & R_{\ell r}(e,e) \\ R_{r\ell}(p,p) & R_{r\ell}(p,e) & R_{rr}(p,p) & R_{rr}(e,e) \\ R_{r\ell}(e,p) & R_{r\ell}(e,e) & R_{rr}(e,p) & R_{rr}(e,e) \end{pmatrix}, \tag{2.75}$$

and the matrix $\overline{K}$,

$$\overline{K} \equiv \begin{pmatrix} \overline{K}_p & \dots & \dots & 0 \\ \vdots & \overline{K}_e & \ddots & \vdots \\ \vdots & \ddots & \overline{K}_p & \vdots \\ 0 & \dots & \dots & \overline{K}_e \end{pmatrix}, \tag{2.76}$$

where $\overline{K}_p$ is a diagonal matrix with elements $\sqrt{k_n}$ $(n = 1, ..., m)$ and $\overline{K}_e$ is a diagonal matrix with elements $\sqrt{\kappa_n}$ $(n = m+1, ...N)$. In these equations, the subscript p (e) denotes propagating (evanescent) modes. If we consider total N modes and there are m propagating modes for a given Fermi energy, $R_{ll}(p,p)$ is an $m{\times}m$ matrix, $R_{ll}(p,e)$ is an $m{\times}(N-m)$ matrix, $R_{ll}(e,e)$ is an $(N-m){\times}(N-m)$ matrix, $\overline{K}_p$ is $m \times m$ diagonal matrix and $\overline{K}_e$ is $(N-m) \times (N-m)$ diagonal matrix.

After a lengthy linear algebra calculation, the matrices $\overline{B}_e$ and $\overline{D}_e$, which involve evanescent modes, can be expressed in terms of matrices $\overline{A}_p$, $\overline{B}_p$, $\overline{C}_p$, and $\overline{D}_p$ which involve propagating modes and we obtain the following expressions

$$\overline{B}_e = i\overline{Q}_0\,\overline{Q}_1\,(\overline{A}_p\,+\,\overline{B}_p)\,+\,i\overline{Q}_0\,\overline{Q}_2\,(\overline{C}_p\,+\,\overline{D}_p) \tag{2.77}$$

and

$$\begin{aligned} D_e = i\overline{Y}\{\; & (\overline{K}_e R_{rl}(e,p)\overline{K}_p\,-\,\overline{K}_e R_{rl}(e,e)\overline{K}_e\,\overline{Q}_0\,\overline{Q}_1)\overline{A}_p\,+\,\overline{B}_p) \\ & +(\overline{K}_e R_{rr}(e,p)\overline{K}_p\,-\,\overline{K}_e R_{rl}(e,e)\overline{K}_e\,\overline{Q}_0\,\overline{Q}_2)(\overline{C}_p\,+\,\overline{D}_p)\} \end{aligned} \tag{2.78}$$

where

$$\overline{Q}_0\;=\;-\frac{1}{\mathbf{1_e}\,-\,\overline{K}_e R_{ll}(e,e)\overline{K}_e\,+\,\overline{K}_e R_{rl}(e,e)\overline{K}_e\,\overline{Y}\,\overline{K}_e R_{rl}(e,e)\overline{K}_e}, \tag{2.79}$$

$$\overline{Q}_1\;=\;\overline{K}_e R_{ll}(e,p)\overline{K}_p\,-\,\overline{K}_e R_{lr}(e,e)\overline{K}_e\,\overline{Y}\,\overline{K}_e R_{rl}(e,p)\overline{K}_p, \tag{2.80}$$

$$\overline{Q}_2\;=\;\overline{K}_e R_{lr}(e,p)\overline{K}_p\,-\,\overline{K}_e R_{lr}(e,e)\overline{K}_e\,\overline{Y}\,\overline{K}_e R_{rr}(e,p)\overline{K}_p, \tag{2.81}$$

and

$$\overline{Y}\;=\;-\frac{1}{\mathbf{1_e}\,-\,\overline{K}_e R_{rr}(e,e)\overline{K}_e}. \tag{2.82}$$

In the above equations, $\mathbf{1_e}$ is the $(N-m)\times(N-m)$ identity matrix. If we substitute Eqs. (2.77) and (2.78) into Eq. (2.74), we obtain an equation relating the amplitudes of the propagating modes,

$$\begin{pmatrix} \overline{A}_p - \overline{B}_p \\ \\ \overline{C}_p - \overline{D}_p \end{pmatrix} = i \begin{pmatrix} \overline{Z_1} & \overline{Z_2} \\ \\ \overline{Z_3} & \overline{Z_4} \end{pmatrix} \begin{pmatrix} \overline{A}_p + \overline{B}_p \\ \\ \overline{C}_p + \overline{D}_p \end{pmatrix}$$

where

$$\overline{Z}_1 = \overline{K}_p R_{ll}(p,p)\overline{K}_p - \overline{K}_p R_{ll}(p,e)\overline{K}_e\,\overline{Q}_0\,\overline{Q}_1 - \overline{K}_p R_{lr}(p,e)\overline{K}_e\,\overline{G}_1 \tag{2.83}$$

$$\overline{Z}_2 = \overline{K}_p R_{lr}(p,p)\overline{K}_p - \overline{K}_p R_{ll}(p,e)\overline{K}_e\,\overline{Q}_0\,\overline{Q}_2 - \overline{K}_p R_{lr}(p,e)\overline{K}_e\,\overline{G}_2 \tag{2.84}$$

$$\overline{Z}_3 = \overline{K}_p R_{rl}(p,p)\overline{K}_p - \overline{K}_p R_{rl}(p,e)\overline{K}_e\,\overline{Q}_0\,\overline{Q}_1 - \overline{K}_p R_{rl}(p,e)\overline{K}_e\,\overline{G}_1 \tag{2.85}$$

$$\overline{Z}_4 = \overline{K}_p R_{rr}(p,p)\overline{K}_p - \overline{K}_p R_{rl}(p,e)\overline{K}_e\,\overline{Q}_0\,\overline{Q}_2 - \overline{K}_p R_{rr}(p,e)\overline{K}_e\,\overline{G}_2, \tag{2.86}$$

where The matrices $\overline{Z}_1 \sim \overline{Z}_4$ are all $m\times m$ matrices, and

$$\overline{G}_1 = \overline{Y}\left(\overline{K}_e R_{rl}(e,p)\overline{K}_p - \overline{K}_e R_{rl}(e,e)\overline{Q}_0\overline{Q}_1\right), \tag{2.87}$$

$$\overline{G}_2 = \overline{Y}\left(\overline{K}_e R_{rr}(e,p)\overline{K}_p - \overline{K}_e R_{rl}(e,e)\overline{Q}_0\overline{Q}_2\right). \tag{2.88}$$

The *scattering matrix* **S** relates the outgoing propagating modes to the incoming propagating modes. Using Eq. (2.76), we rewrite the Eq. (2.83) in the form

$$\begin{pmatrix} \overline{b}^p \\ \\ \overline{d}^p \end{pmatrix} = U^\dagger \frac{\mathbf{1}_p - i\mathbf{Z}}{\mathbf{1}_p + i\mathbf{Z}} U^\dagger \begin{pmatrix} \overline{a}^p \\ \\ \overline{c}^p \end{pmatrix} \tag{2.89}$$

where

$$\mathbf{Z} = \begin{pmatrix} \overline{Z_1} & \overline{Z_2} \\ \\ \overline{Z_3} & \overline{Z_4} \end{pmatrix}$$

The matrix $\mathbf{Z}$ is a $2m \times 2m$ matrix.

$$\mathbf{S} = U^{\dagger} \frac{\mathbf{1}_p - i\mathbf{Z}}{\mathbf{1}_p + i\mathbf{Z}} U^{\dagger} = \begin{pmatrix} \overline{r} & \overline{t}' \\ \\ \overline{t} & \overline{r}' \end{pmatrix} \tag{2.90}$$

where $\overline{t}$ and $\overline{t}'$ are $m \times m$ matrices of transmission probability amplitudes and $\overline{r}$ and $\overline{r}'$ are $m \times m$ matrices of reflection probability amplitudes.

We now show that the S-matrix in Eq. (2.90) is equivalent to what we compute from Lippman-Schwinger Equation in the previous section. If the evanescent mode effect is negligible, the matrix $\mathbf{Z}$ is simply written as

$$\begin{aligned} \mathbf{Z} &= \overline{K} \cdot \mathbf{R_1} \cdot \overline{K} \\ &= \omega^T \cdot \frac{1}{E\mathbf{1}_M - H_{in}} \cdot \omega, \end{aligned} \tag{2.91}$$

where $\mathbf{1}_M$ is the $M \times M$ unit matrix, H_{in} is the $M \times M$ matrix of reaction region eigenvalues, $H_{in} = diag\{\lambda_1, ...\lambda_M\}$,

$$\mathbf{R_1} = \begin{pmatrix} R_{\ell\ell}(p,p) & R_{\ell r}(p,p) \\ R_{r\ell}(p,p) & R_{rr}(p,p) \end{pmatrix}, \tag{2.92}$$

and ω is $M \times m$ coupling matrix,

$$\omega_{j,n} = \begin{cases} \omega_{j,n}(x_\ell) = \phi_{j,n}(x_\ell)\sqrt{\frac{\hbar^2 k_n}{2m}} & \text{if} j = 1, ...M, n = 1, ...m \\ \omega_{j,n}(x_r) = \phi_{j,n}(x_r)\sqrt{\frac{\hbar^2 k_n}{2m}} & \text{if} j = 1, ...M, n = m+1, ...N \end{cases} \tag{2.93}$$

We can then rewrite S-matrix such as

$$\mathbf{S} = U^{\dagger} \cdot \left(\mathbf{1}_M - \frac{2i\mathbf{Z}}{\mathbf{1}_M + i\mathbf{Z}} \right) \cdot U^{\dagger}. \tag{2.94}$$

We can rearrange the second part of the Eq.(2.94),

$$\begin{aligned}
\frac{\mathbf{Z}}{\mathbf{1}_M + i\mathbf{Z}} &= \left[\mathbf{1}_M + i\omega^T \frac{1}{E\mathbf{1}_M - H_{in}}\omega\right]^{-1} \omega^T \frac{1}{E\mathbf{1}_M - H_{in}}\omega \\
&= \sum_{j=0}^{\infty}(-i)^j \left(\omega^T \frac{1}{E\mathbf{1}_M - H_{in}}\omega\right)^{j+1} \\
&= \sum_{j=0}^{\infty}(-i)^j \left(BA\right)^{j+1} \\
&= BA + (-i)BABA + (-i)^2 BABABA + \cdots \\
&= B\left(1 + (-i)AB + (-i)^2 ABAB + ...\right) A \\
&= B\left(1 - (-i)AB\right)^{-1} A \\
&= \omega^T \left[\mathbf{1}_M + i\frac{1}{E\mathbf{1}_M - H_{in}}\omega\omega^T\right]^{-1} \frac{1}{E\mathbf{1}_M - H_{in}}\omega \\
&= \omega^T \frac{1}{E\mathbf{1}_M - H_{in} + i\omega\omega^T}\omega \qquad (2.95)
\end{aligned}$$

As a result, it is shown that Eq. (2.94) has the same form as S-matrix which we derive from the formal scattering theory in the previous section.

Chapter 3

Electron Conductance in a waveguide with a single impurity

There is considerable interest in modeling the effect of impurities on electron flow in GaAs/AlGaAs electron waveguides [22]. Models involving a single impurity inside a waveguide have been discussed by Bagwell [23] and by Boese et al. [24], [25]. The combined effect of the impurity potential and backscattering off the walls of the quantum waveguide can give rise to quasibound states and resonance behavior and thereby have an important effect on the conductivity. The use of delta functions to model finite range impurity potentials is very attractive because they can simplify considerably the computations necessary to obtain the conductivity in the presence of impurities. However, as noted in [25] and [8], δ-functions in two or more space dimensions have convergence problems. Because of these convergence problems, some authors have resorted to the use of more complicated potentials such as, for example, the impurity D function in [7] or an one dimensional δ-function for one space dimension and a finite sized potential (a Gaussian) along the other space dimension [25], [7]. However, as we will see, under certain conditions it is possible to use δ-function potentials to model the effects of finite range impurities on the conductivity of electron waveguides.

We are particularly interested in the effects of impurities on the conductance of semiconductor based two-dimensional (2-D) electron waveguides or carbon nanotubes. For this reason we restrict our discussion to electron flow in two space dimensions. The problem of convergence occurs for all types of boundary conditions in 2-D space. In all cases, in order to approximate a finite range potential by a δ-function potential, we must introduce a cutoff on the modes.

3.1 The Delta-function Impurity in 2-D Open Space

The Hamiltonian operator for a single electron of mass m_e in two dimensional open space, in the presence of a δ-function potential located at the origin, can be written

$$\hat{H} = \frac{\hat{p}^2}{2m_e} + V_0 \delta^2(\hat{\mathbf{r}}), \tag{3.1}$$

where $\hat{p}$ is the momentum of the electron and V_0 is the strength of the δ-function potential. The energy Green's function for this system can be written

$$G(\mathbf{r}_1, \mathbf{r}_2) = \langle \mathbf{r}_1 | \frac{1}{E\hat{1} - \hat{H}} | \mathbf{r}_2 \rangle = G_0(\mathbf{r}_1, \mathbf{r}_2) + \frac{V_0\, G_0(\mathbf{r}_1, \mathbf{0}) G_0(\mathbf{0}, \mathbf{r}_2)}{1 - V_0\, G_0(\mathbf{0}, \mathbf{0})}, \tag{3.2}$$

where $G_0(\mathbf{r}_1, \mathbf{r}_2)$ is the free particle energy Green's function

$$G_0(\mathbf{r}_1, \mathbf{r}_2) = \langle \mathbf{r}_1 | \frac{1}{E\hat{1} - \hat{H}_0} | \mathbf{r}_2 \rangle \tag{3.3}$$

and $H_0 = \hat{p}^2/2m_e$. If the δ-function potential is attractive, $V_0 < 0$, we expect that a single bound state exists and the bound state energy is given by a pole of the Green's function. The condition for the pole is $1 - V_0 G_0(\mathbf{0}, \mathbf{0}) = 0$. In two space dimensions, this can be written in the form

$$\frac{1}{\lambda} = -\frac{1}{2\pi}\int_0^\infty \frac{k}{k^2 - B}\,dk \tag{3.4}$$

where $E_B \equiv \hbar^2 B/2m_e$ is a bound state energy and is negative and $\lambda \equiv 2m_e V_0/\hbar^2$. The integrand of the right hand side of Eq. (3.4) diverges logarithmically for large value of k. Note that if the right hand side diverges, the left hand side cannot be non-zero finite value. Thus, in two space dimensions a bound state does not exist as long as the strength of δ-potential V_0 is finite. In a scattering problem, the s wave scattering amplitude is undefined for $V_0 \neq 0$. [9].

We can resolve this difficulty by introducing a cutoff, Λ, on the upper limit of the integration in Eq. (3.4). In other words, if we integrate from 0 to Λ rather than from 0 to ∞, we can obtain a bound state energy, B, given by

$$B = -\Lambda^2 e^{\frac{2\hbar^2\pi}{m_e V_0}}. \tag{3.5}$$

Let us now compare this to the bound state energy in a cylindrical potential of finite radius, a. The Hamiltonian is

$$H = -\frac{\hat{p}^2}{2m_e} + U(r) = E, \tag{3.6}$$

where the potential is

$$U(r) = V_0/\pi a^2, \quad \text{if} \quad 0 < r < a \quad \text{and} \quad U(r) = 0 \quad \text{if} \quad r > a. \tag{3.7}$$

The potential, $U(r)$, becomes a two dimensional δ function in the limit, $a \to 0$. If we solve the Schrödinger equation, $H\psi_E = E\psi_E$, assuming that the wavefunction, ψ_E, and its first derivative are continuous at the surface of cylinder, we obtain the bound state energy,

$$E_B = -\frac{2\hbar^2 e^{-2\gamma}}{m_e a^2} e^{\frac{2\hbar^2\pi}{m_e V_0}} \tag{3.8}$$

where γ is Euler constant($\gamma = 0.577$). If we compare Eq.(3.5) and Eq.(3.8), and require that the δ-function potential give the same bound state energy as the cylinder, we can find that the momentum cutoff Λ is inversely proportional to the radius a of the impurity potential.

3.2 The Conductance for Waveguide with Finite Range Impurity

In this section, we consider a waveguide with a finite range impurity. We model the finite range impurity potential as a disk shape potential

$$V(x,y) = \begin{cases} \frac{V_0}{\pi a^2} & r \leq a \\ 0 & r > a \end{cases} \tag{3.9}$$

where $x = x_0 + r\cos\phi$ and $y = y_0 + r\sin\phi$ for $0 \leq \phi \leq 2\pi$.

The electron conductance G in the waveguide is given by the Landauer's formula and can be expressed in terms of the transmission amplitudes t_{ij} as

$$G = \frac{2e^2}{h} \sum_{i,j}^{m} \mid t_{ij} \mid^2, \tag{3.10}$$

where the e is the electron charge, h is Planck's constant, and the sum extends over all propagating modes. The transmission amplitudes are determined from the S-matrix. For computation of S-matrix, we use R-matrix theory developed in Chapter. 2.

Inside the reaction region, Schrödinger equation of the system is given by

$$-\frac{\hbar^2}{2m^*}\left(\frac{\partial^2}{\partial x^2}+\frac{\partial^2}{\partial y^2}\right)\phi_j(x,y)+V(x,y)\phi_j(x,y) \;=\; E_j\phi_j(x,y). \tag{3.11}$$

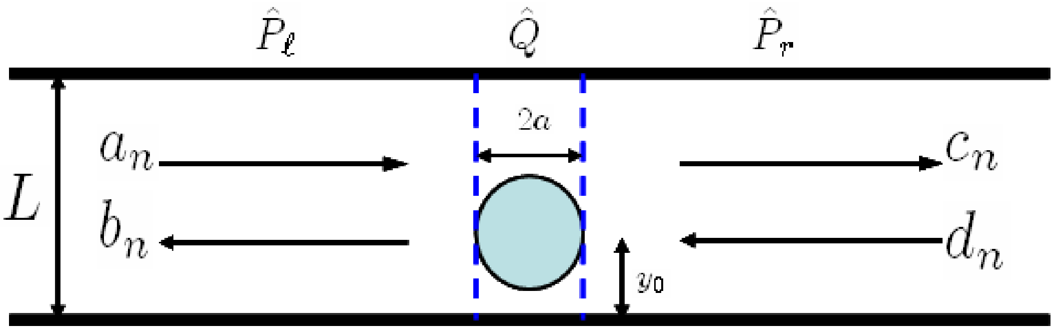

Figure 3.1: The geometry of the two dimensional electron waveguide with a single disk shaped impurity. L is the width of the waveguide. a is the radius of the impurity and y_0 is the transversal position of the impurity. $\hat{P}_\ell$ and $\hat{P}_r$ denote the asymptotic regions and $\hat{Q}$ denotes the reaction region.

As shown in Fig. 3.1, we divide the waveguide into left and right asymptotic regions and a reaction region which contains the impurity. The wavefunction in the reaction region is expanded in a complete orthonormal set of basis states, $\phi_j(x,y)$, which are essentially the eigenstates of a billiard with the finite range impurity centered at (x_o,y_o). The states are zero at the waveguide walls $y=0$ and $y=L$ and they have zero slope at the interfaces $x=0$ and $x=2a$. The eigenvalues associated with these eigenfunctions are denoted λ_j. The states $\phi_j(x,y)\equiv\langle x,y|\phi_j\rangle$ can be expanded in the form

$$\phi_j(x,y) \;=\; \sum_{n=1}^{\infty}\sum_{m=0}^{\infty}B^j_{nm}\sqrt{\frac{2}{L}}\sin\left(\frac{n\pi y}{L}\right)\,A_m\cos\left(\frac{m\pi x}{2a}\right) \tag{3.12}$$

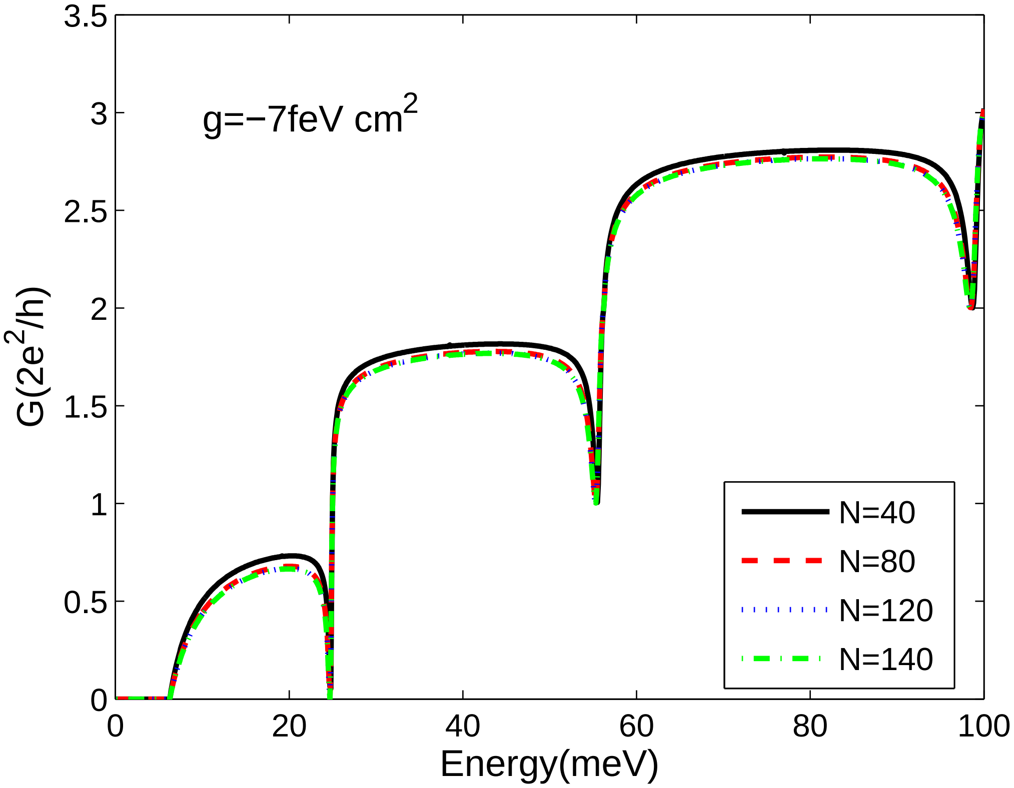

Figure 3.2: Conductance of a waveguide with a finite range impurity for different numbers of modes, N. The impurity is disk shape, the potential strength $g = -7\,\mathrm{feVcm}^2$, and the radius $a = L/150$. When using $N = 120$, the conductance has converged to its final result.

where B^j_{pq} are the expansion coefficients and $A_m = \sqrt{1/2a}$ for $m = 0$ while $A_m = \sqrt{1/a}$ for $m \neq 0$.

In our numerical calculations, we locate the center of the impurity at $x_o = a$ and $y_o = 5L/12$, and we choose $a = L/150$ and $g = -7\text{feVcm}^2$. We consider an attractive impurity here. Fig. 3.2 shows the electron conductance for a waveguide with a finite range impurity, for different total numbers of modes, N (N includes for propagating and evanescent modes). Because of the finite size of the impurity, we obtain convergent results when we use large enough number of modes ($N = 120$ in this case). In Fig. 3.3, the solid line shows the conductance for $N = 120$ and the dashed line is the conductance of a straight waveguide without an impurity present. From Fig. 3.3, we see that the impurity induces resonance and a considerable decrease in the conductance relative to the case when no impurity potential is present. This conductance reduction is due to the electron localization around the impurity, and dips correspond to the quasi bound state [24, 25].

3.3 The Conductance for Waveguide with Delta-function Impurity

Let us now compute the conductance when a δ-function impurity is present at ($x_o = 0$, $y_o = 5L/12$) (this case was also considered in [23] and [24]).

The Green's function for this system is

$$\begin{aligned} G(x,y,x',y',E) &= G^0(x,y,x',y',E) \\ &+ \frac{V_0 G^0(x,y,0,y_0,E) G^0(0,y_0,x',y',E)}{1 - V_0 G^0(0,y_0,0,y_0,E)}, \end{aligned} \tag{3.13}$$

where $G^0(x,y,x',y',E)$ is the Green's function for the free waveguide and is given by

$$G^0(x,y,x',y',E) = \sum_{n=1}^{\infty} \sin\left(\frac{n\pi y}{L}\right) \sin\left(\frac{n\pi y'}{L}\right) \frac{2m^*}{\hbar^2} \frac{e^{ik_n|x-x'|}}{2ik_n} \tag{3.14}$$

(k_n is given as in Sec. 2.4).

The relation between the conductivity and the Green's function was derived by Fisher and Lee [26]. Using the Green's function, we first calculate a transmission matrix and then calculate the conductance. When we construct the Green's function, we keep only N_t modes. However, $(N_t\pi/L)^2$ must be larger than $2m^*E_f/\hbar^2$ where E_f is the Fermi energy so that we include all the propagating modes and at least one evanescent mode.

We use an electron effective mass $m^* = 0.067m_e$ and assume the width of the waveguide is $L = 300$Å. The δ-function impurity potential is $V_i(r) = g\delta^2(\vec{r})$, where g is the strength of the potential. We choose $g = -7\,\mathrm{feVcm}^2$ that ins the same value as in the example in Section 3.2.

In order to determine an appropriate cut-off mode number N_t, we compare the conductance with a δ-function impurity to that for a finite range impurity which was calculated in Sec. 3.2. In Fig. 3.5, we plot the conductance for the finite range disk potential (the solid line) which has radius $a = L/400$,

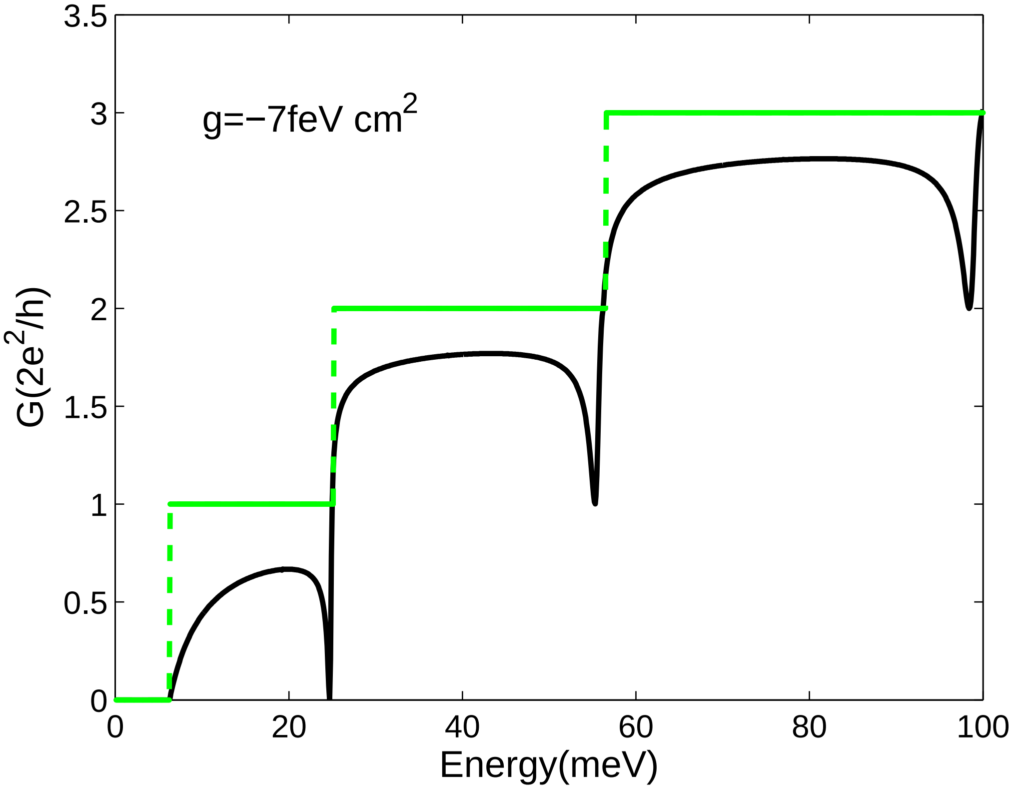

Figure 3.3: Comparison of the conductance of a waveguide with finite range impurity and a waveguide with no impurity. The solid line is for the waveguide with a disk shaped impurity with $g = -7\,\mathrm{feVcm}^2$, $N = 120$, and $a = L/150$. The dotted line is for the waveguide with no impurity. There is a considerable conductance drop due to the electron localization around the impurity, and dips correspond to the quasi bound state.

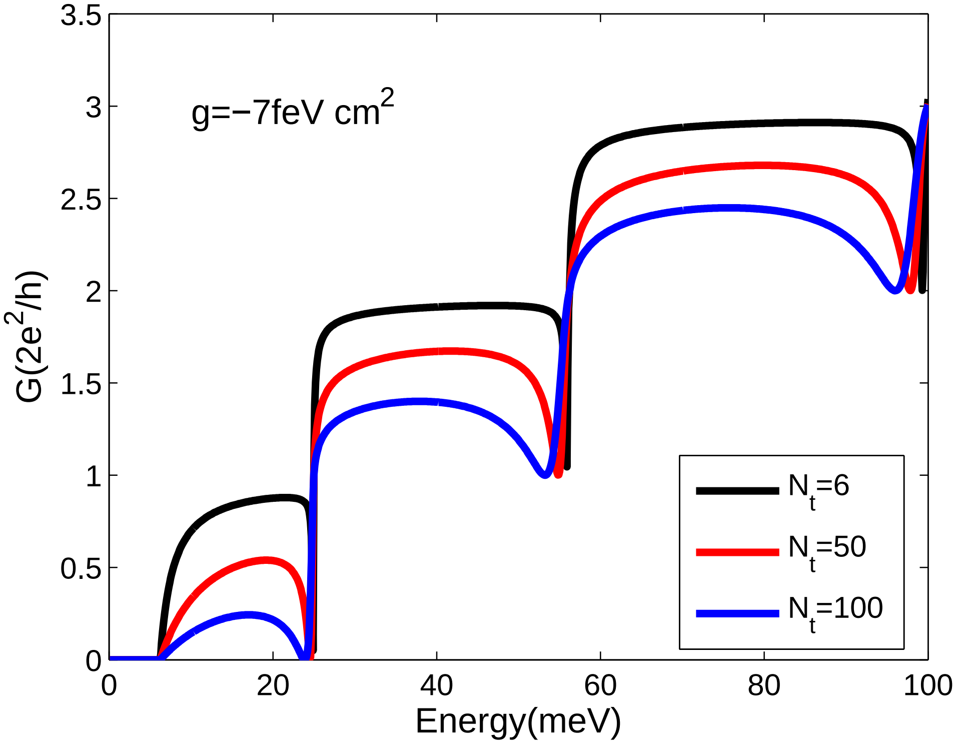

Figure 3.4: Conductance for electron waveguide with a δ-function impurity. N denotes truncate number of modes. It shows conductance do not converge as N increases.

and we plot the conductance for the δ-function potential with several different mode numbers N_t. We see that the conductance for the disk shape impurity and for the δ-function impurity have qualitatively the same properties, namely the reduction of conductance and the appearance of resonances. As shown in Fig. 3.5, the conductance for $N_t = 87$ gives good agreement with the conductance of the disk shape potential.

We define a proportionality constant, μ which relates the cut-off modes and the size of impurity. We can write the total number of modes N_t which gives us good approximation for the finite range impurity, in the form

$$N_t = \frac{L}{2a\mu}, \tag{3.15}$$

where the length scale of the width of the waveguide is L and the impurity length scale is $2a$. For the disk shape impurity in a waveguide, μ is approximately 2.27. We have computed μ for different values of disk diameter $2a$ and the strength g of the potential. The results are shown in Table 3.1. As we change the strength and diameter of the potential significantly, μ only changes slightly. If we replace the disk shape impurity potential with a square shaped impurity, $V_I(x,y) = g/(2a)^2$ for $0 < x < 2a$ and $y_0 - a < y < y_0 + a$, we can again compute μ. The results are shown in Table 3.2. The value of μ is 2.67 with 15% error. Thus, the quantity μ appears to depend more on the geometry of the system than on the size or strength of the impurity.

In open systems, a δ-function impurity only allows s-wave scattering. Scattering from a finite range impurity is predominantly s-wave as long as

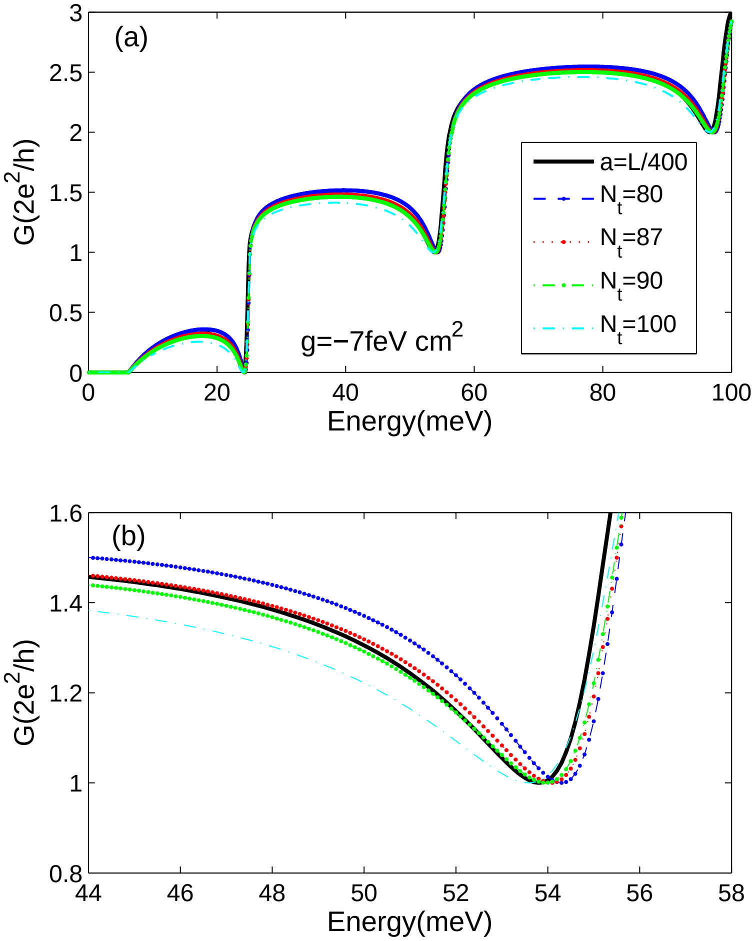

Figure 3.5: (a) Conductance for a waveguide with a single impurity. The solid line is for a disk shape impurity with $g = -7\,\mathrm{feVcm}^2$ and $a = L/400$. All other lines are for a δ-function impurity with a finite number of modes N_t and $g = -7\mathrm{feVcm}^2$. (b) The deviation in the first resonance dip.

Table 3.1: The constant μ for the disk shape potential, diameter $2a$ in a quantum waveguide, width L for different potential strength g and radius.

g(feV cm^2)	$2a$	N_t	μ
-7	$L/50$	23	2.17
	$L/75$	32	2.34
	$L/120$	52	2.31
	$L/200$	87	2.30
-9	$L/50$	22	2.27
	$L/100$	42	2.38
-12	$L/50$	22	2.27
	$L/120$	52	2.31

the wavevector, k, of the incident particle and the range of the potential, a, satisfy the condition $ka \ll 1$ [27]. For the calculations shown in Fig. 3.5, we are in a regime where only a few propagating modes contribute and $k_F a \ll 1$. This appears to be the reason that the δ-function impurity reproduces so well the conductivity for the finite range impurity, at least in regions away from the resonance. As shown in Fig. 3.5 (b), there is a small deviation of the resonance dip positions between the δ-function impurity (dotted line) and the finite range impurity (solid line), although the conductance plateaus have good agreement. Nevertheless the differences are small in the low energy regime. Thus, it appears that we can model a finite range impurity in a two-dimensional waveguide by using a δ-function impurity with a finite number of modes, at least as long as the condition $k_F a \ll 1$ is satisfied.

In a typical quantum point contact experiment, for example, in Ref. [22], the Fermi wavelength $\lambda_F = k_F^{-1}$ is 37 nm ($E_F = 16$meV). In order to satisfy the condition $k_F a \ll 1$, a should be much less than 58.89 Å. Therefore we can apply the delta function approximation for an impurity which has a radius of order of a few Angstrom.

Table 3.2: The constant μ for the square shape potential, width $2a$ in a quantum waveguide, width L for different potential strength g and width

g(feV cm^2)	$2a$	N_t	μ
-7	$L/160$	60	2.67
	$L/240$	78	3.08
-9	$L/80$	30	2.67
-12	$L/160$	60	2.67
	$L/240$	78	3.08

Chapter 4

Ripple Cavity and Chaos

The ripple cavity or ripple waveguide has been used for the study of quantum chaos. Its classical counterpart has a verity of phase space structures which are easily controlled by some parameters. In addition, quantum mechanical Hamiltonian matrix can be written in a analytic form so that many computational necessaries are saved. This chapter consists of three subsections which are the classical dynamics of a ripple cavity, the exact expression of hamiltonian matrix elements, and the quantum version of poincare surface of sections, Husimi functions.

4.1 Classical Dynamics of a ripple cavity

4.1.1 Poincare Surface of Section

Let us consider a ripple cavity as shown in Fig. 4.1 and a particle (electron) bounce off the walls. We assume that collisions are ballistic, then total momentum and kinetic energy are conserved. The width of the cavity is W, the height at the side wall L, the height at the center d, and the ripple amplitude a. A ripple cavity looks like a 2-D box except the upper wall has a ripple. Ripple cause all chaotic motion of a particle inside the cavity. The

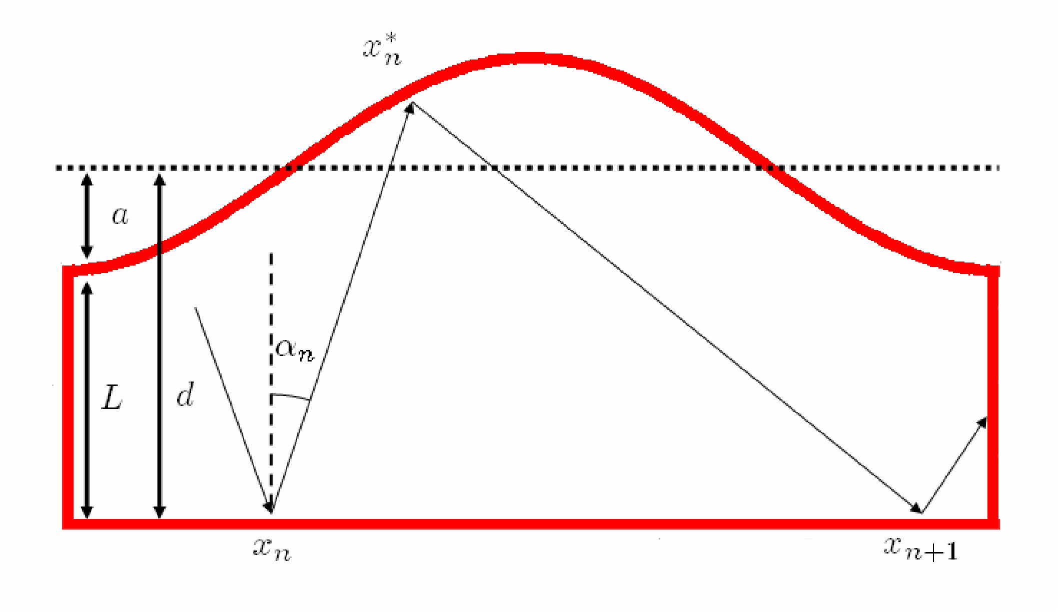

Figure 4.1: A ripple cavity with a side wall height, L and the ripple amplitude, a. A particle bounce off the wall.

ripple can be described by a simple analytic expression such as,

$$f(x) = d - a\cos\left(\frac{2\pi x}{W}\right) \tag{4.1}$$

We will define Birkhoff coordinate $(x_0, \sin\alpha)$ where x_0 is a x-position and $p \cdot \sin\alpha$ is the longitudinal component of the momentum of the particle whenever it hits the bottom wall. There exists a simple map between successive reflection points at the bottom wall [28]. A Poincare map of the trajectory (x_n, α_n) of the particle is given by [28]

$$\alpha_{n+1} = \alpha_n + 2\phi_n, \tag{4.2}$$

$$x_{n+1} = x_n + [d - a\cos(\frac{2\pi x_n^*}{W})][\tan(\alpha_n) + \tan(\alpha_{n+1})], \tag{4.3}$$

with

$$\phi_n = \tan^{-1}\left(\frac{\partial}{\partial x}[d - a\cos\left(\frac{2\pi x}{W}\right)]\right)\Bigg|_{x=x_n^*}, \tag{4.4}$$

where x_n is the position when the particle hits on the nth bounce on the bottom wall, α_n is the scattering angle for nth bounce, and $\tan(\phi_n)$ is the slope of the tangent to the ripple wall at the collision point $x = x_n^*$, where x_n^* is the collision position on the ripple(upper) wall after nth bounce on the bottom wall, and is a function of x_n and α_n. We also use a periodic boundary condition at the left and right vertical boundary for simplicity. If a particle hit one of these side walls, it disappear and another particle come in at the left wall with the same momentum rather than it reflects back ($p_x \rightarrow -p_x$). In the map, Eq. (4.2) and (4.3), we assume that we shoot particles at the center of the bottom wall ($x = W/2$ and $y = 0$) with a initial angle ϕ_0. We iterate its initial condition with the map and plot it whenever the particle hits the bottom wall.

We give the value of a, d, and W. The height of the side walls is then given by $L = d - a$. We plot classical Poincare Surface of Section in Birkhoff coordinate $(x_0, \sin\alpha)$ for four different values of a. They show different classical phase space structures depending on the ripple amplitudes a. It implies that a ripple cavity is useful for quantum chaos study because its chaocity is easily controlled by the value of the parameter a. Fig. 4.2(a) shows the regular motion of particle while the particle moves in a fully chaotic ways in Fig. 4.2 (d). In Fig. 4.2 (b) and (c), two areas (regular islands and chaotic sea) exist simultaneously. This system is called a *mixed phase space system* (mixed system). In Fig. 4.2 (c), once a particle starts off on the KAM island or island chain, it cannot escape from the island or island chain and *vice versa.* As a result, all three areas are clearly separated even though it is energetically allowed.

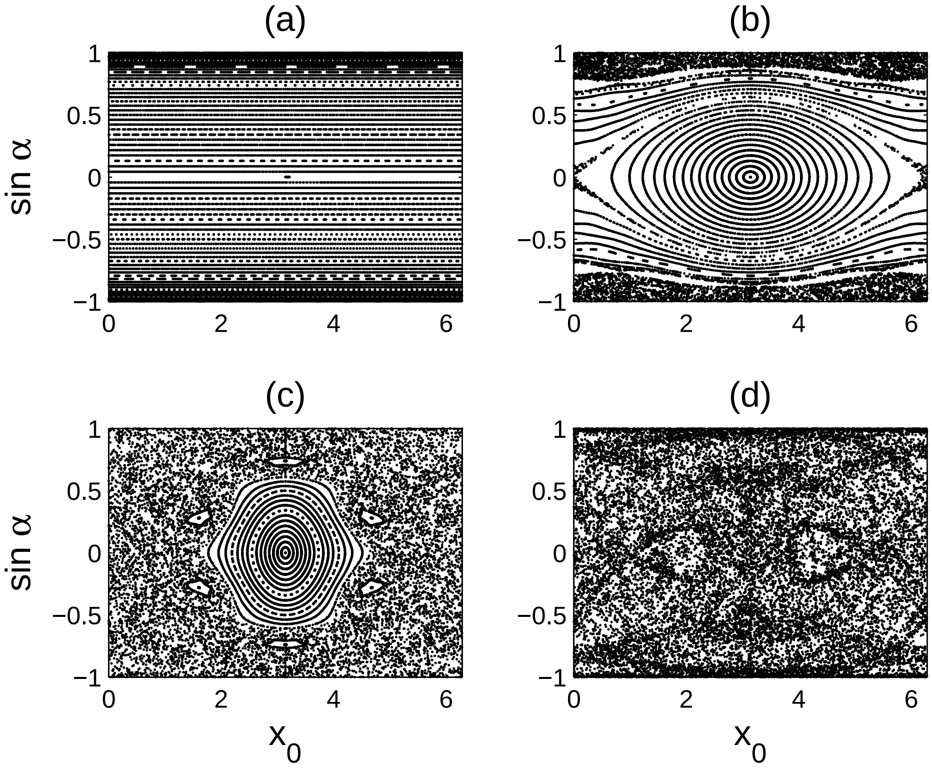

Figure 4.2: Poincare surface of sections in Birkhoff coordinate for a ripple cavity with L=0.7 and $W = 2\pi$ and the ripple amplitude (a) $a = 0$, (b) $a = 0.1$, (c) $a = 0.3$, (d) $a = 0.8$

4.1.2 Homoclinic and Heteroclinic Tangle

For the mixed phase system, the chaotic motion of the particle is generated by the underlying horseshoe structure [1, 29]. In this ripple cavity's phase space, there are three primary fixed points. One of those is located on a center of KAM island and is stable. The others are located at each side wall and are saddle fixed points. A trajectory near a saddle fixed points is unstable along one direction while it is stable along another direction. Near a saddle fixed point, stable and unstable manifolds are formed. The set of initial points that converge to the saddle is called the *stable manifolds* of the saddle fixed point. The set diverge from the saddle is called the *unstable manifolds*. A schematic picture of the stable and unstable manifold of a saddle fixed point P is shown in Fig. 4.3. It is possible that these manifolds intersect each other. We call these intersections homoclinic points(intersections). In principle, there must be infinite number of homoclinic points if unstable and stable manifolds intersect at least at one point. This set of homoclinic points is called *homoclinic tangle*. Trajectories moving near the homoclinic points are repelled by and attracted to the saddle points iteratively. This behavior looks chaotic.

If we consider a rectangle of initial points surrounding the saddle point, the points of the rectangle are stretched out along the unstable manifolds and are compressed along the stable manifolds as the system evolves. The stretched rectangle is folded and overlap with the original rectangle. It is similar as the horseshoe map. The dynamics can then be explained by the horseshoe map.

If there are more than two saddle points and intersections of unstable

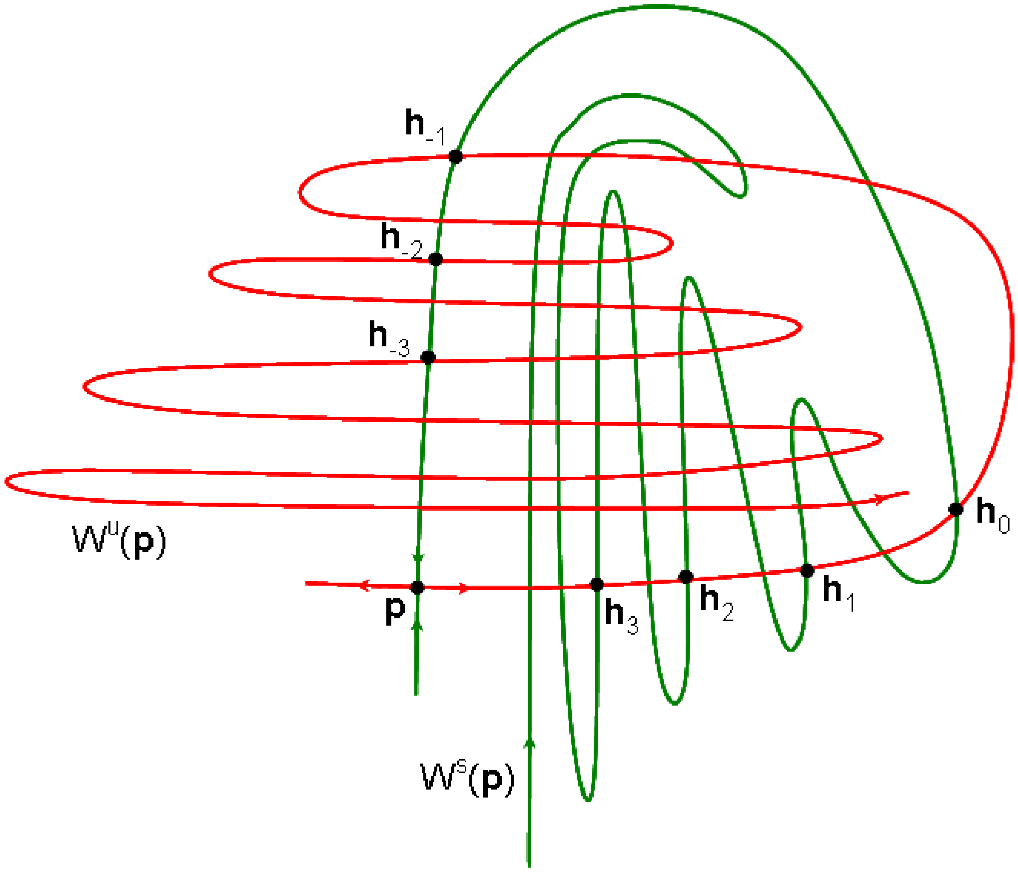

Figure 4.3: Sketch of stable($W^s(\mathbf{P})$) and unstable($W^u(\mathbf{P})$) manifolds for a saddle point P. Intersections of these manifolds form homoclinic points ($\mathbf{h}_n$). (from Ref. [30])

manifolds of a saddle point and stable manifolds of another saddle, these intersections are called *heteroclinic points*. Dynamical structure can be understood in the same way for homoclinic's.

For a ripple cavity, we have two saddle points at $x = 0$ and $x = W$. We denote P_1 and P_2, respectively. First we compute the unstable manifolds for the saddle P_1. In order to compute these manifolds, we linearize the map used in the previous subsection near a saddle fixed point at the left side wall ($x \approx 0$ and $\alpha \approx 0$). In this linear analysis, we consider the case $W = 2\pi$.

$$\begin{aligned} x_n &= 0 + \Delta x_n, && (4.5) \\ x_n^* &= 0 + \Delta x_n^*, && (4.6) \end{aligned}$$

where x_n^* is a solution of the equation,

$$d - a\cos(x_n^*) = \cot(\alpha_n)x_n^* - \cot(\alpha_n)x_n^*. \tag{4.7}$$

We solve it for x_n^* and linearize it such as

$$\Delta x_n^* = \Delta\alpha_n(d - a) + \Delta x_n. \tag{4.8}$$

We linearize the map Eqs. (4.2) and (4.3) by using Eq.(4.8) and

$$\Delta\phi_n = \tan(a\Delta x_n^*) = a\Delta x_n^*. \tag{4.9}$$

The linearized map is given in a matrix form as

$$\begin{pmatrix} \Delta\alpha_{n+1} \\ \Delta x_{n+1} \end{pmatrix} = \mathbf{M} \begin{pmatrix} \Delta\alpha_n \\ \Delta x_n \end{pmatrix}, \tag{4.10}$$

where

$$\mathbf{M} \;=\; \begin{pmatrix} 1+2da-2a^2 & 2a \\ 2(a(d^2-1)+d-2da^2+a^3) & 1+2da-2a^2 \end{pmatrix}. \tag{4.11}$$

One of the eigen values of the matrix $\mathbf{M}$ is greater than 1, which corresponds to the unstable manifolds. The other eigenvalue is smaller than 1 which corresponds to the stable manifolds. Corresponding eigen vectors indicate the evolution direction of manifolds near the saddle fixed point. For computation of unstable manifolds, we select a set of N points($\mathbf{k}_j$) called a segment S_0 between $\mathbf{p}_i$ and $\mathbf{p}_f$ such as

$$\mathbf{p}_i \;=\; \mathbf{u}\times\ell\times\frac{1}{\lambda_u} \tag{4.12}$$

$$\mathbf{p}_f \;=\; \mathbf{u}\times\ell, \tag{4.13}$$

where λ_u and $\mathbf{u}$ are the eigenvalue and the eigen vector for unstable manifolds, respectively. ℓ is a scaling factor.

$$\mathbf{k}_j \;=\; \mathbf{p}_i\times\exp\left(\log\lambda_u\times\frac{j}{N}\right) \tag{4.14}$$

Finally, we get the unstable manifolds for a saddle fixed point at $x=0$ after we evolute the segment S_0. We also compute the unstable manifolds for the saddle fixed point at $x=2\pi$ in a similar method. For stable manifolds, we use the same method for the unstable manifolds, but we take time reversal operator($p_x \to -p_x$) when we evolute the segment S_0. We then have images of S_0 such as $S_{-1}, S_{-2}, S_{-3}\cdots$.

Fig. 4.4 shows the stable and unstable manifolds for two fixed points of the ripple cavity. Solid (dashed) lines represent stable (unstable) manifolds.

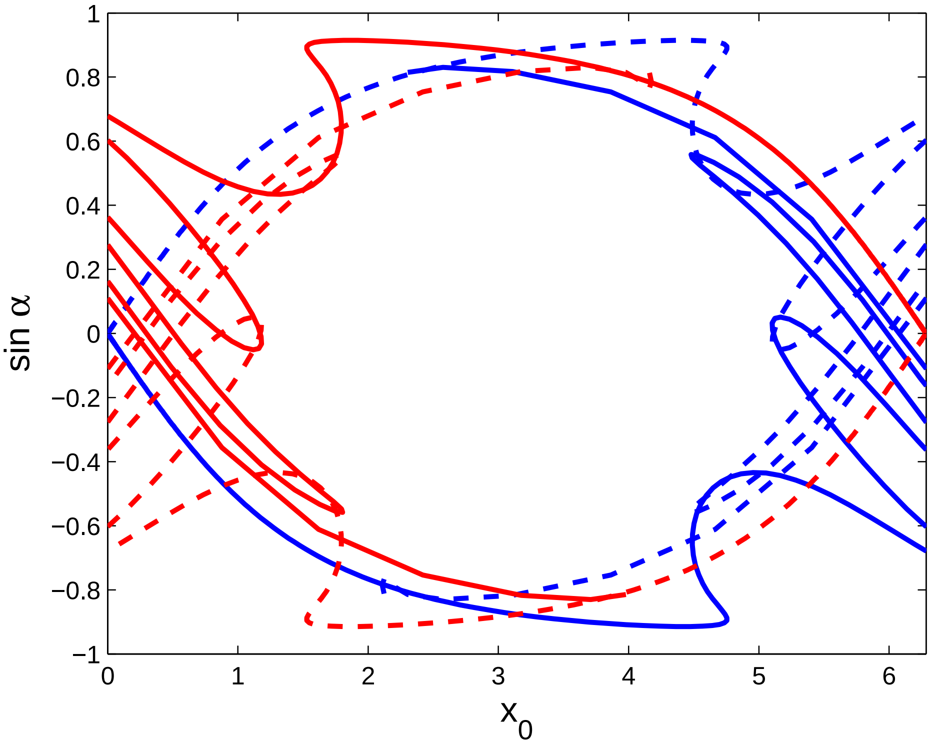

Figure 4.4: Stable(solid) and unstable(dashed) manifolds of two fixed points near the side walls in a ripple cavity for a $L = 0.7$ and $a = 0.3$.

Unstable manifolds of a saddle intersect its stable manifolds (homoclinic) or another saddle's stable manifolds (heteroclinic). These homoclinic (heteroclinic) points form homoclinic (heteroclinic) tangle near the side wall.

We now consider a ripple cavity whose side walls are open. A particle comes in from the left hand side of the cavity, then it bounce around in the cavity. It finally escape to the right hand side (transmission) or back to the left hand side (reflection). In Fig. 4.5, we plot Poincare Surface of Section for a open ripple cavity overlaid by the manifolds. It is clearly seen that four manifolds build up a (partial) boundary for inside and outside regions. Trajectories inside chaotic sea are able to come out only through gaps $G_1, G_2, \cdots$ denoted in Fig. 4.5. Hence, the (partial) boundary is called a *partial transport barrier.* For a closed ripple cavity, there also exists the same partial transport barrier built by manifolds. Trajectories inside and outside chaotic sea exchange each other only through these gaps.

4.2 Hamiltonian Matrix of a ripple cavity

In this section, we examine the quantum mechanical behavior of a particle in a ripple cavity which we consider in the previous section. In order to study the quantum mechanical motion of a ballistic particle in a ripple cavity, we need to solve a Schördinger Equation,

$$-\frac{\hbar^2}{2m}\left(\frac{\partial^2}{\partial x^2}+\frac{\partial^2}{\partial y^2}\right)\Psi(x,y)=E\Psi(x,y). \tag{4.15}$$

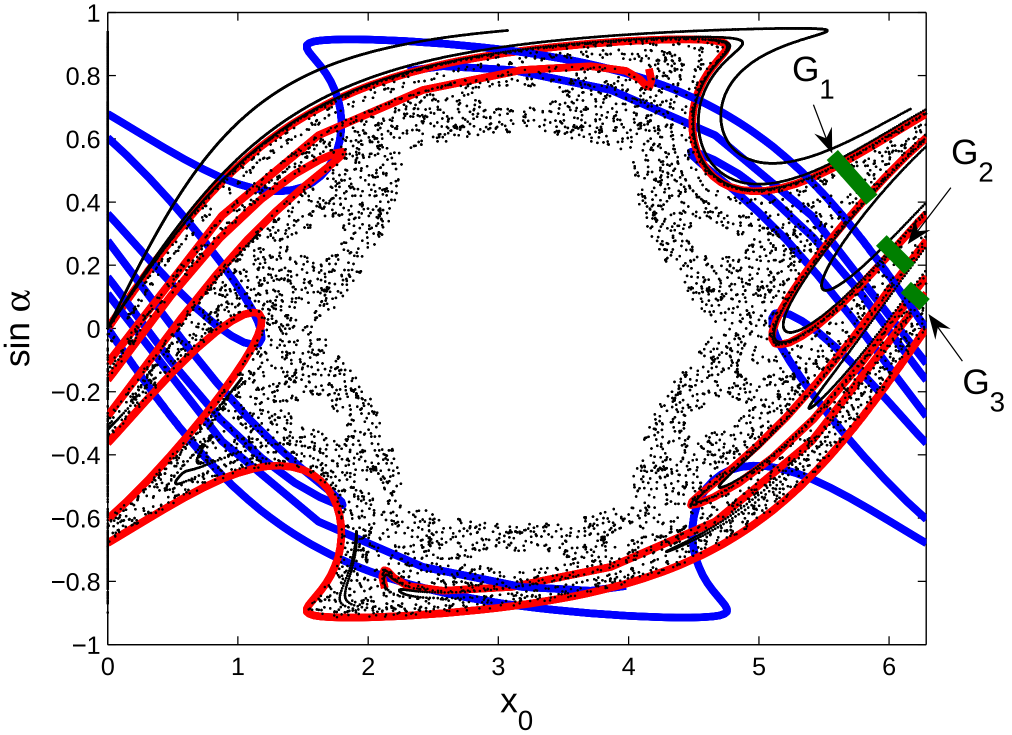

Figure 4.5: Poincare surface of section for a open ripple cavity with the same parameters as ones used for Fig. 4.4. Stable (blue) and unstable (red) manifolds are superimposed. Green line indicate gaps.

Adapting appropriate boundary condition at the upper wall, we introduce a coordinate transformation used in Ref. [13, 14, 28, 31] such as,

$$u = x, \; v = \frac{y}{f(x)}, \tag{4.16}$$

where $f(x) = d - a\cos(2\pi x/W)$ which describe a shape of upper wall boundary.

Using the chain rule, first derivatives of x and y are

$$\begin{aligned} \frac{\partial}{\partial x} &= \frac{\partial u}{\partial x}\frac{\partial}{\partial u} + \frac{\partial v}{\partial x}\frac{\partial}{\partial v} &(4.17)\\ &= \frac{\partial}{\partial u} + \left(-\frac{f'}{f}v\right)\frac{\partial}{\partial v}, &(4.18)\end{aligned}$$

$$\frac{\partial^2}{\partial x^2} = \frac{\partial^2}{\partial u^2} - \frac{f''f - f'^2}{f^2}v\frac{\partial}{\partial v} - 2\frac{f'}{f}v\frac{\partial}{\partial u}\frac{\partial}{\partial v} + \frac{f'^2}{f^2}v\frac{\partial}{\partial v} + \frac{f'^2}{f^2}v^2\frac{\partial^2}{\partial v^2}, \tag{4.19}$$

$$\frac{\partial^2}{\partial y^2} = \frac{1}{f^2}\frac{\partial^2}{\partial v^2}, \tag{4.20}$$

where $f' = \partial f/\partial x$. Thus, the total Hamiltonian is transformed such as

$$\begin{aligned} H &= -\frac{\hbar^2}{2m}\left(\frac{\partial^2}{\partial x^2} + \frac{\partial^2}{\partial y^2}\right) &(4.21)\\ &= -\frac{\hbar^2}{2m}\left(\frac{\partial^2}{\partial u^2} + h_1\frac{\partial^2}{\partial v^2} + h_2\frac{\partial}{\partial u}\frac{\partial}{\partial v} + h_3\frac{\partial}{\partial v}\right), &(4.22)\end{aligned}$$

where

$$\begin{aligned} h_1 &= \frac{f'^2}{f^2}v^2 + \frac{1}{f^2} = \frac{1 + (vf')^2}{f^2} &(4.23)\\ h_2 &= -\frac{2vf'}{f} &(4.24)\\ h_3 &= -\frac{vf''}{f} + \frac{2vf'^2}{f^2}. &(4.25)\end{aligned}$$

We then rewrite the Schrödinger equation in $u - v$ coordinate system.

$$H\psi_j(u,v) = \lambda_j\psi_j(u,v) \tag{4.26}$$

We now consider boundary conditions for a ripple cavity. We assume all the boundaries are infinitely hard so that the wavefunction is zero at all boundary.

We can expand the wavefunction $\psi_j(u,v)$ in terms of basis functions which satisfy boundary condition such as

$$\psi_j(u,0) = \psi_j(u,1) = \psi_j(0,v) = \psi_j(W,v) = 0. \tag{4.27}$$

Wavefunction of jth eigen state is written by

$$\psi_j(u,v) = \sum_{n,m=1}^{\infty} B^j_{mn}\phi_{mn}(u,v), \tag{4.28}$$

where the basis function is

$$\phi_{mn}(u,v) = \frac{2}{\sqrt{W}}\frac{1}{\sqrt{f}}\sin\left(\frac{m\pi u}{W}\right)\sin(n\pi v). \tag{4.29}$$

The matrix elements of the Hamiltonian is given by

$$\begin{aligned} H_{m'n'mn} &\equiv \langle\phi_{m'n'}|H|\phi_{mn}\rangle \qquad (4.30)\\ &= \frac{4}{W}\int_0^W du \int_0^1 dv \frac{1}{\sqrt{f}}\sin(n'\pi v)\sin\left(\frac{m'\pi u}{W}\right) H \\ &\times \frac{1}{\sqrt{f}}\sin(n\pi v)\sin\left(\frac{m\pi u}{W}\right) J \\ &= H^0_{m'n'mn} + H^1_{m'n'mn} + H^2_{m'n'mn} + H^3_{m'n'mn}, \end{aligned}$$

where we require the orthonormality condition,

$$\int\int dudv\phi_{mn}(u,v)\phi_{m'n'}(u,v)J = \delta_{mm'}\delta_{nn'}, \tag{4.31}$$

where J is a Jacobian of integration for coordinate transformation,

$$J = \begin{vmatrix} \frac{\partial x}{\partial u} & \frac{\partial x}{\partial v} \\ \frac{\partial y}{\partial u} & \frac{\partial y}{\partial v} \end{vmatrix} = f(x). \tag{4.32}$$

In Eq.(4.30), each term is given by

$$\begin{aligned} H^0_{m'n'mn} &= \delta_{nn'}\frac{2}{W}\left\{\frac{1}{4}J^5_{mm'} - \frac{1}{2}\left(\frac{m'\pi}{2W}\right)J^2_{mm'}\right. \\ &+ \left.\frac{1}{2}\left(\frac{m\pi}{2W}\right)J^2_{m'm} - \frac{W}{2}\left(\frac{m\pi}{W}\right)^2\delta_{mm'}\right\}, \end{aligned} \tag{4.33}$$

$$H^1_{m'n'mn} = -\frac{2}{W}(n'\pi)^2\left\{\delta_{nn'}J^4_{mm'} + \left(K^2_{m-n'} - K^2_{n+n'}\right)J^5_{mm'}\right\}, \tag{4.34}$$

$$H^2_{m'n'mn} = \frac{2}{W}\left(K^1_{n-n'} + K^1_{n+n'}\right)(n'\pi)\left\{J^5_{mm'} - 2\left(\frac{m'\pi}{W}\right)J^2_{mm'}\right\}, \tag{4.35}$$

$$H^3_{m'n'mn} = \frac{2}{W}(n'\pi)\left(K^1_{n-n'} + K^1_{n+n'}\right)\left(-J^3_{mm'} + 2J^5_{mm'}\right), \tag{4.36}$$

where

$$J^5_{mm'} \equiv \int_0^W du\frac{\sin(\frac{m\pi u}{W})\sin(\frac{m'\pi u}{W})}{f^2(u)}(f'(u))^2 \tag{4.37}$$

$$J^4_{mm'} \equiv \int_0^W du\frac{\sin(\frac{m\pi u}{W})\sin(\frac{m'\pi u}{W})}{f^2(u)} \tag{4.38}$$

$$J^3_{mm'} \equiv \int_0^W du\frac{\sin(\frac{m\pi u}{W})\sin(\frac{m'\pi u}{W})}{f(u)}f''(u) \tag{4.39}$$

$$J^2_{mm'} \equiv \int_0^W du\frac{2\sin(\frac{m\pi u}{W})\cos(\frac{m'\pi u}{W})}{f(u)}f'(u) \tag{4.40}$$

$$K^2_n = \int_0^1 d\nu\nu^2\cos(n\pi\nu) = \begin{cases} \frac{1}{3} & \text{if } n=0 \\ \frac{2(-1)^n}{n^2\pi^2} & \text{otherwise} \end{cases} \tag{4.41}$$

$$K^1_n = \int_0^1 d\nu\nu\sin(n\pi\nu) = \begin{cases} 0 & \text{if } n=0 \\ -\frac{(-1)^n}{n\pi} & \text{otherwise} \end{cases} \tag{4.42}$$

We will consider Neumann boundary condition(the first derivative is zero) for side interfaces for opening of cavity in Chapters 5 and 6. See appendix C for Hamiltonian matrix elements for a ripple cavity with zero-slope boundary condition at the side walls.

4.3 Husimi Function

We can also compute the Husimi function which is a quantum version of Poincare surface of section. The Husimi function is defined as the overlap between wavefunction and coherent state which has the highest probability at x_0 and p_0 in position and momentum basis, respectively.

First, we need to consider a Birkhoff coordinate again to directly compare it with the classical Poincare Surface of section computed in Section 4.1. It means that we will calculate the overlap between wavefunction and a coherent state at the bottom wall. However, as you can see, the wavefunction at the bottom wall is vanished because of the hard wall. Therefore, we will expand the wavefunction near the bottom wall up to the first order as,

$$\Psi(x,y) \;\approx\; 0 + \left.\frac{\partial\Psi(x,y)}{\partial y}y\right|_{y\approx 0} + O(y^2). \tag{4.43}$$

We now define new wavefunction $S(x)$ near the bottom wall such as

$$S(x) \;=\; \left.\frac{\partial\Psi(x,y)}{\partial y}\right|_{y\approx 0}. \tag{4.44}$$

The Husimi function for a ripple cavity is given by

$$H(x_0,p_0) \;=\; \left|\int_0^W S(x)\langle x|x_0,p_0\rangle dx\right|^2, \tag{4.45}$$

where $|x_0,p_0\rangle$ is a coherent state which is a minimum uncertainty wave packet. It has its center at p_0 and x_0 and position representation is given by

$$\langle x|x_0,p_0\rangle \;=\; \left(\frac{\omega}{\pi\hbar}\right)^{\frac{1}{4}}\exp\left(-\frac{\omega}{2\hbar}(x-x_0)^2 + i\frac{p_0}{\hbar}(x-x_0)\right). \tag{4.46}$$

The coherent state has uncertainty $\sigma_x = \sqrt{\hbar/2\omega}$ in position basis and uncertainty $\sigma_p = \sqrt{\hbar\omega/2}$ in momentum basis. The minimum uncertainty of the coherent state is $\sigma_x\sigma_p = \hbar/2$. A parameter ω is chosen by requiring symmetric coarse graining which means $2P_E/\sigma_p = W/\sigma_x$, where $P_E = \sqrt{2m_eE}$. It gives us $\omega = 2P_E/W$. Because of uncertainty principle, a Husimi plot should have a finite resolution which depends on the uncertainty of the coherent state. We then define the maximum resolution, $\hbar_{eff}$ such as

$$\frac{\hbar_{eff}}{2} \equiv \sigma_x\sigma_p/P_E. \tag{4.47}$$

$\hbar_{eff}$ depends on the energy of a system so that $\hbar_{eff}$ decreases as the energy increases. For example, if we consider a ripple cavity constructed in a heterostructure of GaAs/AlGaAs, we use a effective electron mass, $m^* = 0.067m_e$ in GaAs. We also choose the parameters $W = 300\mathring{A}$, $L = 33.42\mathring{A}$, and $a = 13.85\mathring{A}$ which reproduce the same classical phase space structure in the Fig. 4.2 (c). We also assume that the electron energy in the ripple cavity, $E = 5400\text{meV}$. The momentum of an electron is given by

$$P_E = \sqrt{\frac{2m^*c^2E}{(\hbar c)^2}} = 0.308\mathring{A}^{-1}. \tag{4.48}$$

The uncertainties of the coherent state in position basis and in momentum basis are given by

$$\begin{aligned} \sigma_x &= \sqrt{\frac{W}{2P_E}} = 15.60\mathring{A}, && (4.49) \\ \sigma_p/P_E &= \sqrt{\frac{\hbar}{WP_E}} = 0.104. && (4.50) \end{aligned}$$

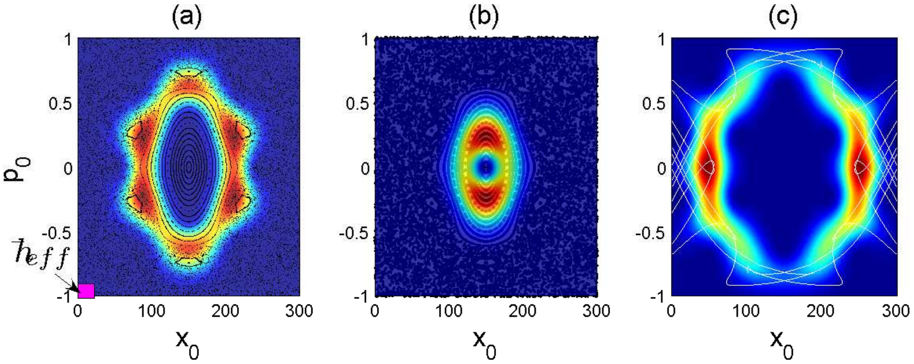

Figure 4.6: Husimi function of (a) 99th, (b)101st, (c) 102nd eigen states of a ripple cavity with the same parameters for Fig. 4.2 (c).

We therefore have a $\hbar_{eff}$ as a rectangle $22.07\mathring{A} \times 0.147$ in a phase space.

Fig. 4.6 shows Husimi functions for a few of eigenstates of the ripple cavity with the same parameters as in Fig. 4.2 (c), and the classical phase space is superimposed on them. Fig. 4.7 shows electron probabilities in the cavity for the same energy eigen states in Fig. 4.6. As shown in Fig. 4.6, those eigen states can be categorized into three different families depending on where high probability region of Husimi function sits on. Fig. 4.6 (a) shows Husimi function of the 99th eigen state sits on the island chain surrounding KAM island. Husimi function sits on the central KAM island area in Fig. 4.6 (b). Fig. 4.6 indicates that the 102th eigen state corresponds to the tangle structure formed by stable and unstable manifolds. We have chosen those states because the eigen energies high enough to show that Husimi distributions sit on three distinctive areas in the classical phase space. In Fig. 4.6 (a), a rectangle shows the size of maximum resolution of the Husimi functions, namely, $\hbar_{eff}$. Since

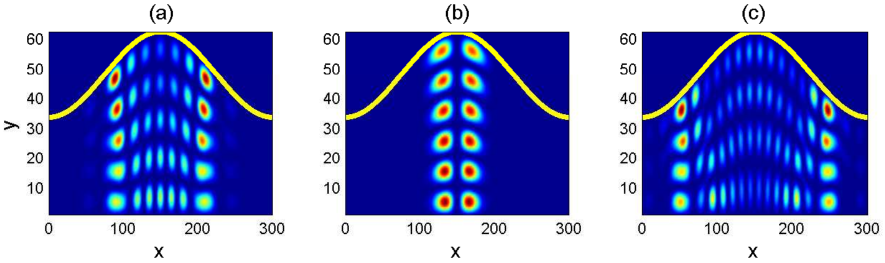

Figure 4.7: Electron probabilities of eigen states corresponding to Fig. 4.6.

the eigen states are relatively low eigen states, $\hbar_{eff}$ is too large to resolve the fractal structure around KAM tori near the island chain.

Chapter 5

Scattering Echoes in a ripple waveguide

Electromagnetic waveguides and electron matter waveguides have been of particular interest in studies of the classical-quantum correspondence because their shape and dimensions and the effective value of Planck's constant are easily controlled. Electromagnetic waveguides, even though they are classical objects, can be constructed to mimic single-particle quantum wave phenomena [32, 33, 34, 35, 36, 37, 38]. Electron matter waveguides and quantum dots formed in the two dimensional electron gas in GaAs/GaAlAs semiconductor heterostructures are also candidates for studying the classical-quantum correspondence because at low enough temperatures the electron flow becomes ballistic and electrons maintain their coherence over relatively long distances [4, 39, 40]. For open quantum systems like waveguides, conductance fluctuations carry much of the information about the internal dynamics of the waveguide.

Systems with mixed classical phase space, which have KAM islands and a chaotic sea surrounding them, are particularly interesting because they have a far richer dynamics (quantum mechanically or classically) than globally chaotic or integrable systems. For example, the dwell time probability $P(t)$, which is a classical quantity, can show power law decay ($P(t) \sim t^{-\gamma}$) [1, 41] in a mixed phase system rather than exponential decay which is characteristic of a chaotic system. In quantum systems, the behavior of the conductance fluctuations is different for classically chaotic systems and systems with mixed phase space. Only smooth variations appear in the conductance fluctuations of a chaotic system. In systems with mixed phase space, sharp isolated resonances can occur on top of the smooth conduction fluctuations. Sharp isolated resonances were found numerically in the conductance fluctuations of the cosine billiard (ripple billiard) for a mixed phase space system [10]. Bird *et al.* also observed these isolated resonances in quantum dots experiments [42] and Backer *et al.* found that the isolated resonances can correspond to resonances associated with regular states (sitting on KAM islands) or the hierarchy states (sitting in the fractal structure surrounding KAM islands) [43, 44] of the corresponding closed billiard. The isolated resonances can also be associated with *scarred* states in the chaotic sea surrounding the KAM island structure [45, 46]. In this chapter, we will focus on resonances associated with the horseshoes (homoclinic/heteroclinic tangles) generated by the outer fixed points of the ripple cavity.

Jung *et al.* [47] showed that a self-pulsing effect (scattering echoes) could be observed in open scattering systems such as a delta kicked one-dimensional scattering system and two-dimensional waveguide. These echoes have been observed numerically in both classical and quantum systems and the period of the echoes can be related to the horseshoe topology in the classical Poincare surface of section. Dembowski *et al.* observed the echoes in a microwave waveguide experiment [37]. Their results reproduce well the theoretically derived value for the period of the echoes. It can be expected that the scattering echoes can also be observed in electron matter waveguides which can be realized in semiconductor heterostructures (*e.g.* GaAs/AlGaAs). We will show that some resonances which appear in the conductance fluctuations of a waveguide with a ripple cavity participate in the scattering echoes and the period of the echoes gives a measure of the horseshoe development of the chaotic layer of the classical system.

Ripple cavities have been used for the study of quantum chaos in both closed and open systems [10, 13, 14, 28, 31, 43] because it is possible to construct analytic expressions for the Hamiltonian matrix elements for these systems. The reaction matrix theory is particularly useful and efficient to compute conductance in a waveguide with a ripple cavity because we only need to compute eigenvalues and eigenvectors of the Hamiltonian matrix once to construct the S-matrix for a range of values of incident energy [13].

This chapter is organized as follows. In Section 5.1, we describe the system which we consider in this paper and show the stable and unstable manifolds which trace out horseshoe development in the Poincare surface of section. From this classical picture, we calculate the theoretical expected value of the period of the scattering echoes. In Section 5.2, we construct the S-matrix for the waveguide with a ripple cavity in order to calculate the conductance of the ripple waveguide. Using Landauer's formula, we can compute the waveguide conductance from the S-matrix. We investigate the resonances associated with the homoclinic/heteroclinic tangles. These resonances have relatively broader width than the resonances associated with the KAM islands. The period of scattering echoes will be obtained by Fast Fourier Transformation(FFT) of the conductance fluctuations. We also construct quantum Poincare surfaces of section using Husimi plots. In Section 5.3, we use Husimi plots to visualize scattering eigenstates associated with the resonances. We then will evaluate the period of echoes using the energy separation of resonances. In Section 5.4, in the time domain we follow a Gaussian wavepacket that scatters through the ripple cavity and we observe the emergence of scattering echoes in the transmitted fragments of the packet.

5.1 Chaotic scattering in a waveguide with a ripple cavity

We study the conduction properties of a ripple cavity(cosine billiard) with two infinite straight leads attached. For this system, we can construct an analytic expression for the Hamiltonian matrix which governs the dynamics inside the cavity [31]. The geometry of the ripple cavity is shown in Fig. 5.1(a). The boundaries are hard walls located at $y = 0$, and

$$y(x) \;=\; d - a\cos\left(\frac{2\pi x}{W}\right) \tag{5.1}$$

for $0 \leq x \leq W$. Straight leads are attached at $x = 0$ and $x = W$.

In Fig. 5.1(b) we show a Poincare surface of section of the classical dynamics in the ripple cavity when $a = 13.846 \mathring{A}$, $d = 47.269 \mathring{A}$, and $W =$

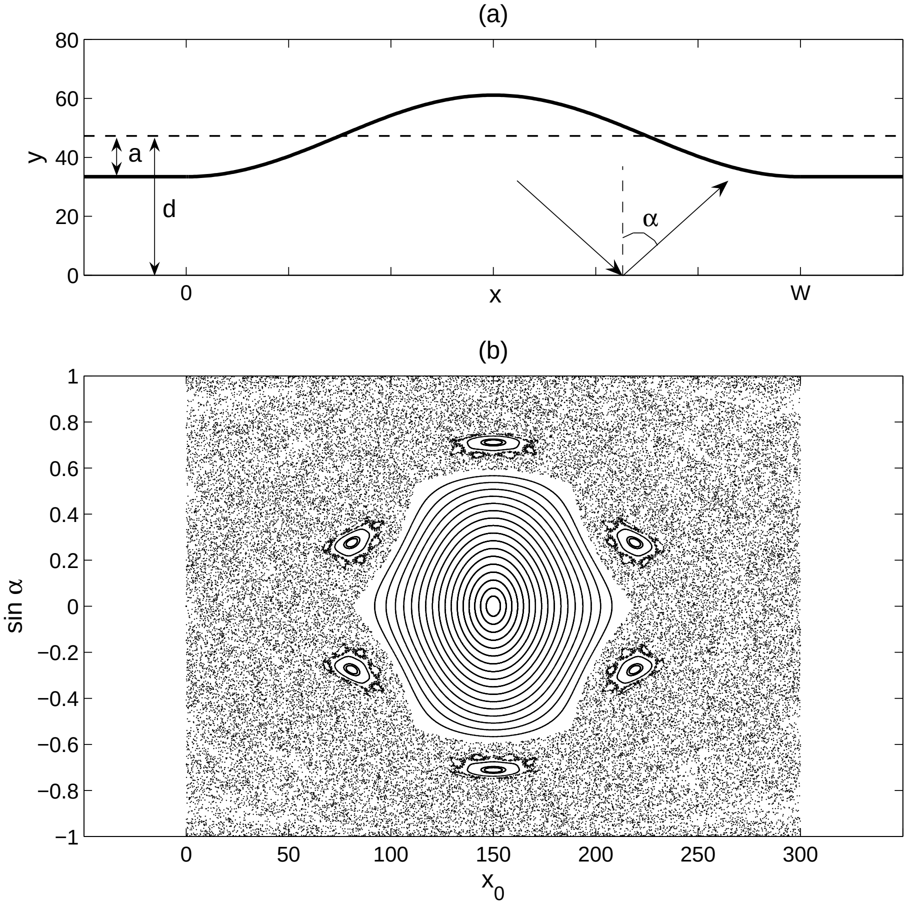

Figure 5.1: (a) The waveguide with ripple cavity for $a = 13.846\text{Å}$, $d = 47.269\text{Å}$ and $W = 300.0\text{Å}$. Leads are attached to the ripple cavity at $x = 0$ and $x = W$. α is the reflection angle at the bottom. (b) The classical Poincare surface of section using Birkhoff coordinates at the bottom boundary ($y = 0$).

$300.0\mathring{A}$. We use Birkhoff coordinates $(x_0, \sin\alpha)$ where x_0 is the x-coordinate and α the reflection angle when the particle hits the bottom boundary (at $y = 0$). The dynamics has a fixed point at the center of cavity $x = W/2$ whose stability depends on the parameters a, d, and W. It also has outer fixed points at $x = 0$ and W. The outer fixed points have an unusual behavior. In the leads, every line for which $x = constant$ is a periodic orbit along the y-direction. Because these orbits form a continuum of absolutely equivalent orbits, they are all parabolic. The lines $x = 0$ and $x = W$ form the interface between the cavity dynamics and the lead dynamics. Therefore the lines $x = 0$ and $x = W$ are periodic orbits which appear to be parabolic when seen from outside (in the leads) and normal hyperbolic when seen from inside the cavity. The corresponding fixed points in the Poincare surface of section have invariant manifolds going to the interior of the cavity region and they trace out the horseshoe (homoclinic/heteroclinic tangle) which acts as the central guiding structure of the chaotic scattering. Because we wish to consider dynamics with a mixed phase space, we will always consider parameters a, d, and W which give us a stable fixed point at $x = W/2$. For the parameters used in Fig. 5.1 (b), there is a large KAM island surrounded by small islands and a chaotic sea. Therefore, for this choice of parameters, the outer fixed points ($x = 0$ and $x = W$) are the outer fixed points of a ternary symmetric horseshoe.

Fig. 5.2 shows the stable and unstable manifolds of the outer fixed points for parameter values given in Fig. 5.1. The intersections of these manifolds form homoclinic/heteroclinic tangles of a ternary horseshoe (three fixed

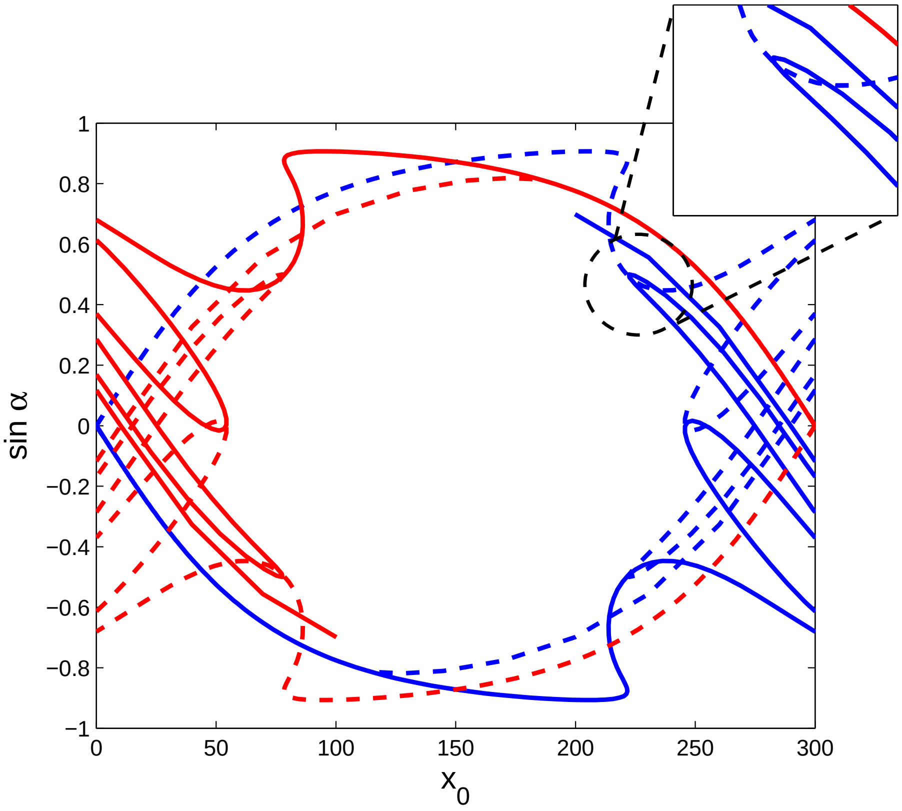

Figure 5.2: The stable and unstable manifolds of the ripple cavity with parameters in given in Fig.5.1. The first tendril of unstable manifold is intersected by the third tendril of stable manifold in two points which implies that the horseshoe development is $\beta = 3^{-3}$. Inset shows two points intersections.

points). In Fig. 5.2, the blue solid and dashed lines represent the stable and unstable manifold, respectively, of the left outer fixed point (fixed point 1). The red solid and dashed lines represent the stable and unstable manifolds, respectively, of the right outer fixed point (fixed point 2). As shown in Fig. 5.2, the third tendril of the stable manifolds intersect the first tendril of unstable manifolds in two points so that the horseshoe development parameter is $\beta = 3^{-3}$ [48]. Inset shows that it makes two points intersection.

The homoclinic/heteroclinic tangles formed by these invariant manifolds yield a chaotic scattering layer [47]. Consider a line of incoming trajectories which passes near the unstable manifold of the fixed point 1. These trajectories enter the chaotic scattering layer and approach fixed point 2 following the unstable manifold of fixed point 1. Depending on the initial conditions, after passing fixed point 2, some trajectories enter the right lead and leave the cavity. The remaining trajectories complete a rotation around the large KAM island and return to the neighborhood of fixed point 1 along the unstable manifold of fixed point 2. After reaching the neighborhood of fixed point 1, some of these trajectories enter the left lead and leave the cavity. The remaining trajectories continue another rotation. (See Fig. 5.3) If we measure the outgoing flux in the leads, we will observe that the flux intensity (transmission and reflection) appears in pulses which are periodic in time. Each pulse is a *scattering echo.*

According to Ref. [47], the period of the scattering echoes, T, is deter-

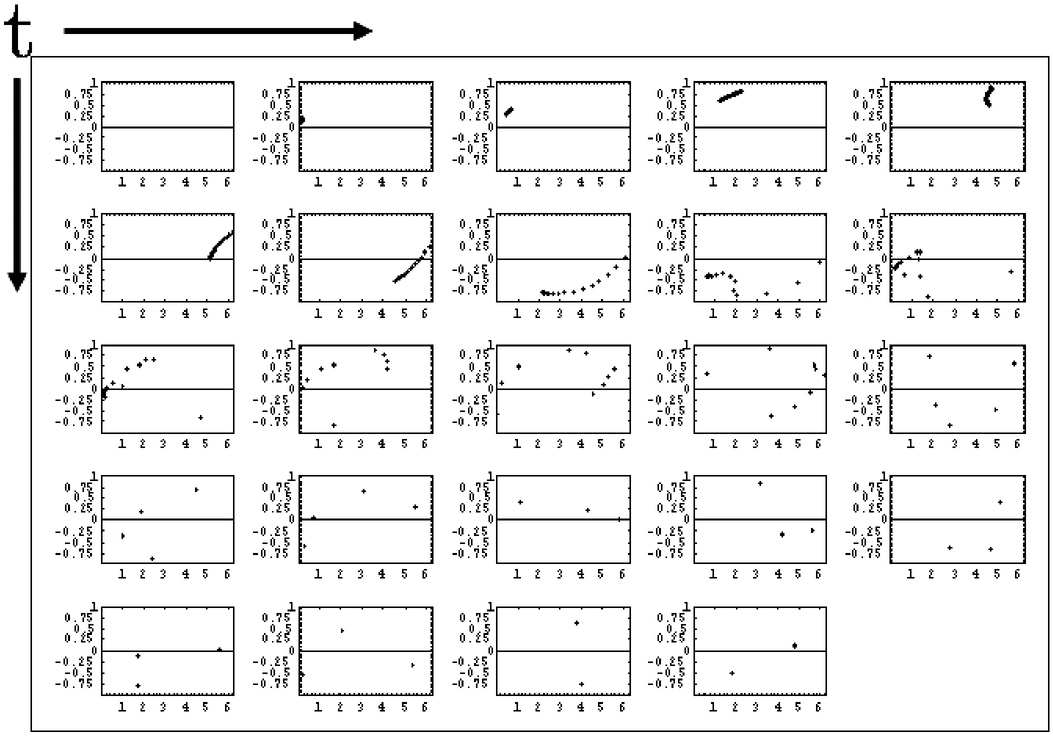

Figure 5.3: A set of initial condition closed to the unstable manifolds evolutes in time. A segment is repelled from the saddle following the unstable manifolds. Approaching the other saddle points, some of them escape from the cavity, but others are attracted by the saddle points following the stable manifolds.

mined by the horseshoe development parameter, β, as

$$T = \tau_{SOS}(-2\log_3\beta + 3/2) \tag{5.2}$$

where β is the ternary horseshoe development parameter and τ_{SOS} is the mean return time of the Poincare surface of section *i.e.* the mean time which a trajectory spends between successive hits on the bottom of the cavity. In the case of the ripple cavity, τ_{SOS} is approximately equal to $2\Delta/v$, where $\Delta = d + a$ is the largest width of the ripple cavity and v the velocity of the particle. Thus, T and τ_{SOS} depend on incident energy of the particle. With parameters of the ripple cavity given in Fig. 5.1, Fig. 5.2 shows that $\beta = 3^{-3}$, and $T/\tau_{SOS} = 7.5 \pm 0.5$ is the number of steps of the map to complete one period of rotation. The quantity T/τ_{SOS} is independent of the incident energy. We will compare this to the period of the scattering echoes in the quantum scattering problem.

5.2 Conductance fluctuations and resonances

The ripple cavity with two leads attached has been used to study various aspects of the quantum-classical correspondence in numerical simulations and microwave experiments [10, 13, 14, 37, 43]. In order to compute the conductance, we first construct the S-matrix using the reaction matrix (R-matrix) approach described in Chapter 2. Using a simple coordinate transformation [31] and zero- slope boundary conditions at the interface between the cavity and the leads [15], we construct the Hamiltonian matrix for the cavity.

(See the Section 4.2 and Appendix C) We then can calculate the eigenenergies E_i and eigenfunctions(basis wavefunctions) $\psi_i(x,y)$ of the cavity Hamiltonian and use them to construct the R-matrix

$$\mathbf{R} = \left(\begin{array}{c} R_{ll} R_{lr} \\ R_{rl} R_{rr} \end{array} \right)$$

where

$$R_{\alpha\beta}(n,n') = \frac{\hbar^2}{2m^*} \sum_{j=1}^{\infty} \frac{\phi_{j,n}(x_\alpha)\phi^*_{j,n'}(x_\beta)}{E - E_j}, \tag{5.3}$$

$r(l)$ refers to the right (left) lead, $\alpha = (r,l)$ and $\beta = (r,l)$, $\phi_{j,n}(x_\alpha)$ is the overlap between the cavity eigenfunction $\psi_j(x,y)$ and the wavefunction for the nth channel in lead α at the interface $x_l = 0$ or $x_r = W$. We neglect the evanescent modes in the leads because they do not give important contributions to the S-matrix in the regime under consideration [13]. If the energy is such that n_p modes can propagate in the lead, then the submatrix $R_{\alpha\beta}$ becomes an $n_p \times n_p$ matrix. The S-matrix is then given by

$$\mathbf{S} \ = \ U^\dagger \frac{\mathbf{1_p} - i\mathbf{Z}}{\mathbf{1_p} + i\mathbf{Z}} U^\dagger, \tag{5.4}$$

where $\mathbf{Z} = \overline{K}_p \mathbf{R} \overline{K}_p$, and $\mathbf{1_p}$ is the $2n_p \times 2n_p$ unit matrix. (See Section 2.4)

The electron conductance G in the waveguide is given by the Landauer's formula and can be expressed in terms of the transmission probability amplitudes. To be specific, we consider a waveguide formed from the semiconductor heterostructure GaAs/AlGaAs. Therefore we use the effective electron mass $m^* = 0.067m_e$ of GaAs in the calculation. The first propagating mode opens at the incident energy $E_1 = \frac{\hbar^2\pi^2}{2m^*L^2} = 0.503\,\mathrm{eV}$ for the parameters given in Fig. 5.1.

In subsequent sections, it will prove useful to construct a quantum version of the Poincare surface of section. We accomplish this by computing Husimi functions for the scattering eigenstates inside the cavity. As described in Section 4.3, the Husimi function is defined

$$H(x_0, p_0) = |\langle S(x)|x_0, p_0\rangle|^2 \tag{5.5}$$

where $S(x) = \frac{\partial\Psi_E(x,y)}{\partial y}|_{y=0}$ is the normal derivative of the scattering eigenfunction $\Psi_E(x,y)$ at $y = 0$, and the state $|x_0, p_0\rangle$ is a coherent state which has its center at p_0 and x_0 and is given by

$$\langle x|x_0, p_0\rangle = \left(\frac{\sigma}{\pi\hbar}\right)^{\frac{1}{4}} e^{\left(-\frac{\sigma}{2\hbar}(x-x_0)^2+i\frac{p_0}{\hbar}(x-x_0)\right)}. \tag{5.6}$$

The coherent state is a minimum uncertainty state and σ is chosen by requiring symmetric coarse graining [28, 49]. For simplicity, we only consider trajectories incoming from the left lead and we assume that only the 3rd propagating mode is occupied in the incident state.

Fig. 5.4 shows the conductance fluctuations for the waveguide in Fig. 5.1. The triangles represent the eigen energies of the corresponding closed ripple billiard. In the range of energy considered, three propagating modes are available ($n_p = 3$) so the system is fairly far into the quantum regime. Resonances occur in the presence of a nearly constant background continuum (*i.e.*full transmission). The resonance profiles have a Fano shape [50] whose form is given

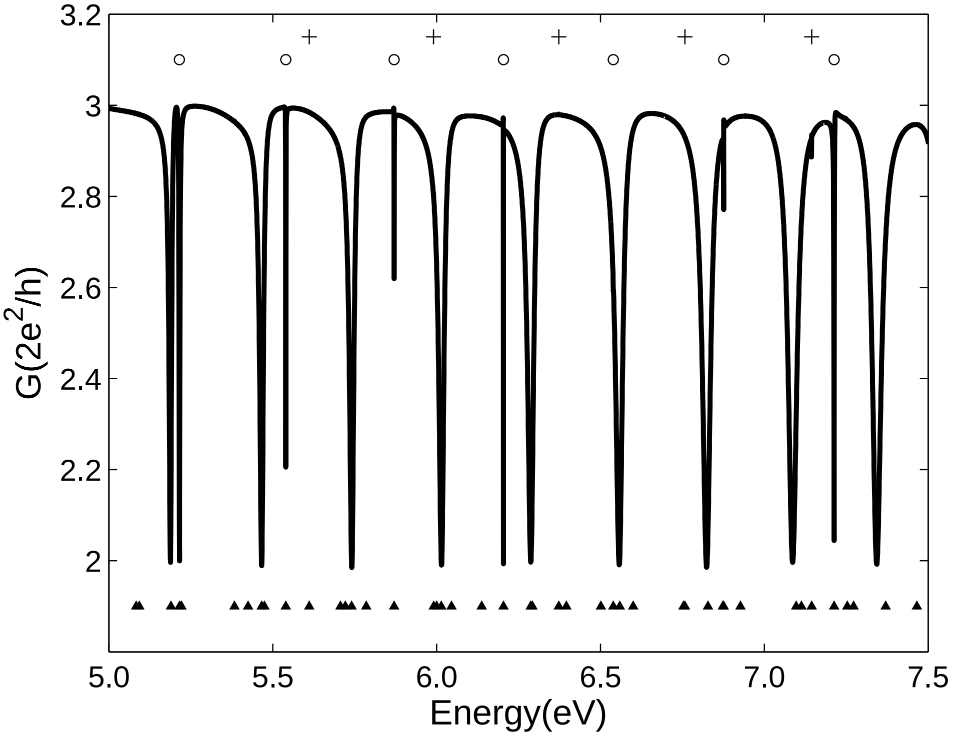

Figure 5.4: Conductance G of the waveguide with ripple cavity for the energy range where there are three propagating modes in the leads. No evanescent modes in the leads are included. The scattered triangles represent the eigenenergies of the corresponding closed billiard. The symbols "+" locate the resonances associated with the large KAM island. The symbols "o" locate the resonances associated with the period-6 island chain.

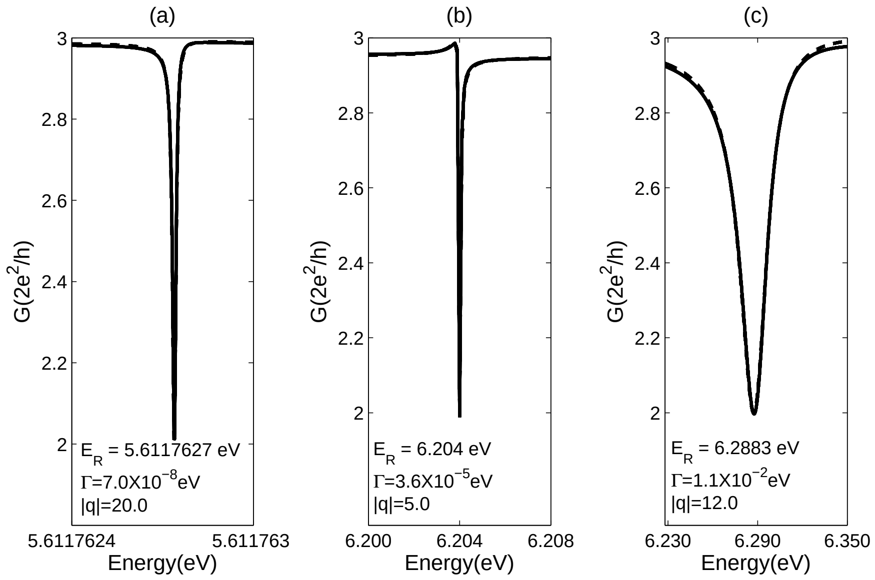

Figure 5.5: Fano shape resonances at (a) $E = 5.612$eV (a scattering state on the large KAM island). (b) $E = 6.204$eV (a scattering state on the island chain surrounding the large KAM island), (c) $E = 6.288$eV (a scattering state on the chaotic layer) Dashed lines show fitted results. The fitted parameters, E_R, Γ, and q are given.

by

$$G = G_b - G_0 \frac{(\epsilon + q)^2}{\epsilon^2 + 1}, \tag{5.7}$$

where G_b is the background conductance, G_0 determines the magnitude of the resonance, $\epsilon = (E - E_R)/\Gamma$, E_R locates the center of the resonance, Γ is the width of the resonance, and q is an asymmetry parameter.

Three types of scattering resonance contribute to the conductance fluctuations. Examples of these three types of resonance, together with their fitted parameters, E_R, Γ, and q are shown in Fig. 5.5. The resonance in Fig. 5.5(a) is located at $E = 5.612$eV and results from a scattering state that has tunneled deep into the large KAM island. The Husimi plot for the scattering state associated with this resonance is shown in Fig. 5.6(a). The resonance in Fig. 5.5(b) is located at energy $E = 6.204$eV and results from a scattering state that lies on the chain of six islands surrounding the large KAM island. The Husimi plot of the scattering state which causes this resonance is shown in Fig. 5.6(b). The broad resonance in Fig. 5.6 is located at energy $E = 6.288$eV and results from a scattering state lying on the chaotic scattering layer. This is clearly seen from the Husimi plot of this scattering state shown in Fig. 5.6(c). The resonance due to the state on the chaotic layer is three orders of magnitude broader than the resonance due to the state on the chain of islands. States on the chaotic layer have a significant amplitude at the interface and are fairly strongly coupled to the continuum. This is why their resonances are so broad.

The three types of resonances shown in Figs. 5.5 and 5.6 are members of three distinct families of resonances whose members appear in the conductance with a characteristic period in energy. The family of resonances which are associated with scattering states sitting on the large KAM island are too narrow to be seen in Fig. 5.4. Their positions are marked by the symbol "+". They occur in Fig. 5.4 with period $T_E \approx 0.385$eV. The family of resonances associated with scattering states sitting on the island chain surrounding the large KAM island are broader and some can be seen in Fig. 5.4. These resonances are marked with the symbol "o" and have period $T_E \approx 0.335$eV. The

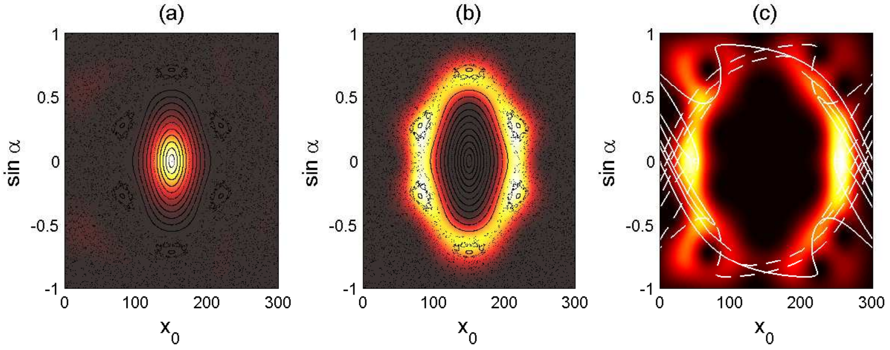

Figure 5.6: Husimi plots of resonant scattering states for the resonances in Fig. 5.5. (a) The state at $E = 5.612$eV lies on the large KAM island. (b) The state at $E = 6.204$eV lies on the island chain surrounding the large KAM island. (c) The state at $E = 6.288$eV lies on the chaotic scattering layer and has high probability regions closed to the outer fixed points. Husimi plots (a) and (b) are superimposed on the classical Poincare surface of section, and (c) on the stable and unstable manifolds.

family of resonances associated with scattering states sitting on the chaotic layer are very broad and can all be seen in Fig. 5.4. These broad resonances also appear periodically in energy. We will show they give rise to the echoes in the transmitted probability.

In order to determine the period of the scattering echoes for the quantum system, we perform a FFT (Fast Fourier Transformation) of the conductance fluctuations. The FFT of the conductance fluctuations in Fig. 5.4 picks up the broad resonances since the narrow resonances barely give a contribution to the FFT and is shown in Fig. 5.7. Before the FFT is performed, we remove the monotonic background. Fig. 5.7 shows beautiful simple harmonics with fundamental frequency $f_E = 1/\Delta E_0 = 3.66\ (eV)^{-1}$. With this frequency, we

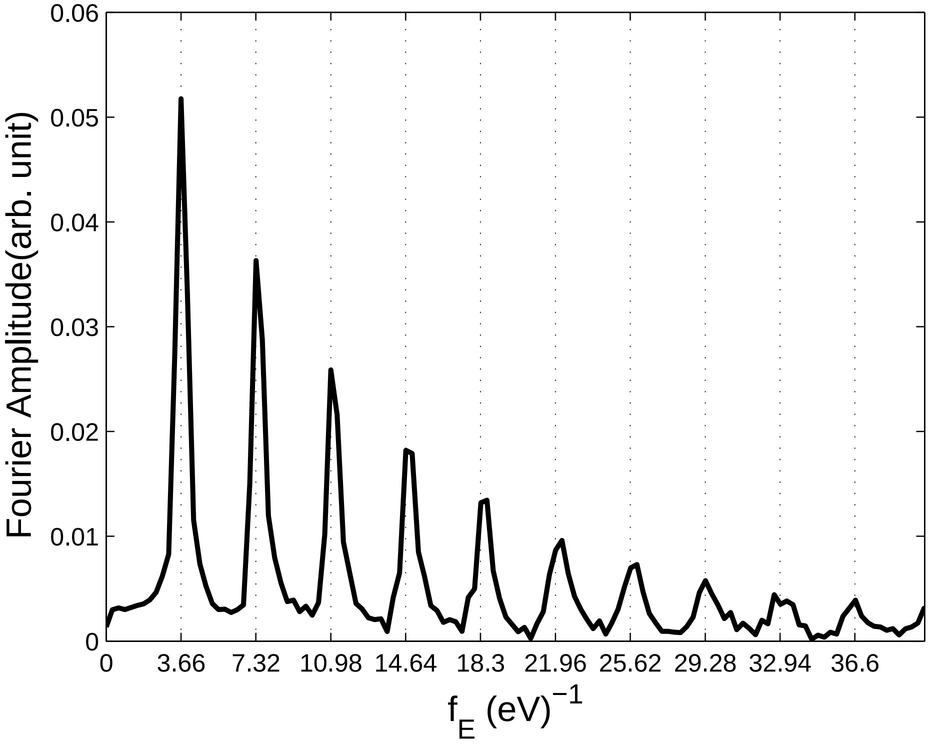

Figure 5.7: The FFT of Fig. 5.4. To perform the FFT, we remove the monotonic background. The plot yields a fundamental frequency $f_E = 1/\Delta E_0 = 3.81(eV)^{-1}$.

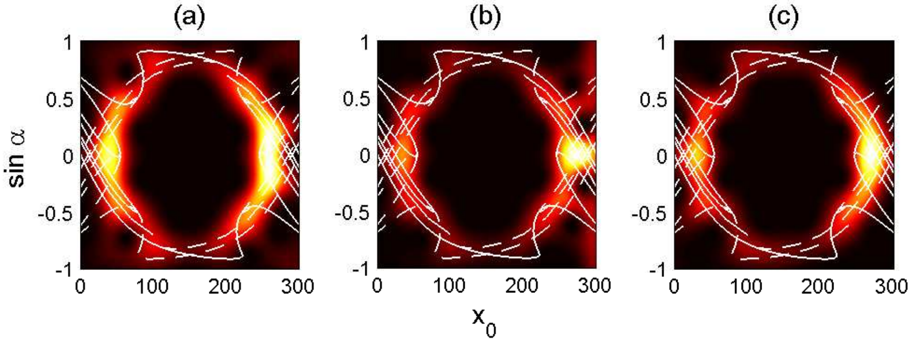

Figure 5.8: Husimi Plots for resonant scattering states on the chaotic layer for (a) $E = 6.557\text{eV}$, (b) 6.824eV, and $E = 7.086\text{eV}$. These states all cover the chaotic scattering layer.

can compute the period of the scattering echoes using $T_c = 2\pi\hbar/\Delta E_0$. We obtain $T_c/\tau_{SOS} = 6.85$. This is close to our classical result of $T/\tau_{SOS} = 7.5 \pm 0.5$. The lower value than the classical result coming from the FFT estimate can be explained in terms of tunneling of part of the resonant state into the large KAM island. We will discuss this in more detail later.

5.3 Quantum Echoes

Fig. 5.8 shows Husimi plots of resonant scattering eigenstates located at energies $E = 6.557\text{eV}$, $E = 6.824\text{eV}$, and $E = 7.086\text{eV}$. These states lie on the chaotic layer as can be seen from classical homoclinic/heteroclinic tangles superposed on the plot. The eigenstates have maximum probability sitting near the outer fixed points. Near the outer fixed points the classical velocity is small so the quantum probability is large. As the incident energy increases, the resonant eigenstates lie further out in the region of tangles and

Table 5.1: The energy frequency $f_E = 1/\Delta E_0$ and T_c/τ_{SOS} for $n_p = 3, 4, 5, 6$. The horseshoe development parameter β is 3^{-3}

n_p	$f_E(eV)^{-1}$	T_n/τ_{SOS}
3	3.81	7.80
4	2.98	7.47
5	2.46	7.51
6	2.09	7.26

cover the chaotic scattering layer. The higher energy states have very little overlap with the central KAM island. If we pick the last two resonances in Fig. 5.4 [47], and use the separation between the last two resonances as ΔE_0, then we obtain $T_c/\tau_{SOS} = 7.80$ for the echo period. This agrees well with the classical prediction 7.5 ± 0.5. We can now understand why the echo period obtained from the FFT is shorter than the theoretical prediction. The rotation period of trajectories inside the KAM island decreases as we go deeper into the island. This decreases the effective echo period for scattering states on the chaotic layer which partially tunnel into the large KAM island. The states with lower energy have larger overlap with the large KAM island.

We can also find the frequency $f_E = 1/\Delta E_0$ for energy regimes with more than three propagating modes. Table 5.1 shows numerical results for T_c/τ_{SOS} for $n_p = 3, 4, 5, 6$. All of them agree with the theoretical expectation.

We can change the horseshoe development parameter of the classical system by changing the amplitude a of the ripple cavity. As the parameter a is decreased, the amount of chaos in the system decreases and the horseshoe development parameter increases (see Fig. 5.9 in Ref. [47]). We have calculated

Table 5.2: The energy frequency $f_E = 1/\Delta E_0$ and T_c/τ_{SOS} for different development of horseshoe

β	$f_E(eV)^{-1}$	$-2\log_3\beta + 3/2$	T_c/τ_{SOS}
3^{-3}	3.81	7.5 ± 0.5	7.80
3^{-4}	3.28	9.5 ± 0.5	9.35
3^{-5}	3.71	11.5 ± 0.5	11.94
3^{-6}	3.35	13.5 ± 0.5	13.98

the period of the scattering echoes for systems which have a smaller horseshoe development parameter ($-2\log_3\beta > 6$). The results are shown in Table 5.2. For a smaller horseshoe development stage $\beta = 3^{-4}$ and 3^{-5}, we used the energy regime with four propagating modes (*i.e.* $n_p = 4$). For horseshoe development stage $\beta = 3^{-6}$, we used five propagating modes ($n_p = 5$) because, in that case, higher energy is needed to resolve the finer structure of the tangles.

Let us next consider the two families of resonances exemplified by Figs. 5.5(a) and 5.5(b) and Figs. 5.6(a) and 5.6(b). The resonances associated with the large KAM island occur periodically in energy. Using the energy spacing $\Delta E_0 = 0.3867$eV for these resonances, we obtain a period of $T_c/\tau_{SOS} = 5.29$ which means the rotation inside the KAM island is faster than that of the chaotic region. The resonances associated with the island chain also appear periodically in energy with different period than the very narrow resonances or the broad resonances. Let us pick up the two sharp resonances (at $E = 6.5394$eV and $E = 6.8762$eV) in Fig. 5.4, and use the energy separation as ΔE_0. We then obtain $T_c/\tau_{SOS} = 6.12$ which is close to the period of the period-6 island chain.

5.4 The wavepacket dynamics

In order to show scattering echoes in real time, in this section we study the time evolution of a wavepacket in the waveguide. First, we prepare a wavepacket which propagates to the right and enters the ripple cavity on the left. We choose a wavepacket which has a Gaussian form along the x-direction and lies fully in the third transverse channel. The initial wavepacket is given by

$$\Psi(x, y, t=0) \;=\; \frac{1}{(g\sqrt{2\pi})^{1/2}} e^{-(x-x_0)^2/4g^2} e^{ik_0 x} \chi_3(y), \tag{5.8}$$

where $\chi_3(y) = \sqrt{\frac{2}{L}} \sin\left(\frac{3\pi}{L}y\right)$ and g determines the width of the wavepacket. Initially the wavepacket is centered at $x = x_0$ and propagates to the right with wavevector k_0. We can expand the initial wavepacket in terms of the energy eigenfunctions (in this case scattering wavefunctions $\varphi_E(x, y)$) so that

$$\Psi(x, y, t=0) \;=\; \frac{1}{\sqrt{2\pi}} \int_0^\infty b_3(E) \varphi_E(x, y) dE. \tag{5.9}$$

Then, the time evolution of the wavepacket is simply given by

$$\Psi(x, y, t) \;=\; \frac{1}{\sqrt{2\pi}} \int_0^\infty b_3(E) e^{-i\frac{E}{\hbar}t} \varphi_E(x, y) dE. \tag{5.10}$$

If we measure the amplitude of the wavepacket at a certain point (x', y') in the asymptotic region in the right lead, the time evolution of wavepacket can be written in terms of transmission probability amplitudes, $t_{nn'}$, such that

$$\Psi(x', y', t) \;=\; \frac{1}{\sqrt{2\pi}} \int_0^\infty b_3(E) \sum_{n'} \frac{t_{3n'}}{\sqrt{k_{n'}}} e^{ik_{n'}(x'-x_0) - i\frac{E}{\hbar}t} dE \chi_{n'}(y') \tag{5.11}$$

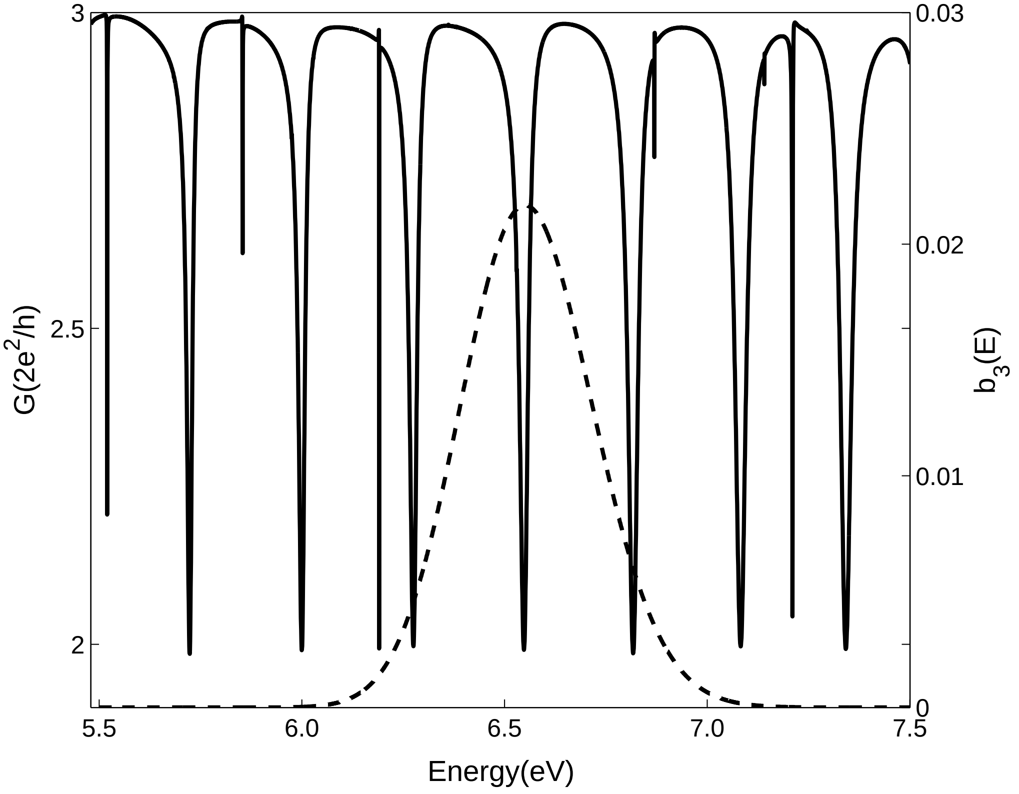

Figure 5.9: The probability amplitude function $b_3(E)$ (dashed line) of the eigenfunction expansion for an initial wavepacket with $g = 66.487\text{Å}$, $x_0 = -1000\text{Å}$, and $k_0 = 0.1889\text{Å}^{-1}$ superposed on the conductance fluctuations for the corresponding energy regime.

where $k_{n'}$ is defined in Section 2.4. We will study the time evolution of this wavepacket for the parameters given in Fig. 5.1 so the horseshoe development parameter of the system is $\beta = 3^{-3}$. We prepare an initial wavepacket with $g = 66.487\text{Å}$, $x_0 = -1000\text{Å}$ and $k_0 = 0.1889\text{Å}^{-1}$. We then calculate $b_3(E)$ from Eq.(5.9). Fig. 5.9 shows $b_3(E)$ superimposed on the conductance fluctuations (also shown in Fig. 5.4). The $b_3(E)$ is centered on the resonance at $E = 6.557\,\text{eV}$ and overlaps three neighboring resonances. There are three transmission routes for the incident wavepacket ($n = 3 \rightarrow n' = 1$, $n = 3 \rightarrow n' = 2$, and $n = 3 \rightarrow n' = 3$) since three propagating modes are also available in the right lead. However, we here consider only the transmission route $n = 3 \rightarrow n' = 3$. Fig. 5.10 shows the probability $\overline{P}(x', y', t) = |\Psi(x', y', t)|^2$ coming from the incident wavepacket after it has been transmitted through the ripple cavity and passes the point x', y' in the right lead for $x' = 1000\text{Å}$ and $y' = L/2$. Fig. 5.10 clearly shows the time-periodic scattering echoes. The period of echoes in Fig. 5.10 is $T_w = 15.5\,\text{fs}$, so that $T_w/\tau_{sos} = 7.453$ which is consistent with the theoretical expectation 7.5 ± 0.5 and the result from the conductance fluctuations in Section 5.3. The inset of Fig. 5.10 is linear-log plot of $P(x', y', t)$ (at $x' = 1000\text{Å}$ and $y' = L/2$) which more clearly shows the time periodic behavior and shows exponential decay of the probability instead of power law decay as discussed in Ref. [47]. Exponential decay implies that tunneling has occurred into the classically inaccessible KAM island. This exponential decay indicates that the hierarchy states do not play a significant role in the quantum dynamics at the energies considered here. If the energy

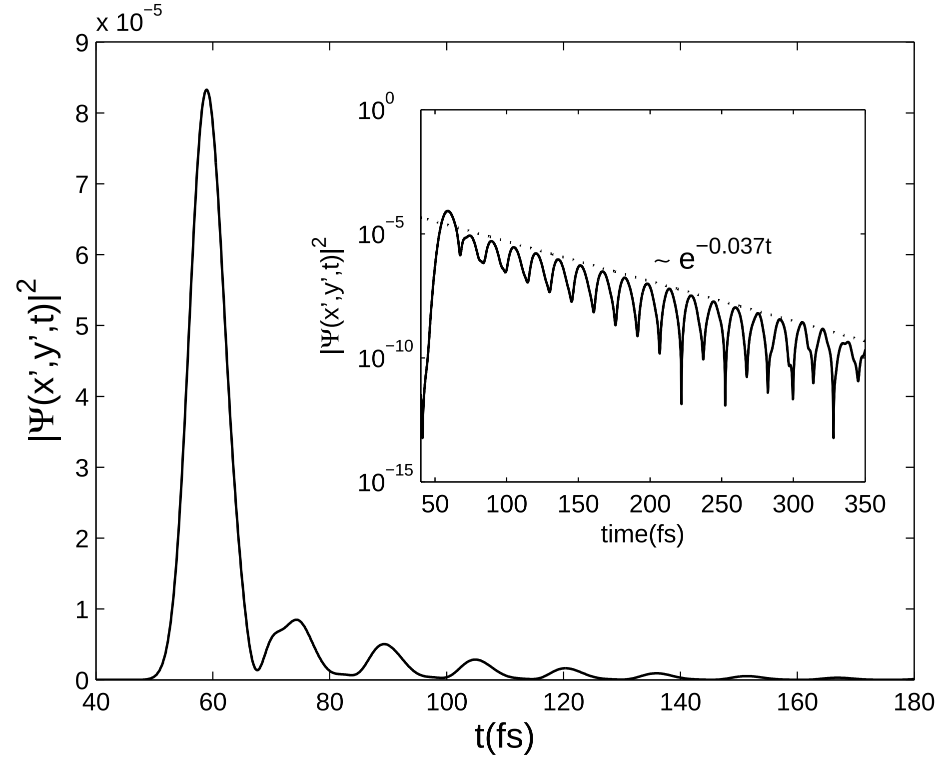

Figure 5.10: The transmitted wavepacket $|\Psi(x', y', t)|^2$ in the asymptotic region of the right lead ($x' = 1000\mathring{A}, y' = L/2$) as a function of time. The inset is a linear-log plot of the probability which appears to decay exponentially.

would be high enough, we expect that it shows the power law decay which implies that the fractal structure exists.

Chapter 6

Dicke Effect in a multi ripple waveguide

Electron matter wave transmission through waveguides has been studied for years, both numerically and experimentally [51, 52, 53, 13]. Electron waveguides can be constructed in the two dimensional electron gas (2DEG) which is formed in semiconductor heterostructures. Confinement along the transversal direction can be obtained by gates that deplete electrons from regions of the 2DEG. Due to this confinement, the wavefunction along the transversal direction is discretized and the conductance through the waveguide is quantized. This quasi one dimensional behavior of electrons makes it easy to study ballistic electron scattering effects.

Research on quantum dots has also grown rapidly in recent years. Electron confinement in quantum dots results in the discrete energy levels of electrons so they are often called "artificial atoms." Electron transmission has been studied in waveguides that contain impurities [15] or waveguides that attach to a cavity or a quantum dot [16, 53]. Quasi bound states are formed near impurities or in quantum dots which are attached to waveguides. Quasi bound states induce resonances that can significantly affect the electron transmission. These resonance structures carry not only the quantum coherent interference effects, but also the classical scattering information such as, for example, self-pulsing effects in a mono-ripple cavity [16] and fractal conductance fluctuations [54].

In quantum optics, Dicke found a type of spontaneous radiation which has much larger wavelength than the separation distance between two atoms [55]. The radiation takes place in a transition from a collective exited state that is strongly coupled to the photon field while the another collective state is weakly coupled to the photon field and has a long lifetime. The coupling of the atoms through the same photon fields result in those collective states. The radiation from the short lived state is called *superradiance* and the radiation from the long lived state is called *subradiance*. The Dicke effect in a mesoscopic system was first found in two channel resonant tunneling by Shahbazyan and Raikh [56]. In this system, the bound state of each impurity is indirectly coupled through common leads. Analogies to the Dicke effect have been found in several mesoscopic systems, such as quantum dots coupled via a common phonon field [57], and a quantum wire with side coupled quantum dots [58]. In this paper, we find a Dicke effect in the conductance of a multi-ripple electron waveguide.

The ripple billiard and waveguide have proven very useful for the study of the quantum-classical correspondence, when chaos is present, because it is easy to adjust the amount of chaos in the ripple billiard and it is possible to construct an analytic expression for the Hamiltonian of the billiard. In this paper, we consider the dynamics of a multi-ripple electron waveguide which consists of waveguide with a cavity containing one flat wall and an another wall in the shape of several oscillations of a cosine. Each oscillation of the cosine wall creates a trapping region so that the system is very similar to that of several coupled quantum dots. If the ends of the cavity are closed off to form a multi-ripple billiard, the discrete energy eigenstates of the billiard form symmetric and antisymmetric pairs. In the case when the billiard is opened and coupled to leads to form a multi-ripple waveguide, the scattering states of the multi-ripple waveguide also form symmetric and anti-symmetric pairs. We find that the anti-symmetric states are more weakly coupled to the continuum states of the waveguide than are the symmetric states. This is the source of the Dicke effect.

We use reaction matrix (R-matrix) theory to compute the electron transmission probability and electron scattering wavefunctions in the multi-ripple waveguide. The R-matrix theory was originally developed by Wigner and Eisenbud in 1950s for the study of nuclear scattering. R-matrix theory more recently has been used to study ballistic electron transmission in waveguides [13, 14, 16].

This chapter is organized as follows. In Section 6.1, we describe the bi-ripple waveguide system and we review scattering theory and conductance in quantum waveguides using the R-matrix theory and the Landauer Formula. In Section 6.2, we present the numerical results for electron transmission through the bi-ripple waveguide. We show that the resonance splitting in the electron transmission is analogous to the Dicke effect in Section 6.3. We study a multi-ripple waveguide (more than two ripples) in Section 6.4. We show that the width of a resonance state linearly increases with the number of ripples N, a behavior that is analogous to the N-atom Dicke model result.

6.1 The bi-ripple waveguide

In Chapter 5, we showed that the conductance of a mono-ripple waveguide has rich structure due to the various types of quasi bound states, and the conduction resonances that result from them, that can be formed in the waveguide. The quasibound states in the mono-ripple waveguide are the analog of excited states of an atom in the Dicke model, and the electron matter waves in the waveguide are the analog of the radiation field in the Dicke model. The quasi-bound states and conduction resonances in the mono-ripple waveguide were found to have several different origins based on the corresponding classical dynamics of an electron in the ripple cavity of the waveguide. We found three families of resonances, one due to the KAM island, a second due to the island chain surrounding the KAM island, and a third due to heteroclinic tangles that form the partial transport barrier at the opening of the ripple cavity.

We now consider the conductance of a bi-ripple electron waveguide. Fig. 6.1 shows a schematic view of this system and also shows the corresponding classical phase space (Poincare surface of section). We use Birkhoff coordinates $(x_0, \sin\theta)$, where x_0 is the x-coordinate and θ is the reflection angle when the electron hits the bottom boundary. The shape of the upper wall of

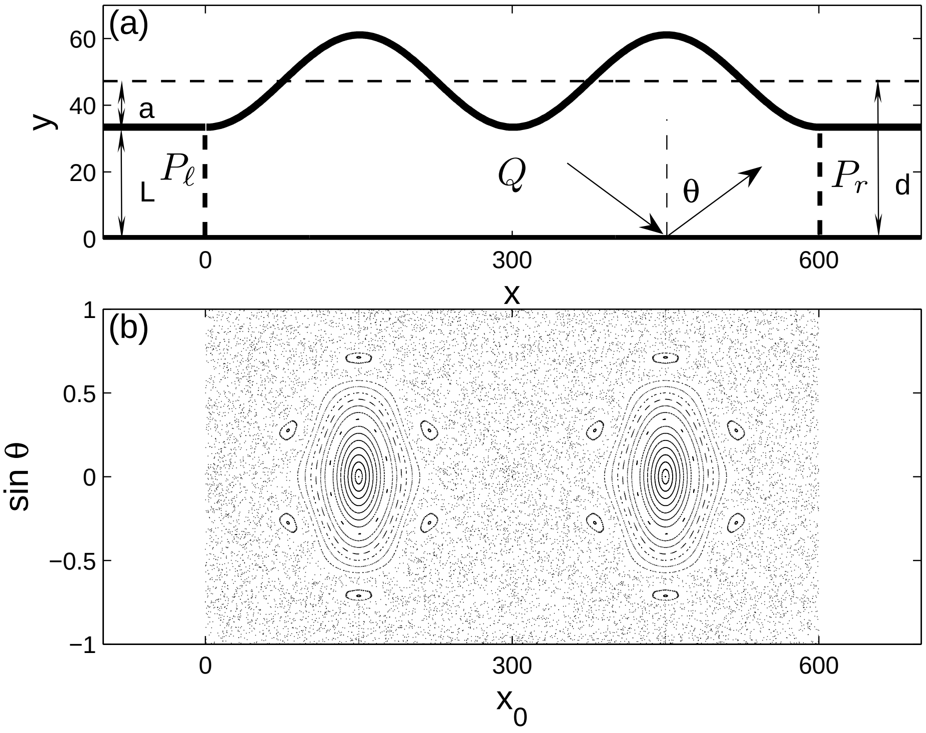

Figure 6.1: (a) The schematic view of the bi-ripple waveguide, where $a = 13.846\mathring{A}$ and $d = 47.269$. θ is the reflection angle at the bottom wall. (b) The classical Poincare surface of section using Birkhoff coordinate at the bottom boundary. The parameter a and d are chosen to have mixed phase space.

the ripple cavity is given by the expression

$$y(x) = d - a\cos\left(\frac{4\pi x}{W}\right), \tag{6.1}$$

where $L = d - a$ is the height of the quantum waveguide leads that attach to either side of the bi-ripple cavity. The height of the waveguide leads determines the energy E_1 at which the first propagating mode can appear, namely $E_1 = \frac{\hbar^2\pi^2}{2m^*L^2}$. The parameters a and d also determine the classical dynamics of the system. In this analysis, we use the effective mass of an electron in GaAs, $m^* = 0.067\,m_e$ where m_e is the electron mass in free space. Fig. 6.1 (b) shows a Poincare surface of section for the bi-ripple cavity with the parameters $a = 13.846\mathring{A}$, $d = 47.269\mathring{A}$ and $W = 600\mathring{A}$. We choose these parameter values because we want the system to have a mixed phase space. For these parameters $E_1 = 0.5034074$ eV.

For the parameters used in the Fig. 6.1, there are five primary fixed points: two stable fixed points are located in the peak of each ripple, two fixed points of mixed stability are at the left and right boundaries of the bi-ripple cavity, and one unstable fixed point is at the center of the bi-ripple cavity. The first two fixed points are associated with the center KAM islands and the other three are related with the heteroclinic tangles and chaos in the classical phase space. As we have shown in Chapter 5, we can identify the way in which resonances are related to classical dynamical structures by using Husimi plots [28].

We compute S-matrix and a scattering wavefunction to solve a Schrodinger equation using R-matrix theory described in Chapter 2. In order to apply the R-matrix theory to the bi-ripple waveguide, we divide the configuration space of the waveguide into three areas as shown in Fig. 6.1 (a). The bi-ripple cavity itself is called the reaction region, Q, and the two asymptotic regions P_ℓ and P_r are electron waveguides attached to the left and right sides of the bi-ripple cavity, respectively. The essence of the R-matrix theory is that we can expand the scattering wavefunction in the reaction region in terms of a set of basis functions which satisfy certain boundary conditions at the interfaces. For simplicity, we use Neumann (zero slope) boundary conditions for the interfaces between the bi-ripple cavity and the waveguide leads. The basis states only need to be computed once. The the S-matrix can be calculated easily for a wide range of energies.

We will assume that the upper and bottom walls of the waveguide are infinitely hard and we use zero-slope boundary conditions at the interfaces between the reaction region and the asymptotic regions. Then we can introduce a discrete set of basis states ψ_j for the reaction region which satisfy the eigenvalue equation

$$\hat{H}_{QQ}\psi_j = E_j\psi_j, \tag{6.2}$$

where E_j is the eigenvalue associated with the jth eigenstate ψ_j. We can expand the scattering eigenfunction $\Psi(x, y; E)$ (for an electron incident with energy E) in terms of the basis functions $\psi_j(x, y)$ in the reaction region

$$\hat{Q}\Psi(x, y) = \sum_{j=1}^{\infty} \gamma_j \psi_j(x, y), \tag{6.3}$$

where γ_j is a jth expansion coefficient.

With the help of the simple coordinate transformation used in Section. 4.2, we can construct the Hamiltonian matrix for the cavity. To get convergent eigenvalues for the energy regime under consideration here, we use 30 basis states for the y-direction and 400 basis states for the x-direction. Therefore, we have a 12 000 × 12 000 Hamiltonian matrix. We can diagonalize it with reasonable computation time (less than 1hr) by using 16-processors and ScaLAPACK routine. As a result, we can calculate the eigenenergies E_j and eigenfunctions $\psi_j(x,y)$.

If the incident energy is larger than $E_1 = \hbar^2/2m^*(\pi/L)^2$, there are propagating modes as well as evanescent modes in the asymptotic region. However, for simplicity, we neglect the evanescent modes because they are not important for energies under consideration here [13].

Using formalism in Section 2.4, $R_{\alpha\beta}(n,n')$,the matrix elements of the R-matrix, are obtained,

$$R_{\alpha\beta}(n,n') = \frac{\hbar^2}{2m^*}\sum_{j=1}^{\nu}\frac{\phi_{j,n}(x_\alpha)\phi_{j,n'}(x_\beta)}{E-E_j}, \tag{6.4}$$

and ν denotes the number of basis states used to compute the R-matrix. (Ideally $\nu = \infty$, but in practice ν is some large value determined by the number of basis states needed to give convergent results. In our case $\nu = 12,000$.) The R-matrix is a $2n_p \times 2n_p$ dimensional matrix (assuming n_p propagating modes in each lead) and can be written in the form

$$\mathbf{R} = \begin{pmatrix} R_{\ell\ell} & R_{\ell r} \\ R_{r\ell} & R_{rr}. \end{pmatrix} \tag{6.5}$$

The R-matrix is usually well defined except at R-matrix poles such as $E = E_j$. Therefore, we use the regularization method developed by Mil'nikov and Nakamura [59] to avoid divergence of S-matrix in numerical calculations.

From Eq.(2.67), we write the relation between incident electron waves, with energy E, and outgoing electron waves

$$\begin{pmatrix} \bar{b} \\ \bar{d} \end{pmatrix} = \mathbf{S}(E) \begin{pmatrix} \bar{a} \\ \bar{c} \end{pmatrix}, \tag{6.6}$$

where $\mathbf{S}(E)$ is the scattering matrix. After some rearrangement [1], $\mathbf{S}(E)$ can be written in the form

$$\mathbf{S}(E) = U^{\dagger}\cdot \left(\mathbf{1_p} - 2i\mathbf{w}^T \cdot \frac{1}{E\mathbf{1}_{in} - \mathbf{H}_{in} + i\mathbf{w}\cdot\mathbf{w}^T} \cdot \mathbf{w} \right) \cdot U^{\dagger} \equiv \begin{pmatrix} \bar{r} & \bar{t}' \\ \bar{t} & \bar{r}' \end{pmatrix}. \tag{6.7}$$

If n_p propagating modes pass in each waveguide, $\mathbf{1_p}$ is a $2n_p \times 2n_p$ unit matrix. $U^{\dagger}$ is a $2n_p \times 2n_p$ diagonal matrix with elements $e^{-ik_n x_\ell}(n = 1, ..., n_p)$ and $e^{-ik_n x_r}(n_{p+1}, ..., 2n_p)$. If ν basis states are used to compute the R-matrix, then $\mathbf{1}_{in}$ is a $\nu \times \nu$ unit matrix and $\mathbf{H}_{in}$ is a $\nu \times \nu$ diagonal matrix whose diagonal elements, $(\mathbf{H}_{in})_{j,j} = E_j$ for $j = 1, ..., \nu$, are the basis state energies. The matrix $\mathbf{w}$ is a $\nu \times 2n_p$ dimensional matrix which gives the strength of the coupling between the ripple cavity and the waveguide leads. At the left interface ($x = x_\ell$) it's matrix elements are defined $(\mathbf{w})_{j,n} = \phi_{j,n}(x_l)\sqrt{\hbar^2 k_n/2m}$ for $j = 1, ..., \nu$ and $n = 1, ..., n_p$. At the right interface at ($x = x_r$) they are defined $(\mathbf{w})_{j,n} = \phi_{j,n}(x_r)\sqrt{\hbar^2 k_n/2m}$ for $j = 1, ..., \nu$ and $n = n_p+1, ..., 2n_p$. The matrix $\mathbf{w}^T$ is the transpose of $\mathbf{w}$. In Eq. (6.7), t and t' are transmission probability amplitudes and r and r' are reflection probability amplitudes. $\bar{t}(\bar{r})$ and $\bar{t}'(\bar{r}')$ are $n_p \times n_p$ matrices of transmission (reflection) probability amplitudes.

The form of the S-matrix given in Eq. (6.7) shows explicitly the structure of the complex energy poles of the S-matrix. Since the poles of the S-matrix are the same as the poles of the Green's function for the waveguide, the S-matrix poles also give the complex energies of the quasibound states of the ripple cavity. The matrix $\mathbf{w}$ largely determines the strength of the coupling between the reaction region (the ripple cavity) and the waveguide leads and thereby the lifetime of the quasibound states. The matrix $\mathbf{H}_{in}$ largely determines the location, along the real energy axis, of the quasibound state energies. This correspondence is not strictly exact because one must actually search for complex values of E that give zeros of the quantity $\mathrm{Det}[E\mathbf{1}_{in}-\mathbf{H}_{in}+i\mathbf{w}\cdot\mathbf{w}^T]=0$ in order to determine the complex energies $E=E_0+i\Gamma$, of quasibound states. Here E_0 is the real part of the quasibound state energy and Γ is the imaginary part. The lifetime of quasibound states is given by $\tau=\hbar/2\Gamma$.

The ballistic electron waveguide can be formed in GaAs/AlGaAs heterostructures at very low temperature. The mean free path of the electrons is so long that quantum coherent scattering of electrons off the waveguide walls plays an important role in determining the transmission probability. The conductance G in the waveguide at very low temperature is given by the Landauer formula

$$G=\frac{2e^2}{h}\sum_{i,j}^{n_p}|t_{i,j}|^2, \tag{6.8}$$

where $T=\sum_{i,j}^{n_p}|t_{i,j}|^2$ is the transmission probability.

6.2 Transmission Resonances and Husimi Plots

We have computed the transmission probability for an electron passing through the bi-ripple waveguide. Fig. 6.2 shows the transmission probability for electrons with an incident energy which lies between E_1 and $E_2 = 4E_1$, the threshold energies of the first and second propagating channels, respectively. In this energy interval, one transversal mode propagates in the waveguide leads. Resonance structures appear in a nearly periodic sequence, which is similar to what we found in the mono-ripple waveguide [16]. There are some differences in the various resonance structures, which we describe below.

6.2.1 First Resonance Structure

Fig. 6.3 (a) shows an enlargement of the lowest energy resonance in the bi-ripple waveguide (solid line), and in the mono-ripple waveguide (dashed line). In Figs. 6.3 (c) and (d) we also show the wavefunction for the two basis states of the bi-ripple cavity which are closest in energy to this resonance. These two basis states give dominant contributions to this lowest energy resonance. The energies $E_{17} = 1.327612\,E_1$ and $E_{18} = 1.327926\,E_1$ of these two states are nearly degenerate and the states form a symmetric and anti-symmetric pair with respect to the center of the double cavity. In Fig. 6.3 (a), the transmission resonance of the bi-ripple waveguide is little bit broader than that of the mono-ripple waveguide, and it appears to have just one transmission zero. Fig. 6.3 (b) shows the log contour plot of the transmission amplitude for the bi-ripple waveguide in the complex energy plane. Two

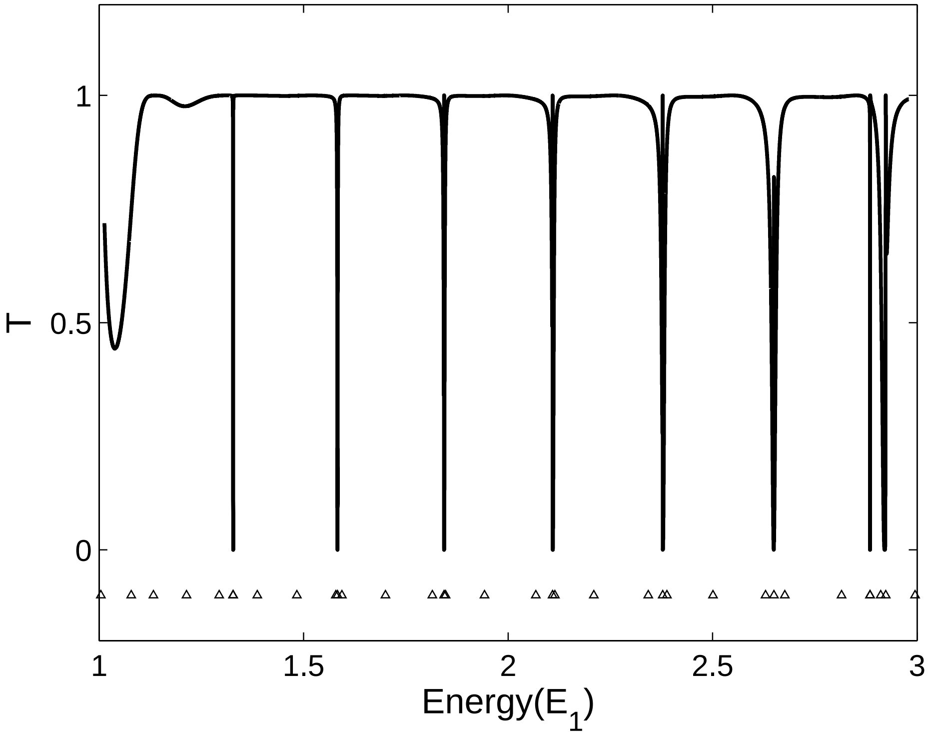

Figure 6.2: Electron transmission through the double ripple cavity for the energy range where only a propagating modes is allowed in the leads. No evanescent modes are included. The triangles represent the eigen energies (E_j in Eq. 6.2) for the corresponding bi-ripple cavity(Neumann boundary condition at the interfaces, but Dirichlet boundary condition at upper and bottom walls).

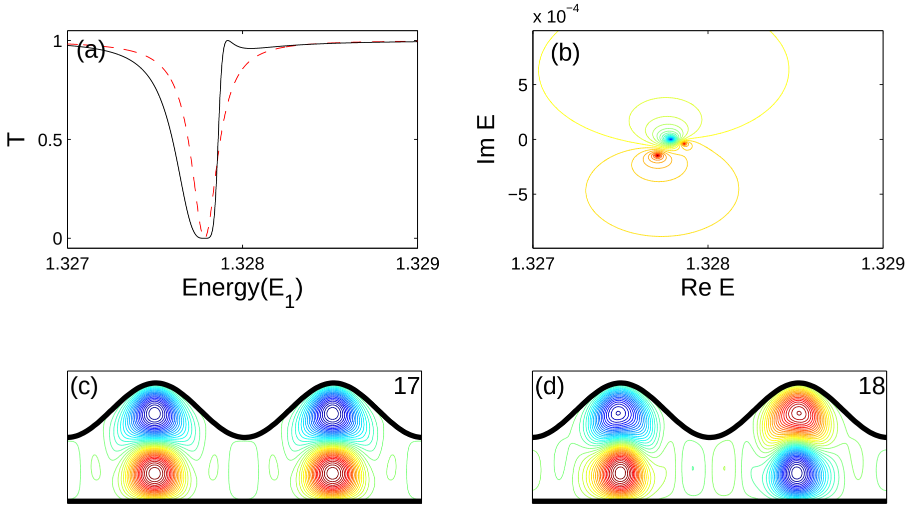

Figure 6.3: Lowest energy conductance resonance in the first channel. (a) Solid line (dashed line) represents the electron transmission for the bi-ripple (mono-ripple) waveguide. (b) Contour plot of log T in a complex energy plane. (c) Spatial distribution of ψ_{17}. Red (blue) is positive (negative). (d) Spatial distribution of ψ_{18}.

poles of the transmission amplitude (red regions) and one transmission zero (blue region on the real axis) are clearly seen in Fig. 6.3 (b).

In Fig. 6.4, we plot the transmission probability as a function of real energy and show a contour plot of the transmission amplitude in the complex energy plane using only selected R-matrix basis states, with energies near the resonance energy, for the computation. In Fig. 6.4 (a) and (a'), we include only the states ψ_{16} and ψ_{17} when we take the summation in Eq. (6.4). Fig. 6.4(a) clearly shows the Fano type resonance [53] due to the interference between non-resonant state (16th) and resonant state (17th). The transmission zero and pole pair is seen in (a'). We can see two transmission zeros and two poles in Fig. 6.4 (c) and (c') where we include the 16th through 19th basis states. After adding one more state (15th state), we find the transmission probability is getting close to the transmission probability for full calculation in Fig. 6.4 (d). Fig. 6.4 (d') shows that the two transmission zeros collide when the 15th state is included. Thus, we find that the lowest energy resonance originates from two quasibound states with very different lifetimes, but with two corresponding transmission zeros that overlap. The ratio between the lifetime τ_A (τ_S) for the quasibound state associated with the symmetric (antisymmetric) scattering state is $\tau_S/\tau_A = 3.7$. As we will discuss in the next section, this ratio for the quasibound state lifetimes for the first resonance structure is much smaller than the ratio of lifetimes for the second resonance structure.

6.2.2 Second Resonance Structure

Fig. 6.5 (a) shows a magnification of the second (in Fig. 6.3) transmission resonance in the bi-ripple waveguide (solid line) and the mono-ripple waveguide (dashed line). For the bi-ripple waveguide, we can see two resonances, one which has much broader width than the resonance for mono-ripple waveguide, and another which is much narrower. These two resonances correspond to symmetric and anti-symmetric resonant states. Fig. 6.5 (b) shows the contour plot of log T in the complex energy plane. This plot contains a

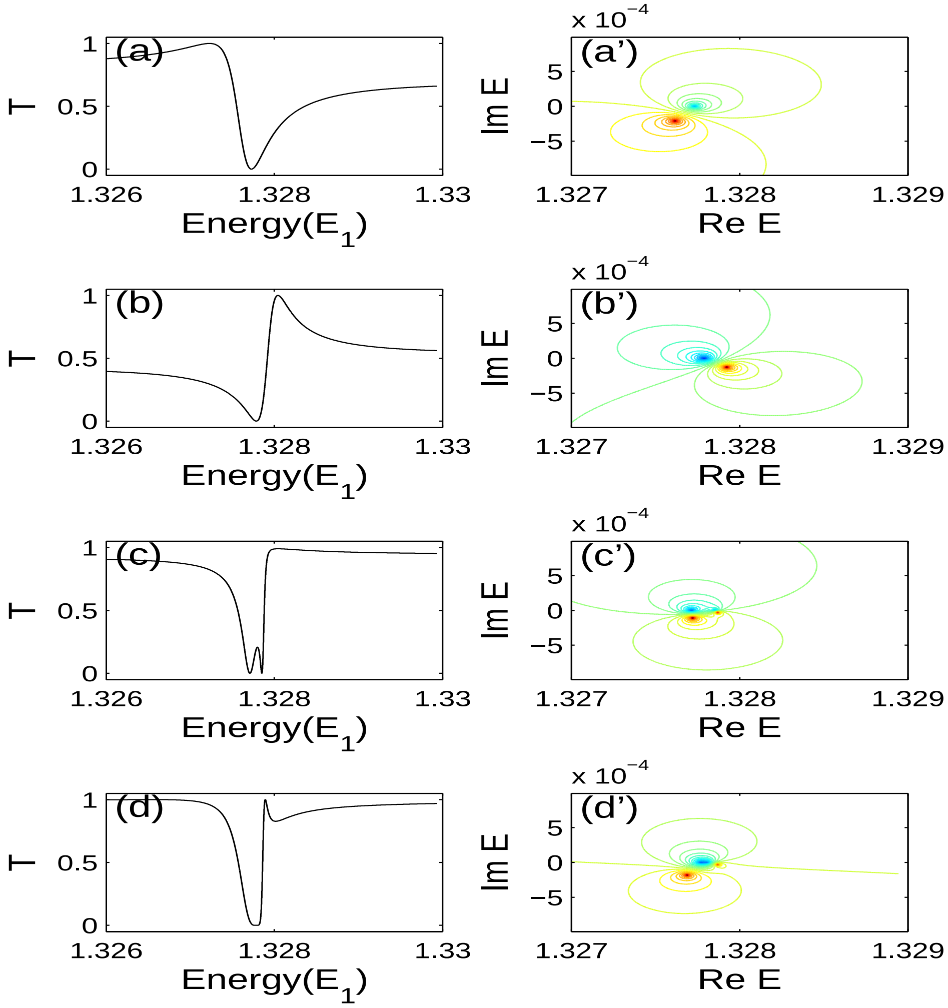

Figure 6.4: (a) and (a') show the electron transmission and contour plot of T in the complex energy plane, respectively when we take into account only ψ_{16} and ψ_{17}. (b) and (b') use only ψ_{18} and ψ_{19} (c) and (c') use ψ_{16}, ψ_{17}, ψ_{18} and ψ_{19}. (d) and (d') use ψ_{15}, ψ_{16}, ψ_{17}, ψ_{18} and ψ_{19}.

transmission zero and two poles (one not clearly visible) which contribute to the resonance. One of the poles is very close to the real axis and the corresponding resonance is very sharp. The other pole is relatively far from the real axis and is easily seen. In Fig. 6.5 (c) we show a magnification of the region near the real axis. This plot clearly shows the pole near the real axis. With this pole structure, an electron can stay in one resonant state for a long time but will escape very fast from the other resonant state.

In order to determine the origin of the two resonance states in Fig. 6.5, in Fig. 6.6 we plot the coefficients γ_j of the scattering wavefunction (see Eq. (6.3)) to determine how each R-matrix basis state contributes to the scattering wavefunction at various incident energies. Fig. 6.6 (a) shows γ_j as a function of j for incident energy $E = 1.583053E_1$, at which perfect transmission ($T = 1$) occurs due to the narrow resonance. It shows that the anti-symmetric 22nd basis state correspond to the narrow resonance. The scattering wavefunction at $E = 1.583053E_1$ is anti-symmetric with respect to the center of the cavity as shown in Fig. 6.6 (c) (the real part is plotted). Fig. 6.6 (d) shows that the real part of the scattering wavefunction at energy $E = 1.583081\,E_1$. It is symmetric with respect to the center of two cavities. Fig. 6.6 (b) shows that the 21st basis state is dominant at $E = 1.583081E_1$, but γ_{23} is not negligible, so that both ψ_{21} and ψ_{23} contribute significantly to the broad resonance state. The difference in the lifetime of the two quasibound states is 100 times greater than for the first resonance structure.

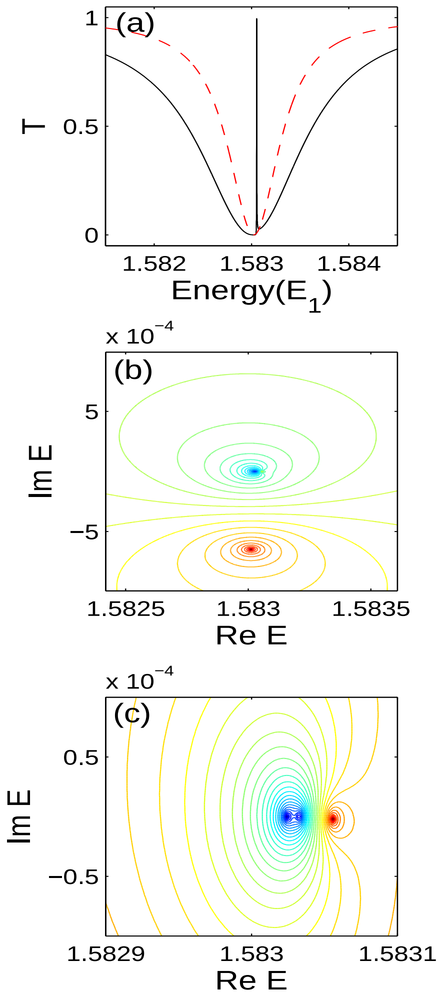

Figure 6.5: (a) Electron transmission at the second resonance energy for the bi-ripple waveguide shows the resonance splitting. The dashed line is the electron transmission for the mono-ripple waveguide. (b) Contour plot of T in a complex energy plane. It shows two poles and a transmission zero. (c) a magnified version of (b) near the transmission zero. It confirms that a pole is located near the real axis.

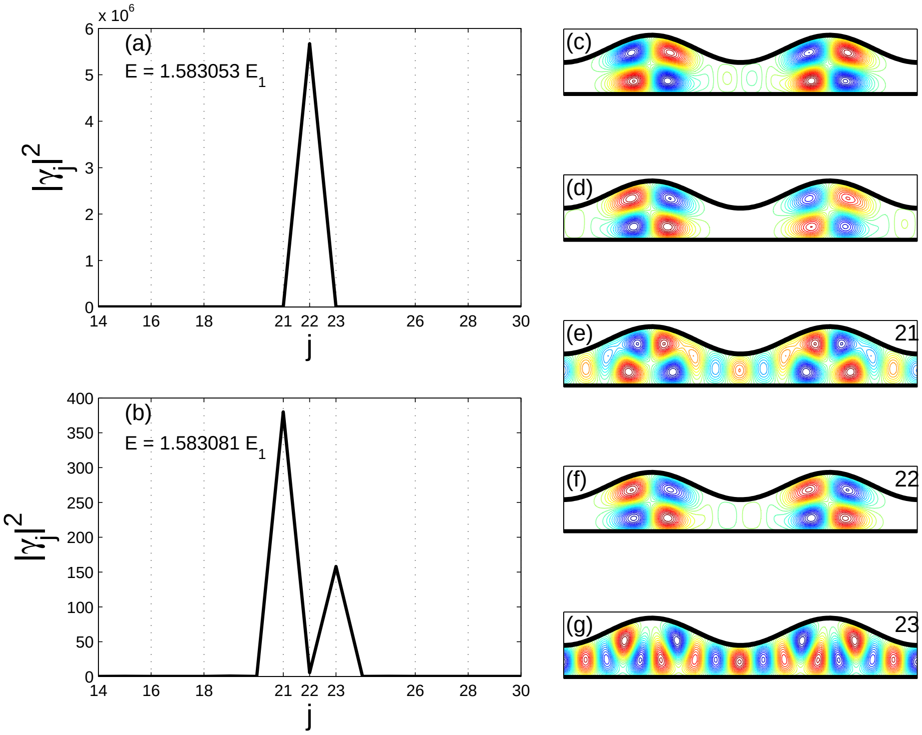

Figure 6.6: (a) and (b) the Coefficient γ_j at the incident energy $E = 1.583053E_1$ which corresponds to the perfect transmission and $E = 1.583053E_1$ which corresponds the transmission zero, respectively. (c) and (d) represent the real part of the scattering wavefunction at $E = 1.583053E_1$ and $E = 1.583053E_1$, respectively. (e) $\sim$ (f) show the R-matrix basis state wavefunction for states ψ_{21}, ψ_{22}, and ψ_{23}.

6.2.3 Other Resonance Structures

Similar clear superpositions of broad and narrow resonances occur at other resonance energies except for the resonance structure at $E = 2.8851E_1$, which is similar to the first resonance structure. We can use the Husimi plots to classify these resonances according to how their probability is distributed in the classical phase space (Fig. 6.1). However, not all resonances can be classified according to their support on classical structures because the energy under consideration here is too low (and wavelengths too long) for some of the scattering states to "see“ the classical structures .

A Husimi plot is a quantum version of a Poincare surface of section. The Husimi function $\tilde{H}(x_0, p_0)$ is defined

$$\tilde{H}(x_0, p_0) \;=\; |\langle S(x)|\, x_0, p_0\rangle|^2, \tag{6.9}$$

where $S(x)$ is the normal derivative of the wavefunction at the bottom wall of the cavity. The state $|\, x_0, p_0\rangle$ is a coherent state which is a minimum uncertainty state and is given by [1, 28]

$$\langle x|\, x_0, p_0\rangle \;=\; \left(\frac{\sigma}{\pi\hbar}\right)^{1/4} exp\left(-\frac{\sigma}{2\hbar}(x-x_0)^2 + i\frac{p_0}{\hbar}(x-x_0)\right), \tag{6.10}$$

where σ is chosen by requiring symmetric coarse graining in phase space [1].

Fig. 6.7 shows some of the resonances in Fig. 6.2 and Husimi Plots for the scattering wavefunction at the corresponding resonance energies. Fig. 6.7 (a) $\sim$ (c) show magnifications of the transmission resonances at energies $E = 2.3779E_1$, $E = 2.8851E_1$, and $E = 2.9235E_1$, respectively. In (a) and (c), we see the resonance broadening and narrowing characteristic of the Dicke effect. However, for the resonance in Fig. 6.7 (b), two transmission zeros collide in a manner similar to the first resonance near $E = 1.327E_1$. Fig. 6.7 (d) $\sim$ (f) show Husimi plots for the scattering eigenstate at the energy corresponding to perfect transmission in Figs. 6.7 (a) $\sim$ (c), respectively. Fig. 6.7 (e) clearly shows that the resonance at $E = 2.8851E_1$ corresponds to a scattering state that sits on the central KAM islands in the corresponding classical phase space of Fig. 6.1 (b). In Fig. 6.7 (f), the Husimi distribution lays on the heteroclinic tangle. Fig. 6.7 (d) appears to be dominated by the island chains surrounding the central KAM islands. Those three resonance families have different widths, which indicates the degree to which the resonant states are connected to the asymptotic region. The resonances associated with the heteroclinic tangle have the broadest width.

6.3 Dicke Effect in a bi-ripple cavity

In 1953, Dicke predicted that spontaneous emission could occur from an excited atom which is in the presence of another atom at a shorter distance than the radiation wavelength. The two atoms indirectly interact through the common photon field. In this interaction regime, the decay channel is split up into fast and slow channels. The fast channel corresponds to a situation in which the excited atom decays and emits radiation through the fast channel but stays a long time in the excited state for the slow channel. The fast (slow) channel radiation is call *superradiance* (*subradiance*). This is the Dicke effect

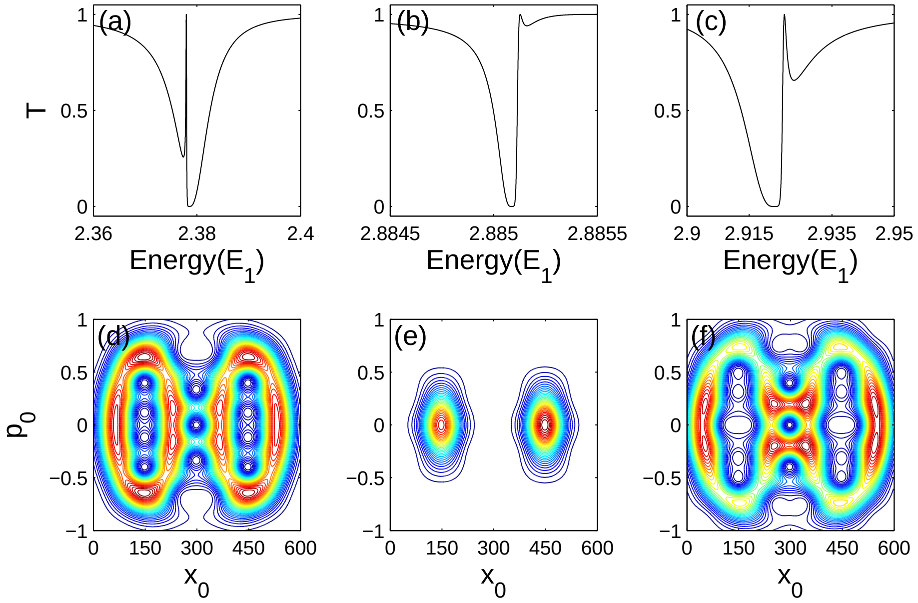

Figure 6.7: The electron transmission in the neighborhood of the energies: (a) $E = 2.3779E_1$, (b) $E = 2.8851E_1$, and (c) $E = 2.9062E_1$. The Husimi plots of scattering eigenstates at the energies (d) $E = 2.3779E_1$, (e) $E = 2.8851E_1$, and (f) $E = 2.9235E_1$.

in quantum optics.

As was mentioned earlier, in mesoscopic systems the Dicke effect was observed by Shahbazyan and Raikh [56] in the form of resonance broadening and narrowing of the electron transmission through two tunneling barriers with two impurities placed between them. The narrow resonance corresponded to the symmetric quasibound state near the two impurities. More recently, the Dicke effect in mesoscopic systems has also been the subject of investigation by a number of authors [60, 61, 57, 62, 63, 64]. In this section, we show that the resonance splittings shown the previous section correspond to the Dicke effect in a multi-ripple waveguide.

In Section 6.2, we saw that the quasibound states of the bi-ripple waveguide have different lifetimes and the scattering states associated with the corresponding resonances form symmetric and anti-symmetric pairs. These quasibound state pairs appear at all resonance positions in Fig. 6.2. The anti-symmetric state is weakly connected to the asymptotic regions (P_ℓ and P_r). This is similar to the situation in which the anti-symmetric state of an electron of two impurities is weakly coupled to electron states in the common leads in Ref. [56].

Broadening and narrowing of resonances and the associated change in the lifetime of the quasibound states, the so called *Dicke Effect*, was described in Ref.[60] in terms of a simple model in which the electron states in two quantum dots are connected directly with each other and indirectly through common leads. In our case, these two effects can be seen explicitly in Eq.(6.7) for the S-matrix. The direct coupling between the two mono-ripples (two "atoms") that comprise the bi-ripple cavity is exactly accounted for because the basis states for the reaction region are exact eigenstates of the Hamiltonian of the bi-ripple cavity. These eigenstates exactly account for the interaction between the mono-ripples. The matrix $\mathbf{w}$ in Eq.(6.7) accounts for the direct coupling between the bi-ripple cavity states and the continuum states in the waveguide leads. However, the fact that the matrix $E\mathbf{1}_{in} - \mathbf{H}_{in} + i\mathbf{w}\cdot\mathbf{w}^T$ is not diagonal means that in some sense there is additional interplay between the various elements of the matrix when we determine solutions to the equation $\mathrm{Det}[E\mathbf{1}_{in} - \mathbf{H}_{in} + i\mathbf{w}\cdot\mathbf{w}^T] = 0$.

We found a weaker Dicke effect in the first and seventh resonances in Fig. 6.2, probably because the direct coupling between the two mono-ripples that comprise the bi-ripple cavity is very weak for these cases. The scattering state at resonance, for these two cases, is composed of two isolated islands of probability that sit on the KAM islands in the mono-ripple cavities. Therefore, there is very weak coupling between the mono-ripples and very weak coupling to the waveguide leads. The other resonance structures appear to be associated with scattering states that sit on the island chain or the tangles in the bi-ripple cavity, thereby having much stronger coupling between the mono-ripples that form the bi-ripple cavity and to the waveguide leads. It is not understood how the weak coupling influences the appearance of the Dicke effect in this calculation. It is an interesting question and needs further study.

It is possible to have the sharp resonance correspond to a symmetric state rather than an anti-symmetric state if the indirect coupling has the opposite sign. This has been observed numerically by Ordonez, Na, and Kim [65].

6.4 Tri- and Quad- Ripple Waveguide

The original Dicke model focused on N coupled atoms in a radiation field and found that the super-radiant state radiates N times faster than the corresponding state in the single atom case [61]. We have found that this same behavior occurs with the quasibound states in multi-ripple waveguides (more than two ripples in a waveguide). The upper wall of tri-ripple and quad-ripple waveguides can be express as $y(x) = d - a\cos(6\pi x/W)$ and $y(x) = d - a\cos(8\pi x/W)$, respectively. We use the same parameters a and d as those of the bi-ripple waveguide while $W = 900\mathring{A}$ and $W = 1200\mathring{A}$ to give the same classical dynamics in the waveguide cavities. Fig. 6.8 (a) shows the electron transmission probability for bi-ripple (solid), tri-ripple (dotted), and quad-ripple (dot-dashed) waveguide at the second resonance structure energy in Fig. 6.2. As each additional mono-ripple is added to the multi-ripple cavity, the electron transmission gains one additional sharp resonance (long lived state) and the resonance corresponding to the Dicke super-radiant state becomes broader. Fig. 6.8 (b) shows the S-matrix poles (the quasibound states) in the complex energy plane for the tri-ripple cavity. Two poles reside near the real axis although they are not clearly shown in this figure, and one pole moves further from the real axis than the corresponding pole for the bi-ripple waveguide. Fig. 6.8 (c) shows the S-matrix poles for the quad-ripple case. Three poles now reside near the real axis and the pole corresponding to the Dicke superradiance state has moved further from the real axis than the corresponding pole for the tri-ripple case.

We plot the imagninary part Γ of the quasibound state pole corresponding the Dicke superradiance state for the second resonance structure as a function of the number of ripples N in Fig. 6.9. We find that Γ increases linearly with the number N of mono-ripples and therefore the lifetime of the superradiant state decreases as $1/N$. This $1/N$ dependence of the lifetime of the superradiant state is the signature of the Dicke effect.

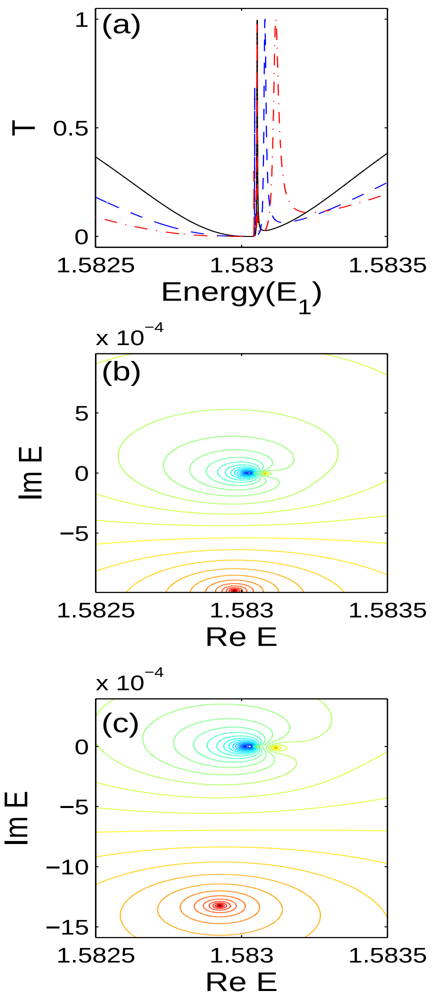

Figure 6.8: (a) The electron transmission in the neighborhood of the 2nd resonance structure for the N-ripple waveguide for N=2 (black solid), N=3(blue dash), and N=4(red dot-dash) (b) S-matrix in a complex energy plane for tri-ripple waveguide. (c) S-matrix in a complex energy plane for quad-ripple waveguide.

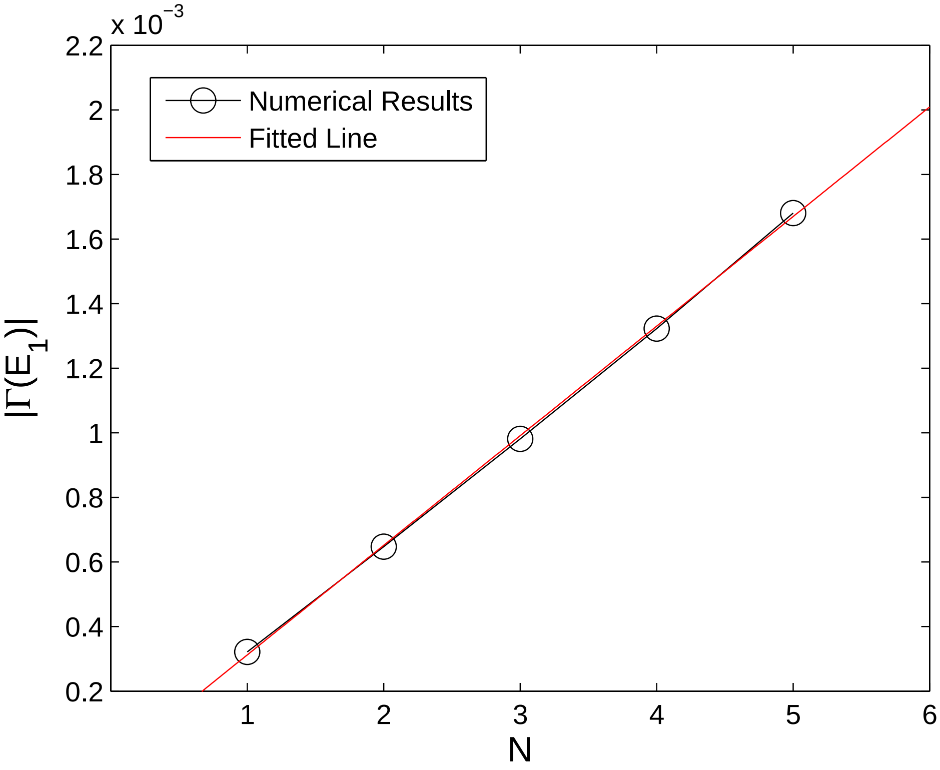

Figure 6.9: The width $|\Gamma|$ of the superradiant quasibound state at the second resonance structure energy for N-ripple waveguide with $N = 1 \sim 5$. Dashed line show the linearly fitted line for help to see the linearity.

Chapter 7

Conclusions

We investigate electron scattering in a waveguide which can be realized in the heterostructure of GaAs/AlGaAs. We study the conductance of a waveguide which contains a single impurity, a ripple waveguide, and a multi-ripple waveguide. Quasi bound state is formed in a waveguide due to the interference of wavefunctions. Thus, conductance fluctuations show the wave-nature of an electron in the waveguide. Conductance is given by Landauer's formula at very low temperature. We numerically compute the transmission probability (S-matrix) through waveguides and a scattering wavefunction by using R-matrix theory. R-matrix is useful and efficient to calculate the conductance in an electron waveguide.

A δ-function potential in two or three space dimensions does not yield convergent expressions for bound state energies in closed systems or scattering properties in open systems. However, we find that a δ-function can be used to model a finite range potential if the number of modes used is truncated in an appropriate manner. We have calculated the conductance for a finite range impurity in a two dimensional waveguide by using the reaction matrix theory. We have shown that the conductance for a δ-function impurity is the same as that of a finite range impurity as long as the mode number N_t is chosen correctly and the Fermi energy is small enough. Boese *et. al* [25], noticed that the number of modes N_t is inversely proportional to the corresponding size of impurity by using the modified δ-function model mentioned in Section 3.1. We have shown here that it is, in fact, determined by the ratio of the impurity range and the size of the confinement region and we have obtained a quantitative expression for the truncation condition.

We have obtained the period of scattering echoes for a quantum waveguide with a ripple cavity via a Fourier transform of the conductance fluctuations and we have shown that this period agrees with the rotation period of trajectories caught in the heteroclinic tangles of the classical system. These results are consistent with the microwave experiment done by Dembowski *et. al.* [37]. We show that the broad resonances in the conductance fluctuations determine the period of the scattering echoes. These resonances are due to states in the chaotic scattering layer which have high probability on heteroclinic tangles. We have observed three distinct families of resonances in the conductance fluctuations. Each family is associated to states lying on different region of the classical Poincare surface of section (the central KAM island, island chain surrounding the central KAM island, and the chaotic scattering layer). We also studied the wavepacket dynamics in the waveguide. The transmission probability for the wavepacket is time-periodic and the period agrees with theoretical predictions obtained from the underlying classical phase space. The exponential decay of the transmission probability shows that the hierarchy states do not play a significant role in the quantum dynamics at the energies considered here.

We have found that resonance splitting in the electron conductance through the bi-ripple waveguide is related to symmetric and anti-symmetric pairs of scattering states. One resonance is broader than the corresponding resonance for the mono-ripple waveguide, while the other is narrower. Using R-matrix scattering theory, we can track the quasibound states that give rise to splitting of resonances by locating the corresponding S-matrix poles in the complex energy plane. For the bi-ripple waveguide, the symmetric resonant scattering states are strongly connected to the continuum, while the anti-symmetric states are isolated. Therefore, an electron in an anti-symmetric state is able to stay in the waveguide cavity for a long time. This is the analog of the Dicke effect in the multi-ripple electron waveguide. It is interesting to note that there is no such resonant splitting for the resonant states which are localized on the central KAM islands because the coupling between mono-ripples, that form the bi-ripple cavity, and coupling to the continuum states in the waveguide leads is very weak.

We have also studied the transmission properties of the N-ripple waveguide (for $N = 3$ and $N = 4$), which is a system similar to the N-atom system in a Dicke model. We find that the lifetime of one of the quasibound states decreases as $1/N$, which is a signature of the Dicke effect. It is useful to note that this effect does not appear to depend strongly on the shape of the waveguide cavities. A similar effect has been seen for two coupled rectangular waveguide cavities [65].

Appendices

Appendix A

Evaluation of a retarded free Green's function in Equation (2.27)

Evaluation of a retarded Green's function in Eq. (2.27) is done by Cauchy integral in a complex energy(wavevector) plane.

$$\begin{aligned}\left\langle x' \left| \frac{1}{E^{(+)} - H_{PP}} \right| x \right\rangle &= \frac{4m}{\hbar^2 \pi} \lim_{\epsilon \to 0} \int_0^\infty \frac{\sin(k'(x'-a))\sin(k'(x-a))}{(k^2 - k'^2) + i\epsilon} dk' \\ &= \frac{4m}{\hbar^2 \pi} \frac{1}{2} \lim_{\epsilon \to 0} \int_{-\infty}^\infty \frac{\sin(k'x_1)\sin(k'x_2)}{(k^2 - k'^2) + i\epsilon} dk' \qquad \text{(A.1)}\end{aligned}$$

where we replace x' (x) by x_1 (x_2) and we use the fact that the integrand is even function for k.

$$\begin{aligned}\lim_{\epsilon \to 0} & \int_{-\infty}^\infty \frac{\sin(k'x_1)\sin(k'x_2)}{(k^2 - k'^2) + i\epsilon} dk' \qquad \text{(A.2)} \\ &= \left(\frac{1}{2i}\right)^2 \Bigg[\underbrace{\lim_{\epsilon \to 0} \int_{-\infty}^\infty \frac{e^{ik'(x_1+x_2)}}{k^2 - k'^2 + i\epsilon} dk'}_{a)} - \underbrace{\lim_{\epsilon \to 0} \int_{-\infty}^\infty \frac{e^{ik'(x_1-x_2)}}{k^2 - k'^2 + i\epsilon} dk'}_{b)} \\ &- \underbrace{\lim_{\epsilon \to 0} \int_{-\infty}^\infty \frac{e^{ik'(x_2-x_1)}}{k^2 - k'^2 + i\epsilon} dk'}_{c)} + \underbrace{\lim_{\epsilon \to 0} \int_{-\infty}^\infty \frac{e^{-ik'(x_1+x_2)}}{k^2 - k'^2 + i\epsilon} dk'}_{d)} \Bigg] \qquad \text{(A.3)}\end{aligned}$$

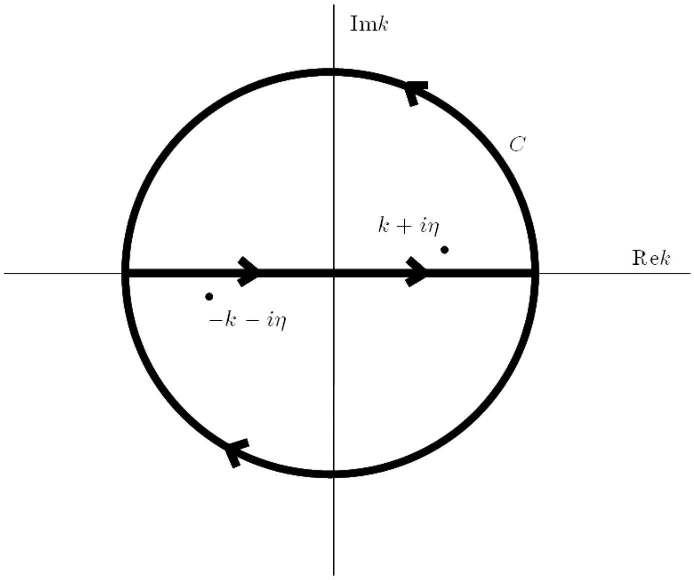

Figure A.1: Path of integral in complex k-plane

We take the limit $x \to \infty$ because we consider the Green's function at the asymptotic region. As a result, x' is larger than x so that x_1 is larger than x_2. The first integral is given by

$$\begin{aligned} a) \quad &= -\lim_{\eta \to 0} \int_{-\infty}^{\infty} \frac{e^{ik'(x_1+x_2)}}{(k'+k+i\eta)(k'-k-i\eta)} dk' \\ &= -(2\pi i) \frac{e^{ik'(x_1+x_2)}}{(k'+k+i\eta)(k'-k-i\eta)} (k'-k-i\eta)\Bigg|_{k'=k+i\eta} \\ &= -\pi i \frac{e^{ik(x_1+x_2)}}{k}. \end{aligned} \tag{A.4}$$

We use the upper half plane because $e^{ik'(x1+x_2)} \to 0$ on the surface of the contour. The second integrals is

$$\begin{aligned} b) &= -\lim_{\eta\to 0}\int_{-\infty}^{\infty}\frac{e^{ik'(x_1-x_2)}}{(k'+k+i\eta)(k'-k-i\eta)}dk' \\ &= -(2\pi i)\frac{e^{ik'(x_1-x_2)}}{(k'+k+i\eta)(k'-k-i\eta)}(k'-k-i\eta)\Big|_{k'=k+i\eta} \\ &= -\pi i\frac{e^{ik(x_1-x_2)}}{k}, \end{aligned} \tag{A.5}$$

where the upper half plane is used because $x_1 > x_2$. The third integral is

$$\begin{aligned} c) &= -\lim_{\eta\to 0}\int_{-\infty}^{\infty}\frac{e^{ik'(x_2-x_1)}}{(k'+k+i\eta)(k'-k-i\eta)}dk' \\ &= -(-2\pi i)\frac{e^{ik'(x_2-x_1)}}{(k'+k+i\eta)(k'-k-i\eta)}(k'+k+i\eta)\Big|_{k'=-k-i\eta} \\ &= -\pi i\frac{e^{-ik(x_2-x_1)}}{k}, \end{aligned} \tag{A.6}$$

where lower half plane is used because $x_1 > x_2$. The last integral in Eq.(A.2) is given by,

$$\begin{aligned} d) &= -\lim_{\eta\to 0}\int_{-\infty}^{\infty}\frac{e^{-ik'(x_1+x_2)}}{(k'+k+i\eta)(k'-k-i\eta)}dk' \\ &= -(-2\pi i)\frac{e^{-ik'(x_1+x_2)}}{(k'+k+i\eta)(k'-k-i\eta)}(k'+k+i\eta)\Big|_{k'=-k-i\eta} \\ &= -\pi i\frac{e^{ik(x_1+x_2)}}{k}, \end{aligned} \tag{A.7}$$

where the lower half plane is used. Consequently, the retarded free Green's function in an asymptotic region ($\hat{P}$) is given by,

$$\begin{aligned}
\left\langle x' \left| \frac{1}{E^{(+)} - H_{PP}} \right| x \right\rangle &= \frac{2m}{\hbar^2 \pi} \left(-\frac{1}{4} \right) \{a) - b) - c) + d)\} \\
&= -\frac{m}{2\hbar^2 \pi} \left(-2e^{ik(x_1 + x)} + 2e^{ik(x_1 - x_2)} \right) \frac{\pi i}{k} \\
&= i \frac{m}{\hbar^2 k} \left(e^{ik(x_1 + x_2)} - e^{ik(x_1 - x_2)} \right) \\
&= i \frac{m}{\hbar^2 k} \left(e^{ik(x' + x)} e^{-2ika} - e^{-ik(x' - x)} \right), \qquad \text{(A.8)}
\end{aligned}$$

where $x_1 (x_2)$ is replaced by $x' - a (x - a)$.

Appendix B

Evaluation of Eq. (2.39)

Equation (2.39) is given,

$$\begin{aligned}\langle x|\hat{P}|\Psi\rangle &= \phi_E(x) + \langle x|G_P^0 T|\phi_0(E)\rangle \qquad (B.1)\\ &= \phi_E(x)\\ &+ \int_a^\infty \int_0^\infty \langle x|G_P^0|x'\rangle\langle x'|\phi_0(E')\rangle\langle\phi_0(E')|T|\phi_0(E)\rangle dE'dx'.\end{aligned}$$

T-matrix, $\langle\phi_0(E')|T|\phi_0(E)\rangle$, can be computed like Eq. (2.36), but the column matrix ω^T is now a function of E' instead of E. We denote it $\omega_{k'}^T$. We then rewrite T-matrix as,

$$\langle\phi_0(E')|T|\phi_0(E)\rangle = \frac{1}{\pi}\omega_{k'}^T \frac{1}{E - H_{in} + i\omega_k\omega_k^T}\omega_k. \qquad (B.2)$$

From Eq. (2.27), a free Green's function is given by,

$$\langle x|G_P^0|x'\rangle = i\frac{m}{\hbar^2 k}\left(e^{ik(x'+x)}e^{-2ika} - e^{ik(x-x')}\right). \qquad (B.3)$$

A plane wave of an energy E' is given by,

$$\begin{aligned}\langle x'|\phi_0(E')\rangle &= A_{k'}\sin\left(k'(x'-a)\right) \qquad (B.4)\\ &= \sqrt{\frac{2m}{\pi\hbar^2 k}}\frac{1}{2i}\left(e^{ik'(x'-a)} - e^{-ik'(x'-a)}\right).\end{aligned}$$

Integration over x' is given by

$$\begin{aligned}\int_a^\infty \langle x|G_P^0|x'\rangle\langle x'|\phi_0(E')\rangle dx' &= i\frac{m}{\hbar^2 k}\sqrt{\frac{2m}{\pi\hbar^2 k}}\frac{1}{2i}e^{ikx} \\ &\quad\times\int_a^\infty \left(e^{ikx'}e^{-2ika} - e^{-ik(x'-a)}\right)\left(e^{ik'(x'-a)} - e^{-ik'(x'-a)}\right)dx' \\ &= i\frac{m}{\hbar^2 k}\sqrt{\frac{2m}{\pi\hbar^2 k}}\frac{1}{2i}e^{ikx}e^{-ika}\int_a^\infty 2i\sin(k(x'-a))2i\sin(k'(x'-a))dx' \\ &= i\frac{m}{\hbar^2 k}\sqrt{\frac{2m}{\pi\hbar^2 k}}\frac{1}{2i}e^{ikx}e^{-ika}(-4)\underbrace{\int_a^\infty \sin(k(x'-a))\sin(k'(x'-a))dx'}_{\frac{1}{A_k^2}\delta(E-E')}.\end{aligned} \tag{B.5}$$

If we plug the above equation into Eq. (B.1), the scattered wave in Eq. (B.1) is given by

$$\sqrt{\frac{m}{2\pi\hbar^2 k}}e^{ika}e^{-2ika}e^{ikx}2\omega_k^T\frac{1}{E-H_{in}+i\omega_k\omega_k^T}\omega_k. \tag{B.6}$$

Therefore, the scattering wavefunction in the asymptotic region is given by

$$\begin{aligned}\langle x|\hat{P}|\Psi\rangle &= i\sqrt{\frac{m}{2\pi\hbar^2 k}}e^{ika}\left(-e^{ikx}e^{-2ika} + e^{-ikx}\right) \\ &+ i\sqrt{\frac{m}{2\pi\hbar^2 k}}e^{ika}e^{-2ika}e^{ikx}2\omega_k^T\frac{1}{E-H_{in}+i\omega_k\omega_k^T}\omega_k \\ &= i\sqrt{\frac{m}{2\pi\hbar^2 k}}e^{ika}\left\{e^{-ikx} - e^{-2ika}\left(1-2i\omega_k^T\frac{1}{E-H_{in}+i\omega_k\omega_k^T}\omega_k\right)e^{ikx}\right\}.\end{aligned} \tag{B.7}$$

Appendix C

Hamiltonian matrix elements of a open ripple cavity (a zero-slope boundary condition for side walls)

We can expand the wavefunction $\psi_j(u,v)$ with a set of basis functions which satisfy boundary condition such as

$$\left.\frac{\partial \psi_j}{\partial u}\right|_{u=0} = \left.\frac{\partial \psi_j}{\partial u}\right|_{u=W} = 0,\ \psi_j(u,0) = \psi_j(u,1) = 0. \tag{C.1}$$

Wavefunction of jth eigen state is written by

$$\psi_j(u,v) \ = \sum_{n,m=1}^{\infty} B^j_{mn}\phi_{mn}(u,v), \tag{C.2}$$

where the basis functions are

$$\phi_{mn}(u,v) \ = \frac{2}{\sqrt{f}} A_m \cos\left(\frac{(m-1)\pi u}{W}\right)\sin(n\pi v), \tag{C.3}$$

where A_m is a normalization constant such as

$$A_m \ = \begin{cases} \sqrt{\frac{1}{W}} & \text{for } \ m=1 \\ \sqrt{\frac{2}{W}} & \text{otherwise} \end{cases}. \tag{C.4}$$

The matrix elements of the Hamiltonian is given by

$$\begin{aligned}\langle\phi_{m'n'}| \quad H \quad |\phi_{mn}\rangle &= H_{m'n'mn} \\ &= 2\int_0^W du\int_0^1 dv\sqrt{f}\sin(n'\pi v)\cos\left(\frac{(m'-1)\pi u}{W}\right)A'_m H \\ &\times \; A_m\frac{1}{\sqrt{f}}\sin(n\pi v)\cos\left(\frac{(m-1)\pi u}{W}\right)J \\ &= H^0_{m'n'mn}+H^1_{m'n'mn}+H^2_{m'n'mn}+H^3_{m'n'mn}, \end{aligned} \tag{C.5}$$

where we require the orthonomality condition,

$$\int\int dudv\phi_{mn}(u,v)\phi_{m'n'}(u,v)J \; = \; \delta_{mm'}\delta_{nn'}, \tag{C.6}$$

where J is a Jacobian of integration for coordinate transformation,

$$J \; = \left|\begin{array}{cc} \frac{\partial x}{\partial u} & \frac{\partial x}{\partial v} \\ & \\ \frac{\partial y}{\partial u} & \frac{\partial y}{\partial v}\end{array}\right| \; = \; f(x). \tag{C.7}$$

In Eq. (C.5), each term is given by

$$\begin{aligned} H^0_{m'n'mn} \;&=\; A_mA'_m\delta_{nn'}\left\{\frac{1}{4}J^5_{mm'} \; - \; \frac{1}{2}\left(\frac{(m'-1)\pi}{2W}\right)J^2_{mm'}\right. \\ &+ \; \left.\frac{1}{2}\left(\frac{(m-1)\pi}{2W}\right)J^2_{m'm}-\frac{W}{2}\left(\frac{(m-1)\pi}{W}\right)^2\delta_{mm'}\right\}, \end{aligned} \tag{C.8}$$

$$H^1_{m'n'mn} \; = \; -A_mA'_m(n'\pi)^2\left\{\delta_{nn'}J^4_{mm'} \; + \; \left(K^2_{m-n'}-K^2_{n+n'}\right)J^5_{mm'}\right\}, \tag{C.9}$$

$$H^2_{m'n'mn} \; = \; A_mA'_m\left(K^1_{n-n'}+K^1_{n+n'}\right)(n'\pi)\left\{J^5_{mm'}-2\left(\frac{(m'-1)\pi}{W}\right)J^2_{mm'}\right\}, \tag{C.10}$$

$$H^3_{m'n'mn} \; = \; A_mA'_m(n'\pi)\left(K^1_{n-n'}+K^1_{n+n'}\right)\left(-J^3_{mm'}+2J^5_{mm'}\right), \tag{C.11}$$

where

$$J^5_{mm'} \equiv \int_0^W du \frac{\cos(\frac{(m-1)\pi u}{W})\cos(\frac{(m'-1)\pi u}{W})}{f^2(u)}(f'(u))^2 \tag{C.12}$$

$$J^4_{mm'} \equiv \int_0^W du \frac{\cos(\frac{(m-1)\pi u}{W})\cos(\frac{(m'-1)\pi u}{W})}{f^2(u)} \tag{C.13}$$

$$J^3_{mm'} \equiv \int_0^W du \frac{\cos(\frac{(m-1)\pi u}{W})\cos(\frac{(m'-1)\pi u}{W})}{f(u)} f''(u) \tag{C.14}$$

$$J^2_{mm'} \equiv \int_0^W du \frac{2\sin(\frac{(m-1)\pi u}{W})\cos(\frac{(m'-1)\pi u}{W})}{f(u)} f'(u) \tag{C.15}$$

$$K^2_n = \int_0^1 d\nu \nu^2 \cos(n\pi\nu) = \begin{cases} \frac{1}{3} & \text{if } n = 0 \\ \frac{2(-1)^n}{n^2\pi^2} & \text{otherwise} \end{cases} \tag{C.16}$$

$$K^1_n = \int_0^1 d\nu \nu \sin(n\pi\nu) = \begin{cases} 0 & \text{if } n = 0 \\ -\frac{(-1)^n}{n\pi} & \text{otherwise} \end{cases} \tag{C.17}$$

Bibliography

[1] L. E. Reichl. *The Transition to Chaos.* Springer-Verlag New York, 2nd edition, 2004.

[2] Katsuhiro Nakamura and Takahisa Harayama. *Quantum Chaos and Quantum Dots.* Oxford University Press, 2004.

[3] Eric J. Heller. Bound-state eigenfunctions of classically chaotic hamiltonian systems: Scars of periodic orbits. *Phys. Rev. Lett.*, 53(16):1515–1518, Oct 1984.

[4] C. M. Marcus, A. J. Rimberg, R. M. Westervelt, P. F. Hopkins, and A. C. Gossard. Conductance fluctuations and chaotic scattering in ballistic microstructures. *Phys. Rev. Lett.*, 69(3):506–509, Jul 1992.

[5] A. Forchel. http://www.ftf.lth.se/coop/qswitch.html.

[6] B. J. van Wees, H. van Houten, C. W. J. Beenakker, J. G. Williamson, L. P. Kouwenhoven, D. van der Marel, and C. T. Foxon. Quantized conductance of point contacts in a two-dimensional electron gas. *Phys. Rev. Lett.*, 60(9):848–850, Feb 1988.

[7] Mark Ya. Azbel'. Quantum particle in a random potential: Implications of an exact solution. *Phys. Rev. Lett.*, 67(13):1787–1790, Sep 1991.

[8] K. Huang. *Int. J. Mod. Phys. A*, 67:1787, 1991.

[9] R. Jackiw. In A. Ali and P. Hoodbhoy, editors, *M. A. B. Beg Memorial Volume*. World Scientific, 1991.

[10] Bodo Huckestein, Roland Ketzmerick, and Caio H. Lewenkopf. Quantum transport through ballistic cavities: Soft vs hard quantum chaos. *Phys. Rev. Lett.*, 84(24):5504–5507, Jun 2000.

[11] E. P. Wigner and L. Eisenbud. Higher angular momenta and long range interaction in resonance reactions. *Phys. Rev.*, 72(1):29–41, Jul 1947.

[12] A. M. Lane and R. G. Thomas. R-matrix theory of nuclear reactions. *Rev. Mod. Phys.*, 30(2):257–353, Apr 1958.

[13] G. Akguc and L. E. Reichl. Effect of evanescent modes and chaos on deterministic scattering in electron waveguides. *Phys. Rev. E*, 64(5):056221, Oct 2001.

[14] G. B. Akguc and L. E. Reichl. Direct scattering processes and signatures of chaos in quantum waveguides. *Phys. Rev. E*, 67(4):046202, Apr 2003.

[15] Hoshik Lee, Han Hsu, and L. E. Reichl. Modeling conduction in electron waveguides with finite-range impurities. *Phys. Rev. B*, 71(4):045307, 2005.

[16] Hoshik Lee, C. Jung, and L. E. Reichl. Scattering echoes in a waveguide with a ripple cavity. *Phys. Rev. B*, 73(19):195315, 2006.

[17] Pier A. Mello and Narendra Kumar. *Quantum Transport in Mesoscopic Systems.* Oxford University Press, 2004.

[18] Charles J. Joachain. *Quantum Collision Theory.* North-Holland, 1987.

[19] Claude Bloch. Une formulation unifiee de la theorie des reactions nucleaires. *Nuclear Physics*, 4:503–528, 1957.

[20] J. Cugnon. Background phase shift in r-matrix theory. *Phys. Rev. C*, 11(2):291–301, Feb 1975.

[21] Dmitry V. Savin, Valentin V. Sokolov, and Hans-Jürgen Sommers. Is the concept of the non-hermitian effective hamiltonian relevant in the case of potential scattering? *Phys. Rev. E*, 67(2):026215, Feb 2003.

[22] R. M. Westervelt S. E. J. Shaw R Fleischmann E. J. Heller K. D. Maranowski A. C. Gossard M. A. Topinka, B. J. LeRoy. *Nature*, 410:183, 201.

[23] Philip F. Bagwell. Evanescent modes and scattering in quasi-one-dimensional wires. *Phys. Rev. B*, 41(15):10354–10371, May 1990.

[24] Daniel Boese, Markus Lischka, and L. E. Reichl. Resonances in a two-dimensional electron waveguide with a single δ-function scatterer. *Phys. Rev. B*, 61(8):5632–5636, Feb 2000.

[25] Daniel Boese, Markus Lischka, and L. E. Reichl. Scaling behavior in a quantum wire with scatterers. *Phys. Rev. B*, 62(24):16933–16938, Dec 2000.

[26] Daniel S. Fisher and Patrick A. Lee. Relation between conductivity and transmission matrix. *Phys. Rev. B*, 23(12):6851–6854, Jun 1981.

[27] Eugen Merzbacher. *Quantum Mechanics.* Wiley, 2nd edition, 1974.

[28] G. A. Luna-Acosta, Kyungsun Na, L. E. Reichl, and A. Krokhin. Band structure and quantum poincaré sections of a classically chaotic quantum rippled channel. *Phys. Rev. E*, 53(4):3271–3283, Apr 1996.

[29] Robert C. Hilborn. *Chaos and Nonlinear Dynamics.* Oxford University Press, 1994.

[30] Paul So. Unstable periodic orbits. *Scholarpedia*, 2:1353, 2007.

[31] Wenjun Li, L. E. Reichl, and Biao Wu. Quantum chaos in a ripple billiard. *Phys. Rev. E*, 65(5):056220, May 2002.

[32] H.-J. Stöckmann and J. Stein. ‘‘quantum’’ chaos in billiards studied by microwave absorption. *Phys. Rev. Lett.*, 64(19):2215–2218, May 1990.

[33] J. Stein and H.-J. Stöckmann. Experimental determination of billiard wave functions. *Phys. Rev. Lett.*, 68(19):2867–2870, May 1992.

[34] H.-D. Gräf, H. L. Harney, H. Lengeler, C. H. Lewenkopf, C. Rangacharyulu, A. Richter, P. Schardt, and H. A. Weidenmüller. Distribution of eigenmodes in a superconducting stadium billiard with chaotic dynamics. *Phys. Rev. Lett.*, 69(9):1296–1299, Aug 1992.

[35] Y.-H. Kim, M. Barth, H.-J. Stöckmann, and J. P. Bird. Wave function scarring in open quantum dots: a microwave-billiard analog study. *Phys. Rev. B*, 65(16):165317, Apr 2002.

[36] C. Dembowski, B. Dietz, H.-D. Gräf, A. Heine, T. Papenbrock, A. Richter, and C. Richter. Experimental test of a trace formula for a chaotic three-dimensional microwave cavity. *Phys. Rev. Lett.*, 89(6):064101, Jul 2002.

[37] C. Dembowski, B. Dietz, T. Friedrich, H.-D. Gräf, A. Heine, C. Mejía-Monasterio, M. Miski-Oglu, A. Richter, and T. H. Seligman. First experimental evidence for quantum echoes in scattering systems. *Phys. Rev. Lett.*, 93(13):134102, Sep 2004.

[38] R. Hofferbert, H. Alt, C. Dembowski, H.-D. Gräf, H. L. Harney, A. Heine, H. Rehfeld, and A. Richter. Experimental investigations of chaos-assisted tunneling in a microwave annular billiard. *Physical Review E (Statistical, Nonlinear, and Soft Matter Physics)*, 71(4):046201, 2005.

[39] A. Mittal D. E. Prober M. W. Keller, O. Millo and R. N. Sacks. Magnetotransport in a chaotic scattering cavity with tunable electron density. *Surface Science*, 305:501–506, March 1994.

[40] Mark W. Keller, A. Mittal, J. W. Sleight, R. G. Wheeler, D. E. Prober, R. N. Sacks, and H. Shtrikmann. Energy-averaged weak localization in chaotic microcavities. *Phys. Rev. B*, 53(4):R1693–R1696, Jan 1996.

[41] B. V. Chirikov and D. L. Shepelyansky. Asymptotic statistics of poincaré recurrences in hamiltonian systems with divided phase space. *Phys. Rev. Lett.*, 82(3):528–531, Jan 1999.

[42] J. P. Bird, R. Akis, D. K. Ferry, D. Vasileska, J. Cooper, Y. Aoyagi, and T. Sugano. Lead-orientation-dependent wave function scarring in open quantum dots. *Phys. Rev. Lett.*, 82(23):4691–4694, Jun 1999.

[43] Arnd Bäcker, Achim Manze, Bodo Huckestein, and Roland Ketzmerick. Isolated resonances in conductance fluctuations and hierarchical states. *Phys. Rev. E*, 66(1):016211, Jul 2002.

[44] R. Ketzmerick, L. Hufnagel, F. Steinbach, and M. Weiss. New class of eigenstates in generic hamiltonian systems. *Phys. Rev. Lett.*, 85(6):1214–1217, Aug 2000.

[45] R. Akis, J. P. Bird, and D. K. Ferry. The persistence of eigenstates in open quantum dots. *Applied Physics Letters*, 81(1):129–131, 2002.

[46] Bernhard Weingartner, Stefan Rotter, and Joachim Burgdörfer. Simulation of electron transport through a quantum dot with soft walls. *Physical Review B (Condensed Matter and Materials Physics)*, 72(11):115342, 2005.

[47] O Merlo C Jung, C Mejía-Monasterio and T H Seligman. Self-pulsing effect in chaotic scattering. *New Journal of Physics*, 6:48, 2004.

[48] C. Lipp C. Jung and T. H. Seligman. The inverse scattering problem for chaotic hamiltonian systems. *Annals of Physics*, 275:151, August 1999.

[49] Bruno Crespi, Gabriel Perez, and Shau-Jin Chang. Quantum poincaré sections for two-dimensional billiards. *Phys. Rev. E*, 47(2):986–991, Feb 1993.

[50] U. Fano. Effects of configuration interaction on intensities and phase shifts. *Phys. Rev.*, 124(6):1866–1878, Dec 1961.

[51] Cristopher C. Eugster and Jesús A. del Alamo. Tunneling spectroscopy of an electron waveguide. *Phys. Rev. Lett.*, 67(25):3586–3589, Dec 1991.

[52] Fernando Sols, M. Macucci, U. Ravaioli, and Karl Hess. Theory for a quantum modulated transistor. *J. Appl. Phys.*, 66(8):3892–3906, 1989.

[53] K. Na and L. E. Reichl. Electron conductance and lifetimes in a ballistic electron waveguide. *J. Stat. Phys*, 92(3/4):519, 1998.

[54] Roland Ketzmerick. Fractal conductance fluctuations in generic chaotic cavities. *Phys. Rev. B*, 54(15):10841–10844, Oct 1996.

[55] R. H. Dicke. The effect of collisions upon the doppler width of spectral lines. *Phys. Rev.*, 89(2):472–473, Jan 1953.

[56] T. V. Shahbazyan and M. E. Raikh. Two-channel resonant tunnleing. *Phys. Rev. B*, 9(24):17123, February 1994.

[57] T. Vorrath and T. Brandes. Dicke effect in the tunnel current through two double quantum dots. *Phys. Rev. B*, 68(3):035309, Jul 2003.

[58] F. Dominguez-Adame P.A. Orellana and E. Diez. Dicke effect in a quantum wire with side-coupled quantum dots. *Physica E*, 35(1):126, Oct 2006.

[59] G. V. Mil'nikov and H. Nakamura. Regularizaiton of scattering calculations at r-matrix poles. *J. Phys. B*, 34:L791, 2001.

[60] T. V. Shahbazyan and S. E. Ulloa. Localized states in a strong magnetic field: Resonant scattering and the dicke effect. *Phys. Rev. B*, 57(11):6642–6653, Mar 1998.

[61] Tobias Brandes. Coherent and collective quantum optical effects in mesoscopic systems. *Physics Reports*, 408:315, February 2005.

[62] Bernhard Wunsch and Alexander Chudnovskiy. Quasistates and their relation to the dicke effect in a mesoscopic ring coupled to a reservoir. *Phys. Rev. B*, 68(24):245317, Dec 2003.

[63] T. Brandes and B. Kramer. Spontaneous emission of phonons by coupled quantum dots. *Phys. Rev. Lett.*, 83(15):3021–3024, Oct 1999.

[64] P. A. Orellana, M. L. Ladrón de Guevara, and F. Claro. Controlling fano and dicke effects via a magnetic flux in a two-site anderson model. *Phys. Rev. B*, 70(23):233315, 2004.

[65] Gonzalo Ordonez, Kyungsun Na, and Sungyun Kim. Bound states in the continuum in quantum-dot pairs. *Physical Review A (Atomic, Molecular, and Optical Physics)*, 73(2):022113, 2006.

Vita

Hoshik Lee was born in Paju City, South Korea on 27 Jan 1975, the son of Ha Yong Lee and Yong He Lee. He entered Sungkyunkwan University and received the degree of Bachelor of Science in Physics in February 1997. He studied theoretical nuclear physics and received his Master's degree in Physics in February 1999. After two years of military service in South Korea, he entered the University of Texas at Austin in August 2002. He joined the Center for Complex Quantum Systems in January 2003 and started his research on quantum chaos under Dr. Linda E. Reichl.

Permanent address: 432 Paju 3 Ri Paju-Eup Paju City, Kyunggi-Do
South Korea

This dissertation was typeset with LaTeX[†] by the author.

[†] LaTeX is a document preparation system developed by Leslie Lamport as a special version of Donald Knuth's TeX Program.